University of Texas at Arlington
MavMatrix

Physics Dissertations	Department of Physics

2023

Self-Consistent Effects of the Recirculating Plasmapshere on the Development of Storm Time Dynamics in the Inner Magnetosphere.

Christian-Andrew Bagby-wright

Follow this and additional works at: https://mavmatrix.uta.edu/physics_dissertations

Part of the Physics Commons

Recommended Citation

Bagby-wright, Christian-Andrew, "Self-Consistent Effects of the Recirculating Plasmapshere on the Development of Storm Time Dynamics in the Inner Magnetosphere." (2023). *Physics Dissertations*. 116.
https://mavmatrix.uta.edu/physics_dissertations/116

This Dissertation is brought to you for free and open access by the Department of Physics at MavMatrix. It has been accepted for inclusion in Physics Dissertations by an authorized administrator of MavMatrix. For more information, please contact leah.mccurdy@uta.edu, erica.rousseau@uta.edu, vanessa.garrett@uta.edu.

Self-Consistent Effects of the Recirculating Plasmapshere on the Development of Storm Time Dynamics in the Inner Magnetosphere.

Christian-Andrew Todd Bagby-Wright

This thesis is submitted to the Faculty of the Department of Physics in partial fulfillment of the requirements of the Degree of

Doctorate of Philosophy in Physics

at the

University of Texas at Arlington

May, 2023

Copyright 2023 – All rights are reserved and held by,

Christian-Andrew Todd Bagby-Wright

Declaration of Authorship

I, **Christian-Andrew Bagby-Wright**, declare that this thesis titled, "Self-Consistent Effects of the Recirculating Plasmapshere on the Development of Storm Time Dynamics in the Inner Magnetosphere." and the work presented in it are my own. I confirm that:

- This work was done wholly or mainly while in candidature for a research degree at the University of Texas at Arlington
- Where any part of this thesis has previously been submitted for a degree or any other qualification at this University or any other institution, this has been clearly stated.
- Where I have consulted the published work of others, this is always clearly attributed.
- Where I have quoted from the work of others, the source is always given. With the expectation of such quotations, this thesis is entirely y own work.
- I have acknowledged all main sources of help.
- Where the thesis is based on work done by myself jointly with others, I have made clear exactly what was done by others and what I have contributed myself.

Signed: Christian-Andrew Bagby-Wright

Date: 4/19/2023

0.1 Special Thanks

I would first like to thank my advisor, Dr. Daniel T. Welling, for taking on a young and inexperienced graduate student. Your patient yet firm guidance was the exact combination I needed to flourish.

I thank Dr. Ramon E. Lopez for his guidance, many good stories, and providing a place for me to land when Dr. Welling changed institutions.

I would like to thank my parents, Raymond T. Wright and Lisa E. Bagby. Your support was the rock upon which this work is built. I never needed to worry about housing, food, or any basic need, knowing that, if I feel short, it wouldn't be a long fall.

I thank my sister, Genna-Rebecca E. Bagby-Wright, the only other person in the world who understands how long our names are. I'm so proud of you having done your own graduate degree. You know the difficultly of walking this path, and you did it with a full time job! The support and understanding you have shown me is treasured.

I would like to thank my friends, Sion Alfred, Jon Franklin, and Adam Lishman. The friendship and brotherhood each of you have shown me has been invaluable. You each provided an empathetic ear and wise counsel many times over the years. More importantly you reminded, and helped me to, enjoy the journey. Long Live the Republic!

0.2 Abstract

The near Earth space environment is a highly coupled system. The Interplanetary Magnetic Field (IMF) interacts with the magnetosphere in myriad ways depend on the orientation of the IMF to the magnetosphere. The magnetic fields of the magnetosphere and the IMF trap plasma and carry the plasma with it as both magnetic fields evolve over time. This plasma can in turn interact with other plasmas, carried by other field lines, affecting the dynamics of the other population and the magnetic field lines of both populations. The nature, frequency, and importance of interactions between different plasma, or magnetic fields, varies greatly depending on things such as the density of the plasma, strength of the magnetic field, or relative energies of the plasmas. The study of these many varied and recursive relationships is called magnetohydrodynamics (MHD). The plasmasphere is a population of cold and dense plasma near Earth, which often goes understudied due to its typically sedentary nature.

The fate of plasmasphere material once it is drained out of the plasmasphere through a plume and into the solar wind or plasma mantle is unknown. One of two things may happen to the eroded plasmasphere material. It can be swept away with the solar wind, lost to the Earth system, or it may be recaptured by reconnection on the night side of the planet, and transported through the plasma sheet into the inner magnetosphere. Recirculating plasmasphere material which

has been recaptured could plausible contribute to the ring current.

Using observations to study the fate of the plasmasphere is difficult, as space plasma is mostly hydrogen. The homogeneity of the plasma species complicates identifying source populations of a plasma with in situ observations. Numerical models however, can keep the material distinct, opening the possibility of resolving the question using simulations.

This work was completed in two major parts. The first part uses numerical models to answer two questions: First, does any plasmasphere material recirculate back into the magnetosphere? Second, what signature can we look for in real world data to distinguish if this is a physical or model effect? This is done by studying simulations produced by the Space Weather Modeling Framework (SWMF) configured to couple three models: the Block Adaptive Tree Solar Roe Up Wind Scheme (BATS-R-US) model, the Dynamic Global Core Plasma Model (DGCPM) plasmasphere model, and the Ridley Ionosphere Model (RIM). For these simulations BATS-R-US is configured to use two fluids. The first fluid represents currently accepted sources of ring current material, namely the solar wind and high latitude ionospheric outflow (polar wind). The second fluid represents the plasmasphere. Within 10 Earth Radii (R_E) the dynamics of the second BATS-R-US fluid on closed field lines is dictated by coupling with the DGCPM. DGCPM passes the density of material in the plasmasphere to BATS-R-US. In addition to

this coupling, RIM passes electric field information to both BATS-R-US and DG-PCM while receiving current density form BATS-R-US. This configuration of the SWMF represents a novel advancement in simulations of the plasmasphere, more self-consistent then previous studies. To study how plasmasphere material recirculates and how it might affect the ring current two simulations are run: including an Idealized Square Wave Event and an Idealized Corotating Interaction Region Event.

The second part consists of altering the configuration of the SWMF and integrated models to enhance our ability to explore plasmasphere recirculation. I place a particular emphasis on integrating a ring current model. The integration of a ring current model would allow use to self-consistently study the effects of the recirculating plasmasphere on key metrics of storm strength such as D_{st}. This is done by studying simulations produced by the SWMF configured to couple three models: BATS-R-US, the Comprehensive Inner Magnetosphere-Ionosphere (CIMI) model, and RIM. BATS-R-US is again configured to use two fluids. The first fluid represents currently accepted sources of ring current material, namely the solar wind and polar wind. The second fluid represents the plasmasphere. Within 10 R_E the dynamics of the plasmasphere fluid in BATS-R-US on closed field lines are dictated by coupling with CIMI. In a new capability added to CIMI for this study, BATS-R-US passes density and pressure information to two populations in

CIMI. Previously CIMI had only one population to represent plasma at its outer boundary. We have added a second population representing the portion of the plasmasphere which has recirculated which contributes directly to ring current material. With this new capability, we can see exactly what portion of observables such as density, momentum, and pressure or D_{st} comes from the recirculating plasmasphere material. CIMI then couples back to BATS-R-US by passing the total density of material in the plasmasphere to the MHD plasmasphere fluid, as well as the pressure of the ring current and radiation belt. In addition to this coupling, RIM passes electric field information to both BATS-R-US and CIMI while receiving current density from BATS-R-US. This configuration has the advantage of an integrated ring current model over the above configuration of the SWMF. This allows us to self-consistently model the ring current while maintaining the advantage of being able to distinguish how much each population contributes to the total ring current. While I do not presented conclusive results of simulations conducted with such a configuration, I will discuss model development, verification, and the current state of the effort.

Contents

List of Figures

Chapter 1

Introduction

Space physics is the area of physics primarily concerned with the recursive relationship between plasma, abundant in space, and the electric and magnetic fields found in the interplanetary and interstellar mediums, as well as near stars and planetary bodies. In its earliest forms, space physics was studied through observations of the aurora, Earth's magnetic field through the use of a compass, and after the invention of the telescope, observations of sunspots.

Space physics is a strongly interconnected field of study with many recursive relationships between the different populations of plasma and fundamental driving physics. There are many approaches for unraveling the interconnected near-Earth space environment. For the purposes of this brief primer on the subject we shall follow the energy of the system, starting at the sun.

1.1 Solar Wind

The magnetic fields at the surface of the sun are complicated. As various magnetic systems interact plasma can be ejected from the sun through funnels, coronal holes, coronal mass ejections and other mechanisms. Once ejected from the sun the plasma will begin to move towards Earth as part of the solar wind, governed by the magnetohydrodynamic (MHD) equations. The MHD equations contain information of the bulk flow velocity, collisions transfers, and sources and sinks of plasma moments. Specific recurring systems are created by the interactions of various flows of plasma as they balance pressure, momentum, and the configuration of their magnetic fields. Such configurations of the solar magnetic field include the heliospheric current sheet, coronal mass ejections, and Corotating Interaction Regions. The variable nature of the solar wind causes asymmetries in the flow of plasma in the interplanetary magnetic field. Factors such as the corotation of the sun's magnetic field, sunspots, and others contribute to the irregular flow of the solar wind. The solar wind is comprised primarily of protons, electrons, 4% alpha particles, and minor amounts of heavier ions. Due to the low density and high temperature of the solar wind kinetic effects are more important in the solar wind then in other plasma populations. Kinetic effects include things like Coulomb collisions and wave particle interactions.

The ideal Ohm's law holds for the solar wind. As a consequence the frozen-in flux theorem is true for the plasma in the solar wind. The frozen-in flux theorem has two halves; firstly, the magnetic flux through any enclosed area remains constant as the area is transported with the fluid , secondly, any magnetic field line that connects two fluid elements remains connected with the fluid elements [1]. Due to the frozen-in flux theorem the plasma of the solar wind carries the magnetic field embedded within it through space. This magnetic field constitutes the interplanetary magnetic field (IMF). For the research presented herein the B_Z component of the IMF is important as the physical processes we are interested in occur when it is negative (interchangeably referred to as southward).

A common coordinate system which is used within space physics is the geocentric solar ecliptic (GSE) system. In this system the positive X-axis points from the center of Earth to the center of the Sun, while the positive Z-axis is normal to the plane of the ecliptic pointing northward, while the positive Y-axis completes the right-handed coordinate system. This is the system we will default to throughout most of this paper, explicitly stating when we diverge from it.

There are several features of the solar wind that are important my research. When these features reach Earth, they interact with Earth's magnetic fields in different ways, affecting the local flow of plasma. The first of these features is a Corotating Interaction Region (CIR) event, in which fast streams of the solar wind catch up to slow streams in the rotating field creating a CIR. CIRs themselves are not storms, though they may cause them. CIRs feature an oscillating B_z with a long recovery phase, this can cause a weak magnetic storm. Coronal mass ejection events have two sub categories, magnetic clouds, and sheath driven. The magnetic geometry of sheath driven CME events is similar to that of CIR storms, however the two classes of storm vary in average storm length, recovery, and intensity. Magnetic Cloud type CMEs have a strong magnetic field rotated through a large angle[2].

1.2 Magnetic Storms and Reconnection

The magnetosphere is defined as the region of space dominated by Earth's magnetic field. As magnetic field lines cannot cross, the terrestrial magnetic field carves a cavity in space where the IMF can not penetrate. The magnetosphere is separated from the solar wind by the magnetopause. The solar wind is separated from the magnetosphere by the magnetopause current on the dayside and the tail current on the night side. Figures 1.1 and 1.2 show a summary of the major current systems and plasma populations found in the inner magnetosphere respectively.

Magnetic storms are characterized by extended southward IMF passing Earth, associated with a strong dawn-to-dusk electric field. This dawn-to-dusk electric field increases convection within the magnetosphere which causes many phenomena including the formation of a ring current. The ring current alters the magnetic field on Earth's surface, by reducing the horizontal component, which can be measured. Storms are often quantified by the disturbance storm time index ($\mathrm{D_{st}}$) which represents the deflection of the horizontal magnetic field as seen on the surface of Earth [3].

Magnetic reconnection between the interplanetary magnetic field (IMF) and the magnetosphere is the primary way in which energy is transferred from the solar wind to Earth's magnetosphere. Reconnection can happen regardless of the IMF orientation, but is most effective at transferring energy from the solar wind to the magnetosphere when the IMF is southward. It is the dynamics which occur during the southward configuration which are important for my research. As such I will neglect the northward case and focus on the dynamics of the magnetosphere during southward IMF conditions.

When the IMF is southward, dayside magnetic reconnection becomes possible. In this configuration the topology of the magnetic field changes, and ideal MHD is no longer valid. Because ideal MHD is no longer valid we can no longer relay on the ideal Ohm's law:

$$\mathbf{E} + \mathbf{u} \times \mathbf{B} = 0 \tag{1.1}$$

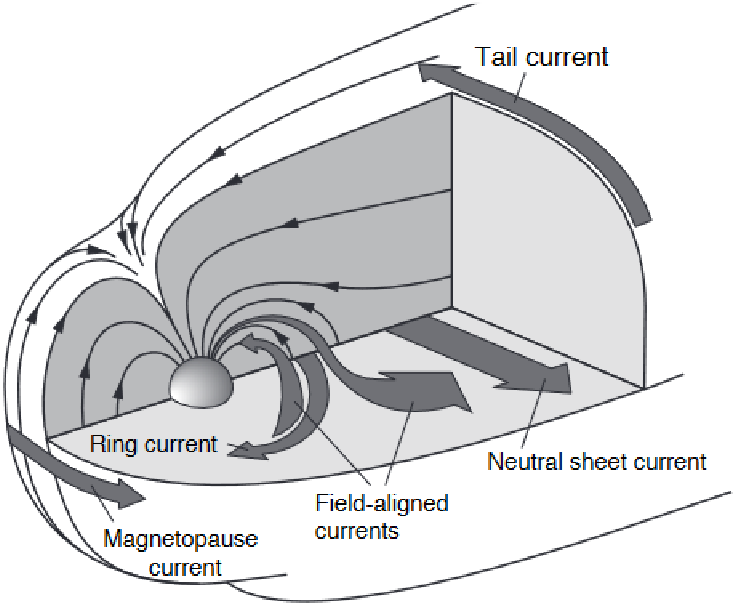

FIGURE 1.1: Major current systems the magnetosphere. Taken from Fig 1.6 in [4].

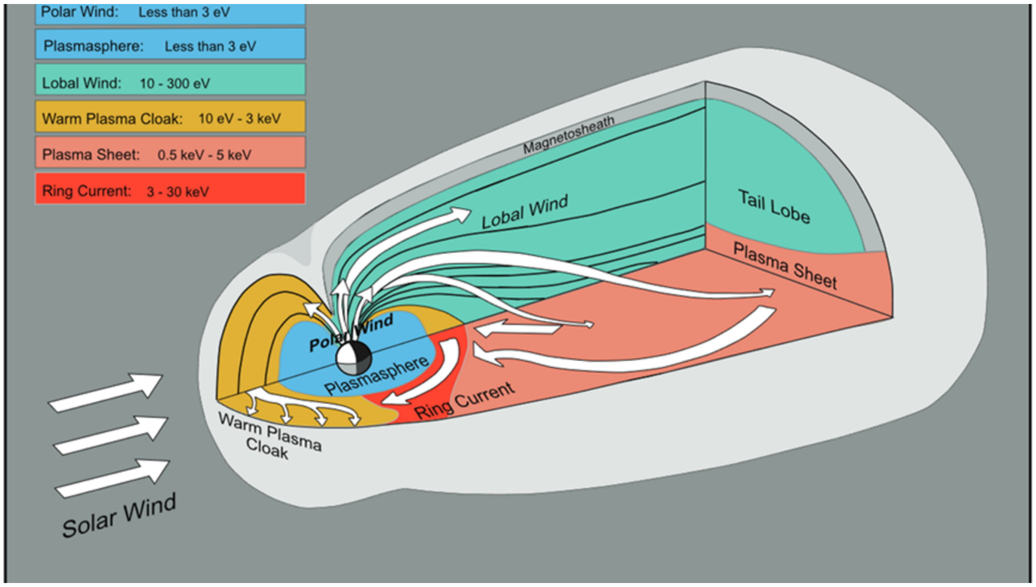

FIGURE 1.2: Major plasma populations of the inner magnetosphere and typical energies for the same. White arrows depict path of plasma from the ionosphere as it circulates within the magnetosphere. Reproduced from Figure 16 [5].

This additionally means that the frozen-in flux theorem is broken for the solar wind. Once we leave the domain of the frozen in flux theorem and ideal Ohm's law we must relay on the generalized Ohm's law:

$$\frac{\partial}{\partial t}\mathbf{j}+\nabla\cdot\left(\sum_{s}\frac{q_s\mathbf{P}_s}{m_s}+\mathbf{ju}+\mathbf{uj}-\rho_q\mathbf{uu}\right)-\sum_{s}\frac{q_s^2 n_s}{m_s}(\mathbf{E}+\mathbf{u}\times\mathbf{B})-\rho_q\mathbf{g}=\sum_{s,k}n_s q_s v_{s,k}(\mathbf{u}_s-\mathbf{u}_k). \tag{1.2}$$

where s refers to the species, **j** is the current, q is the charge, **P** is the pressure, m is the mass, **u** is the bulk flow velocity, ρ_q is the charge density, n is the number density, **g** acceleration due to gravity, $v_{s,k}$ is the collision frequency between the species s and k, the summations occur over species s and k, and other symbols have there expected meanings. In this regime reconnection becomes possible.

While reconnection is a broad, deep, active, and an important field of study it is not completely understood and its mechanics are outside the scope of this work. For an example of the work being done with reconnection see [6]. When plasma both in the solar wind and Earth's magnetosphere moves towards the magnetopause ideal MHD breaks down and we shift to the regime of the generalized Ohm's law (Figure 1.3 at t<0). However, keep in mind that reconnection only occurs on a small scale. Therefore, the frozen in flux theorem is true thought out most of the plasma even during reconnection.

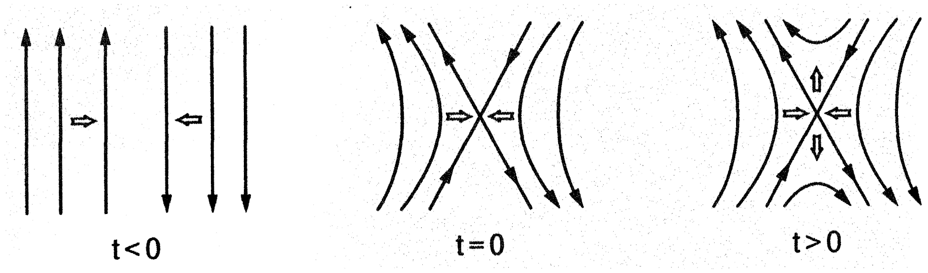

FIGURE 1.3: Major current systems the magnetosphere. Reproduced from Figure 5.3 [4].

During the process of reconnection the magnetic field vanishes at a particular point (Figure 1.3 t = 0). This results in the X-type configuration seen in Figure 1.3 at t=0. The center of the X-shape is called the neutral point. As the fields lines reconnect the tension in the magnetic field lines causes them to relax leaving the reconnection region both above and below the reconnection point, while the pressure of the solar wind and magnetosphere push new field lines in; giving us the configuration seen in Figure 1.3 at t>0. This X-shaped configuration stretches along the dayside magnetopause and forms the separatrix. As the anti-parallel field lines of the solar wind and magnetosphere reconnect the plasma that was trapped on those field lines mixes and homogenizes as the field lines move tail ward.

During southward IMF the magnetosphere will undergo the Dungey cycle. Figure 1.4 shows a diagram of the entire Dungey cycle. The dark arrows outside the magnetosphere (the shaded region) represent the flow of the solar wind plasma while the white arrows within the magnetosphere show the flow of magnetospheric plasma. The magnetic field lines labeled 1 and 2 in Figure 1.4 correspond to t<0, and t>0 in Figure 1.3 respectively. Note that the reconnected field line has foot points on both Earth and in the solar wind. The solar wind will transport this field line down-tail dragging the foot point connected to Earth across the polar cap (this process is represented by field lines 3-6). This allows magnetospheric plasma to be transported by the movement of the magnetic fields. This movement of magnetospheric plasma over the poles is a key part of my research and something which we will discuss in more detail latter. Down tail the northern and southern open field lines will meet again as they become stretched around the magnetosphere and night side reconnection will occur (line 7 in Figure 1.4). After night side reconnection both the field lines closed to Earth and to the solar wind will relax. It is this relaxing of the field lines which leads to the flow of plasma from the deep tail Earthward, shown by the white arrows in the tail of Figure 1.4 and also shown in Figure 1.2. The relaxed solar wind line is represented by line 8 in Figure 1.4.This work focus on the behavior and fate of plasmasphere material during magnetic storms. Now that we have established a baseline knowledge of how storms in space work, we can move on to exploring the plasmasphere.

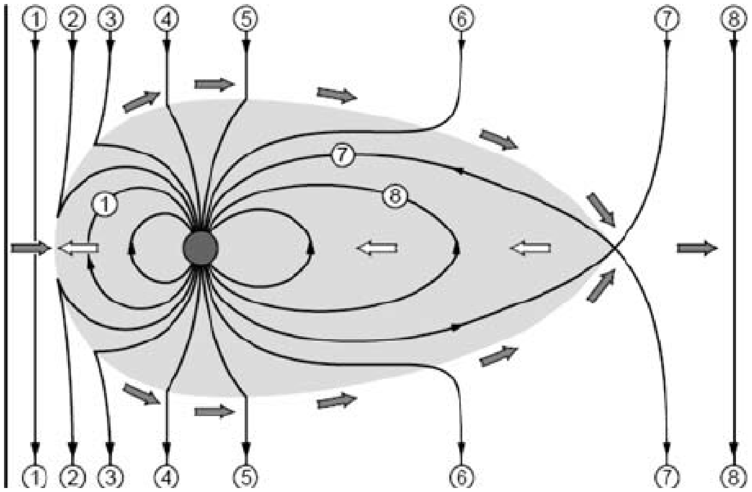

FIGURE 1.4: Magnetic reconnection and merging in at both on both the day and night side. Reproduced from Fig 5.4 [4].

1.3 Plasmasphere

The magnetopause current is connected to a potential difference across the magnetosphere. This potential difference creates a dawn-dusk electric field within the magnetosphere. The constant rotation of Earth and the embedded dipole gives rise to another electric field pointed radially inwards towards Earth. The balance of these two fields gives rise to lines of electric equipotentials. Low energy particles within the magnetosphere will drift along these equipotential lines conserving total electromagnetic energy. Depending on the path these particles can reach the magnetopause and find itself on a field line that is merged with the IMF. This is called an open drift path. Within the line of zero potential the drift paths of plasma

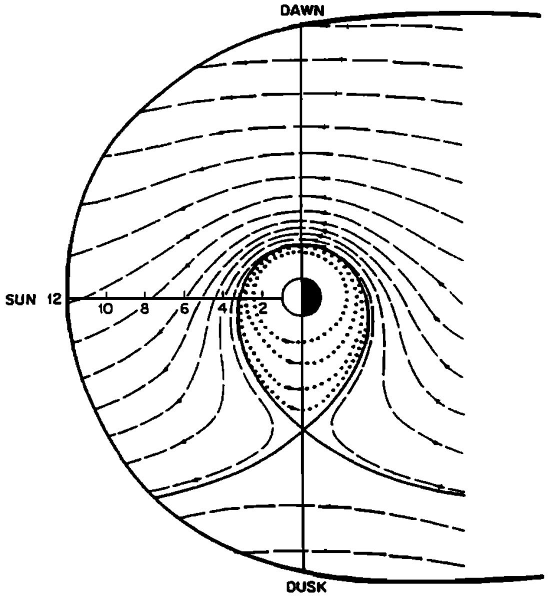

FIGURE 1.5: Lines of Electric Equipotential in the innermagnetosphere giving rise to the tear drop model of the plasmasphere. Reproduced from [7], Figure 1.

are closed. This region is defined to be the plasmasphere. This gives rise to the tear drop model of the plasmasphere shown in Figure 1.5. The teardrop model is a fundamentally simplistic view of the plasmasphere, hence why the true teardrop shape is not seen in observation, but it does highlight some of the fundamental physics at play in the plasmasphere which is important to this work.

Russell and Strangeway [1] states that a particle's drift velocity can be generalized to any velocity-independent force **F**:

$$\mathbf{v}_d = \frac{\mathbf{F} \times \mathbf{B}}{qB^2} \tag{1.3}$$

where q is the particle charge, **F** is the velocity-independent force, and **B** is the magnetic field. If the force can be expressed in terms of a potential, such as the electric potential for a static electric field $\mathbf{F} = -q\nabla\tilde{\phi}$, then we can rewrite the drift velocity as:

$$\mathbf{v}_d = \frac{\mathbf{B} \times \nabla\tilde{\phi}}{B^2} \tag{1.4}$$

As a consequence, drift paths follow equipotential contours for this generalized potential.

To explore this in more detail, with out unnecessary complexity, we will make a few simplifying assumptions. First, that Earth's magnetic field can be well represented as a magnetic dipole. Second, that Earth's magnetic dipole points along Earth's axis of rotation. Finally, that Earth's axis of rotation is perpendicular to the ecliptic plane. We shall define a coordinate system such that the positive x-axis points from the center of Earth to the center of the sun. The positive z-axis points along the dipole axis, and the y-axis completes the right-handed coordinate system. In our case this means that the positive y-axis is pointing from the center of Earth opposite the direction Earth orbits around the sun. We also define a corresponding spherical coordinate system were the azimuthal angle (φ) varies around the z-axis of the Cartesian coordinate system, with $\varphi = 0$ pointing to the sun and $\varphi = \pi/2$ pointing along the y-axis. We will further restrict our discussion to particles whose first adiabatic invariant is preserved, that is to say, whose magnetic moment, μ, is constant. This restriction, while it does simplify the math, is not significant as most particles in the magnetosphere do have invariant magnetic moments. In addition we will restrict the derivation to 90° pitch angle particles drifting in the equatorial plane, and assuming steady state electric and magnetic fields, these assumptions allow us to write the particle drift velocity as

$$\mathbf{v}_d = \frac{-\nabla\phi \times \mathbf{B}}{B^2} + \frac{\mu}{qB^2}\mathbf{B} \times \nabla B \tag{1.5}$$

where ϕ is the electric field potential ($\mathbf{E} = -\nabla\phi$) and $W_\perp$ is the perpendicular energy of the particle. Recall that a particle's magnetic moment is $\mu = W_\perp/B$. Therefore we can rewrite 1.5 as:

$$\mathbf{v}_d = \frac{1}{B^2}\mathbf{B} \times \nabla(\phi + \frac{\mu B}{q}) \tag{1.6}$$

We can define,

$$\tilde{\phi} = \phi + \frac{\mu B}{q} = \phi + W_\perp, \tag{1.7}$$

This potential is the path that the 90° equatorial particle drift follow. This parameter is the total energy of the particles. Therefore, the drift is energy conserving

We understand now what role the potential plays in determining the particle drift, but what form does this potential take? Within the magnetosphere there are two primary means by which an electric potential is imposed. The first of these is corotation. Collision of neutral atoms in the atmosphere forces the ionosphere to corotate, creating a corotation electric field. In the steady state magnetic field lines are equipotentials, causing the electric potential in the ionosphere to map down to the equatorial plane. However this is where our assumptions breakdown somewhat. In actuality the changes in convection are transmitted through magnetohydrodynamic waves and the associated Maxwell stress ($\mathbf{j} \times \mathbf{B}$). The other source of the electric potential is the convection from the night side to the day side of the planet. This convection is driven by reconnection with the IMF, and sunward convection returns magnetic flux that is in turn transported into the lobes via the reconnection process.

For corotation,

$$\mathbf{v}_{cr} = \hat{\boldsymbol{\varphi}} r \frac{2\pi}{\tau_d} \tag{1.8}$$

where $\tau_d = 86,400$ is the number of seconds in the day. Working backwards from this we see that the corresponding electric potential is:

$$\phi_{cr} = -\frac{2\pi}{\tau_d} B_0 r_0^2 (\frac{r_0}{r}) \tag{1.9}$$

In equation 1.8 we have retained our assumption of a dipole magnetic field described as $B = B_0 r_0^3 / r^3$. Referencing the International Geomagnetic Reference Field (IGRF) to specify the dipole magnetic field, the r_0 is the mean Earth radius (6371.2 km).

We can further define a parameter known as the corotation potential:

$$\phi_c = \frac{2\pi}{\tau_d} B_0 r_0^2 \tag{1.10}$$

Using the IGRF version 12 magnetic field for 2016, $B_0 = 29816$ nT and $\phi_c = 88.01 kV$.

For the reconnection-imposed convection we make the simplifying assumption that the electric field is uniform and points from dawn to dusk (positive-y direction):

$$\mathbf{E}_{conv} = \hat{\mathbf{y}} \frac{\phi_{pc}}{W r_0} \tag{1.11}$$

where ϕ_{pc} is the cross-polar-cap potential and W is a characteristic width of the magnetosphere, expressed in units of r_0. There are more sophisticated models of the convection electric field, for example the Volland-Stern model, where the convection electric field is shielded from the inner magnetosphere. But for the purpose of understanding how the plasmasphere arises from the interaction of the electric fields, the uniform electric field assumption is sufficient.

Now let us derive the potential corresponding to the electric field in 1.10 Combining this with the corotation potential, we get the total potential for the sunward convection and corotation:

$$\phi = -\phi_c(\frac{r_0}{r}) - \frac{\phi_{pc}}{W}(\frac{r}{r_0})\sin\phi \tag{1.12}$$

At any particular radial distance the potential is maximum at dawn ($\phi = -\pi/2$) and minimum at dusk ($\phi = \pi/2$). The potential lies between these two limits for any other local times.

For equatorial particles, then, from eq 1.7,

$$\tilde{\phi} = -\phi_c(\frac{r_0}{r}) - \frac{\phi_{pc}}{W}(\frac{r}{r_0})\sin\phi + \frac{\mu B_0}{q}(\frac{r_0}{r})^3 \tag{1.13}$$

or

$$\frac{\tilde{\phi}}{\phi_c} = -(\frac{B}{B+0})^{\frac{1}{3}} - \frac{\phi_{pc}}{W\phi_c}(\frac{B_0}{B})^{\frac{1}{3}}\sin\phi + \frac{\mu B_0}{q\phi_c}(\frac{B}{B_0}) \tag{1.14}$$

in eq 1.13 the magnetic moment is normalized to $\mu = q\phi_{pc}/B_0$. In SI units this parameter equals 2.948 $GeVT^{-1}$. By combining equations 1.4 and 1.12 the equatorial particle drift velocity is given by

$$\mathbf{v}_d = \frac{2\pi r_0}{\tau_d}\{\hat{\varphi}[(\frac{r}{r_0}) - \frac{\phi_{pc}}{W\phi_c}(\frac{r}{r_0})^3 \sin\phi - \frac{\mu B_0}{q\phi_c}(\frac{r_0}{r})] + \hat{\boldsymbol{r}}\frac{\phi_{pc}}{W\phi_c}(\frac{r}{r_0})^3 \cos\phi\} \tag{1.15}$$

If we consider the azimuthal component of eq. 1.15, the first term in the square brackets corresponds to corotation and the second corresponds to the $\varphi-$component of the sunward convection. The last term in the square brackets is the gradient drift. Note that the gradient drift of positive ions of the plasma is counter to the drift of corotation. Eq. 1.15 shows that the different drifts tend to dominate at different radial distances. At small radial distances, the gradient drift will tend to dominate; at large radial distances, sunward convection dominates; at intermediate distances, corotation is important. But, again, this is complicated by the dependence on the particle magnetic moment.

The radial component of eq. 1.15 shows that particles move to lower radial distance on the night side and higher radial distance on the dayside. this is to be expected since it is only the sunward convection that changes the radial distance of the particles. But the other aspect of this is that particles gain energy on the night side part of their drifts and lose energy on the dayside. This concludes our mathematical treatment of the plasmasphere, and how it arises from the basic processes occurring within the inner magnetosphere. For further discussion on the topic see [1].

Sunlight ionizes neutrals to create plasma in the day side ionosphere. This plasma will then flow up along the magnetic field lines which are approximately dipolar. At low latitudes this plasma becomes trapped between mirroring points. These particles form the plasmasphere. The velocity at which particles bounce between the mirror points is determined by its pitch angle. The pitch angle being the angle between the equatorial plane and particles velocity vector. Due to the frozen-in flux theorem the plasma trapped in the bounce motion will drift eastward following Earth's rotation as they gyrate around the magnetic field lines. The volume of space carved out by particles as they gyrate around a magnetic field line while undergoing the combined bounce motion and gyration is called a flux tube. The combination of these effects means that the plasmasphere looks like a tours.

On the night side the sun no longer ionizes neutrals to create plasma to fill the flux tubes. This causes flux tubes whose magnetic footprints map to magnetic field lines on the night side ionosphere to lose plasma, as the rate of loss due to particles being in the loss cone is now greater then the filling rate from the ionosphere. Over a long period of time the filling from the ionosphere on the day side dominates the loss rate due to loss cone scattering on the night side. This causes the plasmasphere to fill to a saturation density overtime. It takes about two weeks to reach this diffusive equilibrium.

1.3.1 Erosion and Refilling

During a magnetic storm several factors coincide to drive the draining of the plasmasphere. Due to the frozen in flux theorem the plasmasphere plasma will travel with the magnetic field lines as they undergo reconnection. The pressure balance between the solar wind and the magnetosphere will cause new magnetic field lines to be pushed to the reconnection point as the storm continues. This causes the plasma to form a plume of material going from the plasmasphere to the day side reconnection point. Beyond the frozen-in flux theorem there is another reason why the plasma forms a plume on the day side. When the IMF turns southward the balance between the Dawn-Dusk electric field and the corotation electric field changes, causing the boundary of closed drift paths to move much closer to Earth. This causes plasma in the plasmasphere, previously on closed drift paths to suddenly be on open drift paths. The plasma of course follows lines of constant equipotential, which look like a plume coming form the now smaller plasmasphere.

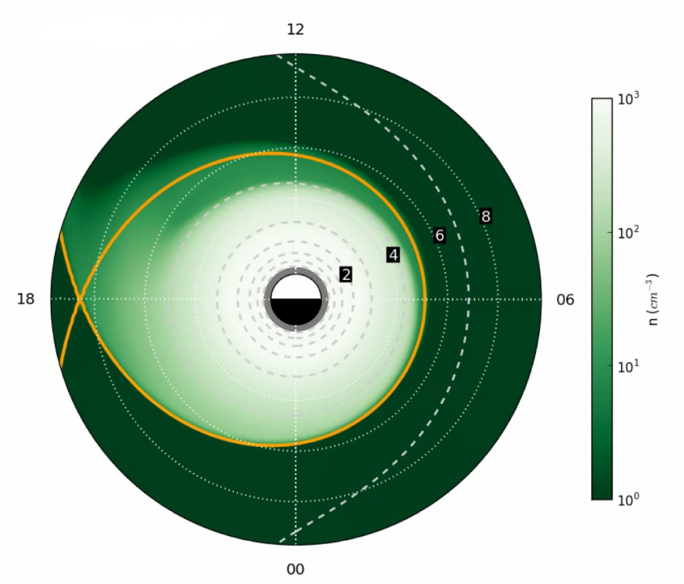

FIGURE 1.6: DGCPM simulation of the plasmasphere before the storm onset.

Figures 1.6 and 1.7 show the equatorial plasmasphere taken form a simulation using the Dynamic Global Core Plasma Model (DGCPM). We will get more depth on this model of the plasmasphere latter. DGCPM was configured to use the Volland-Stern empirical electric field model, which was parameterized on K_p. Therefore the simulation was not directly solar wind driven. K_p is an indication of the convection electric field and increases as the IMF turns southward, indicating a magnetic storm

As reconnection continues the outer flux tubes of the plasmasphere will be stripped away, draining the plasmasphere of material. My research deals with

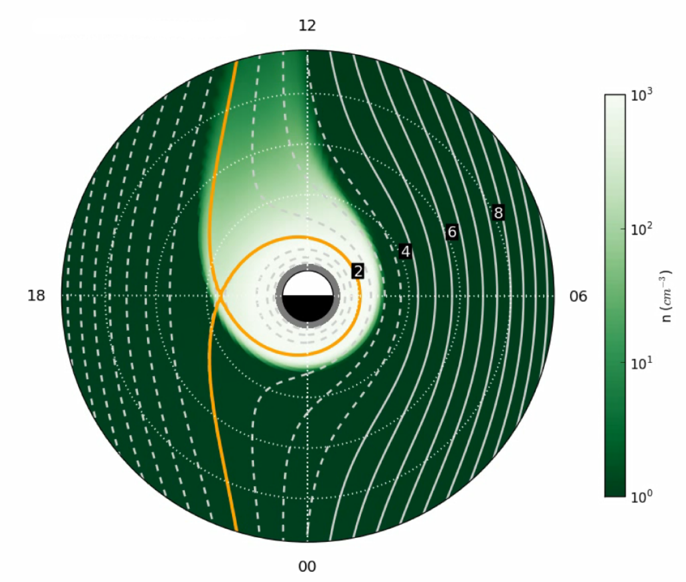

FIGURE 1.7: DGCPM simulation of the plasmasphere 6 hours after the storm onset.

the fate of the plasmasphere material that was stripped away, specifically if it is recaptured by night side reconnection (Figure 1.4 line 7) or lost to the solar wind (Figure 1.4 line 8). We will discuss this question, and the existing literature, in more detail latter. For now let us continue with our overview of the plasmasphere.

The refilling of the plasmasphere is driven by many complex process. These complexities have been studied by the use of single stream fluid models, two-streams fluid models, kinetic models, and observations. The plasma flow from the ionosphere along the flux tube is characterized by large scale phenomena. Plasma in the upper parts of the ionosphere is energized and flows out of the ionosphere along magnetic field lines. This process is dominated by large scale phenomena, while conversely, the trapping and thermalization of plasma in the equatorial plane is dominated by small scale phenomena involving plasma-plasma and wave-particle interactions. Figure 1.8 shows a schematic detailing various processes involved in the refilling of the plasmasphere. As the plasma flows up the flux tube from the ionosphere it is heated in the direction perpendicular to the magnetic field line. The ions are intensely heated in the equatorial plane resulting in an electric field point towards the ionosphere along the magnetic field line. The heating of the plasma in the equatorial plane, combined with the creation of an electric field pointed towards the ionosphere causes the plasma flowing from the ionosphere to slow creating a shock. The shock then propagates back towards the

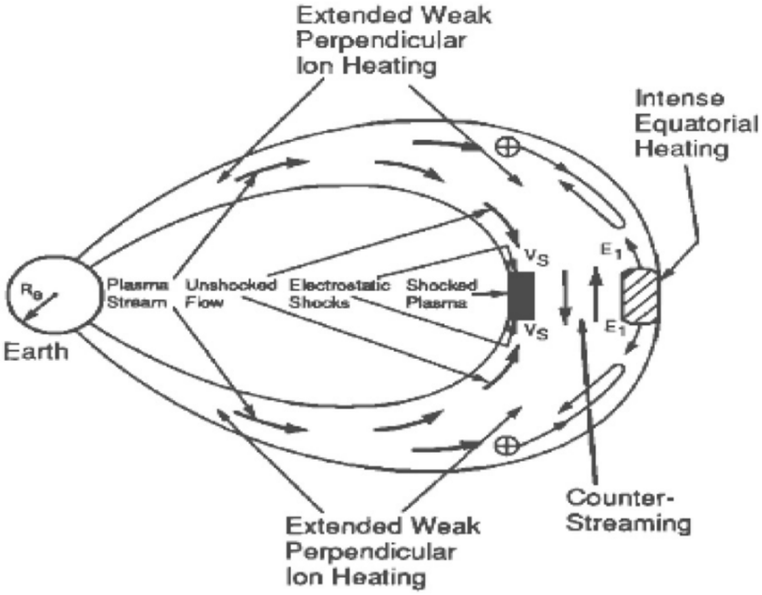

FIGURE 1.8: Various processes involved during refilling of the plasmasphere. Reproduced from [10] from Fig. 10.

ionosphere at the velocity v_s labeled in Figure 1.8. The electric fields will reflect the plasma streams coming from the ionosphere and slow the filling process. Singh and Horwitz 1998 and references therein discuss the processes involved in these interactions while Gallegher and Comfort 2016 discuss some of the open questions in regards to plasmasphere refilling, which is ultimately not well understood [8, 9].

1.3.2 Observations

There have been several missions throughout the years to study the plasmasphere. These include CLUSTER, and IMAGE among others. IMAGE and CLUSTER play a role in my research and so I will go into a primer on these missions here.

CLUSTER is a set of four satellites which orbit Earth roughly in its noon-midnight meridian plane. The space craft cross the plasmasphere near perigee around 4 Earth radii every 57 hours. On board the CLUSTER satellites are four sets of identical sensors. For the detection of the magnetic field the Flux Gate Magnetometer (FGM) is used. The electric field is measured by an electron beam drift experiment called Electron Drift Instrument (EDI). There are five experiments for measuring waves including: the Electrical Field and Wave (EFW), Digital Wave Processing (DWP), Spatio-Temporal Analysis of Field Fluctuations (STAFF), Waves of High frequency and Sounder for Probing the Electron Density by Relaxation (WISPER), and the WideBand Data (WBD) instrument. Three instruments are used for particle measurement: the Cluster Ion Spectrometer (CIS), Plasma Electron and Current AnalysEr (PEACE), and the Research with Adaptive Particle Imaging Detectors (RAPID) [11]. The WISPER instrument provides observations of the low frequency cut-off of natural plasma emissions, which operates between 2 and 90 kHz. With frequency resolution of 162 Hz WISPER provides 2-d view and lifetimes of global density structures, dynamics including resolution and lifetimes

[12, 13].

The Imager for Magnetopause-to-Aurora Global Exploration (IMAGE) is a single satellite dedicated to imaging Earth's magnetosphere. IMAGE has three plasma imaging techniques: neutral atom imaging, ranging from 10 ev to 500 keV, far ultraviolet imaging (FUV) at 121-190 nm range, extreme ultraviolet imaging (EUV) at 30.4 nm, and radio plasma imaging over the density range of .1 to 10^5 cm^{-3} through the magnetosphere [14, 15]. Nuetral atom imaging is managed by three different instruments to handle low-energy (LENA), medium-energy (MENA), and high-energy (HENA) due to technological reasons. Similiarly, for the FUV measurements three instruments are used, the Spectrographic Imager, the Wide-band Imaging Camera, and the Geocroonal Imager. The IMAGE satellite was launched into an elliptical orbit at 90-deg inclination with an apogee altitude of 7 R_E and perigee of 1000 km. For my research the EUV imager is the most important instrument as it is capable of imaging the plasmasphere [15].

1.4 Ring Current

The ring current is an electrically neutral current flowing toroidally west to east around Earth. Though the ring current is electrically neutral the charge is primarily carried by the ions, with typically energies of 1-30 keV. The ring current typically spans from 2 R_E to 9 R_E in the equatorial plane. The quiescent ring current is dominated by hydrogen sourced from the solar wind and the ionosphere. During quiet time the normal current density is 1-4 nA m^{-2}. During periods of strong geomagnetic activity increased outflow from the polar wind leads to the ring current being enhanced by an injection of O^+. The newly injected O^+ can comprise up to 50% of the ring current charge carrying ability. During storms the ring current can exceed values of 7 nA m^{-2}.

The ring current is the key part of geomagnetic storms near Earth. It is this current which decreases the horizontal component of the geomagnetic field strength at the surface of Earth. Intense geomagnetic storms, associated with strong ring currents, can have a drastic effect on technological systems, such as power lines and satellites. As such, understanding the ring current, how it is formed and evolves throughout a storm is critical. One area which is understudied, is the potential contribution of the plasmasphere plasma once it has been energized by recirculation. It is this overlooked potential contribution that is the focus of this work.

The ring current in its earliest form was first proposed by Schmidt (1917) [16] and Chapman (1919) [17] as an explanation of the observed decrease of Earth's magnetic field on the surface during geomagnetic storms. They proposed a singularly charged stream originating from the sun. During the 1930s further work by Chapman and Ferraro refined the concept to a transient stream of out flowing solar ions and electrons Chapman and Ferraro (1930) and (1931) [18, 19]. They proposed that when the stream reached Earth particles from it would leak into the magnetosphere and being to orbit creating the ring current. Parker (1958) [20] renamed this transient stream the solar wind, as he realized that it was continuous, rather than transient. From there the basic concept of the ring current has persisted to this day.

Dessler and Parker (1959) [21] and Sckopke et al. (1966) [22] showed the magnetic disturbance ΔB of the apparent magnetic field at the surface is proportional to the energy of the ring current particles:

$$\frac{\Delta B}{B_0} = \frac{2E}{3E_m} \tag{1.16}$$

where B_0 is the average surface geomagnetic field intensity at the equator, E is the total energy of the ring current particles and E_m is the energy of Earth's dipole field above Earth's surface. In our case $E_m = B_0^2 R_E^3/3$ which according to [23] is on the order of 10^{18} J.

The generalized Dessler-Parker-Sckopke relation includes terms from internal and boundary sources:

$$\frac{B_D}{B_0} = \frac{2E + M - \oint \mathbf{R} \cdot \mathbf{n} d\sigma}{3E_m} \tag{1.17}$$

where B_D is the field decrease due to the combined magnetic field from all sources including the ring current, the magnetopause current and the magnetotail current. M is the total magnetic energy inside the magnetosphere, that is the volume integral of $B_D^2/2\mu_0$. The unit vector **n** is the outward pointing normal, and **R** is,

$$\mathbf{R} = (p + \frac{B^2}{2\mu_0})\mathbf{r} + \rho(\mathbf{V} \cdot \mathbf{r})\mathbf{V} - \frac{(\mathbf{B} \cdot \mathbf{r})\mathbf{B}}{\mu_0} \tag{1.18}$$

where p is the thermal pressure assumed to be isotropic, **r** is the radius vector from the center of Earth, ρ is the mass density of the solar wind in the plasma mantle, **V** is the flow velocity of the mantle plasma, and **B** is the total magnetic field vector.

The Dessler-Parker-Sckopke demonstrates that the energy of the ring current has a direct affect on the apparent magnetic field at the surface of Earth. As such understanding the plasmasphere's contribution to the ring current is an important aspect of properly understanding the ring current and the affects of the near-Earth space environment on our planet. However, the exact nature of the coupling of the plasmasphere and ring current is beyond the scope of this dissertation. This work is focused on the question of the recirculation of plasmaspheric material during geomagnetic storms, and how the pre-storm space environment affects recirculation, if it occurs.

1.5 History of Plasmasphere Recirculation

The recirculation of the plasmasphere was first proposed by Freeman et al. (1977) [24]. That paper proposed that the plasmaspheric material may either recirculate over the poles and-or around the flanks. Borovsky et al. (1997) [25] estimates that the plasmasphere can provide up to twice the needed material to explain the super dense plasma sheet. A six-step process was proposed by which the plasmaspheric material can recirculate over the poles. Using satellite data from four LANL-MPA instruments, it was demonstrated that plasmaspheric material does undergo the first three steps of the proposed six-step process. However, due to the orbits of the LANL satellites being used it was not possible to demonstrate conclusively that the plasmaspheric material went any further then step three of the six. Borovsky notes that the conditions necessary for the six-step process would also allow the penetration of solar wind into the plasma sheet, making it difficult to determine if observed material in the tail is of plasmasphere or solar wind origin [25]. Daglis et al. (1999) [26] demonstrated ring current ions primarily come from the plasma sheet and the solar wind. However, the plasma sheet is itself fed by the high latitude ionosphere and the solar wind. Thus, the ultimate source of ring current particles is the high latitude ionosphere and solar wind . Su et al. 2001[27] demonstrated that plasmasphere material could be located on high-latitude open field lines in some cases, finding it twice in a sampling of 21 events.

Simulations and models have also been used to investigate this issue. Elphic et al.(1997) [28], used the Weimer 1996 [29] and Tsyganenko 1989 [30] models to track magnetic flux tubes by following their foot points in the ionosphere. Elphic found that in storm conditions the magnetic field flux tubes representing plasmasphere flux tubes did recirculate over the poles and not around the flank as was thought possible by Freeman. This study was limited as it did not include the recursive effects of the plasma being transported and included only one simulated event. Moore et al. (2008) [31] used the Lyon-Fedder-Mobarry (LFM) [32] to trace test particles that were given initial velocities and energies representative of the plasmasphere by the coupled Comprehensive Ring Current Model (CRCM). The contribution to the ring current of test particles that recirculated back into the region of the CRCM was then compared to the contribution to the ring current from other populations. It was found that the plasmasphere contributed about the same to the ring current as the polar wind, though its contribution lagged by about an hour, and that the plasmasphere contributed less then the solar and auroral wind sources. The Moore et al. (2008) study was limited by a lack of self-consistency. The plasmaspheric particles in the LFM portion were test particles, and the ionosphere particles in the CRCM portion were not coupling to the LFM model. It was suggested that treating the plasmasphere particles self-consistently and including the ionosphere particles in the LFM/CRCM coupling could substantially change the results.

Using observations to resolve the issue is difficult due to the composition of the plasma from the solar wind, plasmasphere, and ionosphere, which are all dominated by hydrogen as well as the large-scale nature of the problem. Until recently, simulations have not been up to the task of tracking multiple populations of ions in the magnetosphere on a global scale, due both to a lack of computational power and the outer boundary of dedicated of plasmaspheric codes typically being placed at 10 R_E, which is to close to Earth to capture recirculation of the plasma. However, recent advancements both in modeling approaches and computing power have made it possible to study the fate of plasmaspheric material on a global scale in numerical simulations.

This thesis presents two simulations using the Space Weather Modeling Framework in a novel configuration to study the fate of plasmaspheric material during magnetic storms. The simulations approach the recursive relationship of the inner magnetosphere and solar wind coupling from a self-consistent manner. This will enable us to address the fate of the plasmasphere once it enters to solar wind, and begin to resolve the outstanding question.

1.6 Science Questions

This work will explore the question of whether plasmasphere material will recirculate during a geomagnetic storm through the use of simulations utilizing the Space Wheater Modeling Framework (SWMF). I will demonstrate that recirculating plasmasphere material can be a significant contributor to the plasma within the inner magnetosphere. I will examine under what conditions this contribution can be significant and how factors such as the initial condition of the plasmapshere and solar wind affect this contribution. I will discuss the mechanisms, both psychical and model based, by which the results presented can, or have been, achieved. Finally in regards to work completed I will discuss the weakness of the work, and how they can be rectified in the future.

I will also discuss what work is currently being done to advance the science demonstrated here in. I will present the development of the SWMF and integral models whose newly added capabilities will be able to close the gaps left in the completed work from a modeling prospective. We will discuss in detail how to properly validate model development, including sanity checks, test cases, and comparison to well verified results among other techniques.

Chapter 2

Models

2.1 Space Weather Modeling Framework

Various domains of the Earth-Sun system can be simulated with stand-alone models. Simplifying assumptions made about the interaction of the particular domain with the rest of the system, or the use of satellite and ground-based measurements can plug the gaps in any given standalone model. The Space Weather Modeling Framework (SWMF) however aims to enable the simulation all the relevant domains from a first-principles-based physics models. The SWMF accomplishes this by coupling together models dedicated to a particular domain of the Sun-Earth system and ensuring their execution in an efficient manner [33].

The SWMF was developed at the University of Michigan during the mid-2000s. SWMF is often conflated with BATS-R-US, as both codes were developed at the

University Michigan; the SWMF following BATS-R-US. However, the SWMF is a framework, not a model. A framework is a reusable system design, which aims at coupling together multiple models via standardized interfaces. The framework makes the integration, extension, modification, and use of the coupled system easier than for a monolithic code or a system of models coupled in an ad hoc manner. The SWMF aims to integrate state-of-the-art models with a minimal change to the models without sacrificing the efficiency of the code [34]. Typically there is a balance between not altering the base code to be integrated and the efficiency of the SWMF. As the SWMF has been designed with real-time space weather prediction in mind, efficiency of the SWMF is often chosen over keeping a model in its base state. As such, there is an initial time investment into making a model compatible with the SWMF. This initial investment is typically measured in weeks for one or two people.

The SWMF is broadly organized into four layers. The top layer being the user interface. The SWMF is primarily interacted with through a command line prompt. Generally speaking, the user first configures the SWMF with the desired physics modules with high level information, such as which planet the simulation takes place around, or what species, fluids, or populations are being included. Next the user constructs a parameter file which exercises considerable control over how the simulation runs, including start stop time, input files to be read, more detailed configuration of included models, and how to split the load over the computer architecture if run in parallel among other settings. The second layer is the control module. The control module is responsible for distributing the calculation load over the various nodes of a parallel architecture, executing the models, and coupling them at the correct frequencies. The third layer is the physics models themselves. To be integrated into the SWMF these models must be modified with a wrapper with which the control module can interact with the physics model. The fourth and final layer is the shared library which stores routines common to all levels of the SWMF and physics models to reduce the amount of replicated code. An executable can be created for a given configuration of the SWMF which can then be placed in a directory with the parameter files to begin actual execution of the simulation. Extensive documentation provided with the SWMF, and numerous examples of parameter files for various configurations, makes running the SWMF relatively easy. Additionally, the SWMF is available at CCMC for those without the ability to run the code themselves [34].

Currently there are 15 physics domains within the SWMF. Depending on specific choices of domains, or choice of models within a given domain, various amounts of overlap occurs. The currently included domains, in no particular order, are: Convection Zone (CZ), Global Magnetosphere (GM), Eruptive Event Generator (EE), Solar Corona (SC), Inner Heliosphere (IH), Outer Heliosphere (OH), Ionosphere Electrodynamics (IE), Inner magnetosphere (IM), Particle Tracker (PT), Particle-in-Cell (PC), Plasmasphere (PS), Polar wind (PW), Radiation Belt (RB), Solar Energetic Particles (SP), and the Upper Atmosphere (UA). A simulation can be preformed with any given, physically meaningful, combination of the above domains.

For this work the SWMF has been configured in two ways. For the Published Simulations Chapter the SWMF was configured to couple the Block-Adaptive-Tree-Solar-Roe-Upwind-Scheme (BATS-R-US) (GM), the Dynamic Global Core Plasma Model (DGCPM) (PS), and the Ridley Ionosphere Model (RIM) (IE). In the Chapter 'Developing CIMI for use in Plasmasphere Recirculation Research' the SWMF is configured to couple BATS-R-US (GM), the Comprehensive Innermagnetosphere-Ionosphere Model (CIMI) (IM), and RIM (IE). While each of these models and some aspects of their coupling are discussed in detail latter, we will cover the basics of the coupling presently. For the PS to GM coupling the density of the plasmasphere is passed to the GM component which nudges its solution for the density of the plasmasphere towards the same value on closed field lines such that they converge rapidly. There is no GM to PS coupling. The GM to IE coupling consists of the GM component giving the field aligned currents to the IE component. As there is not a coupled UA component the Hall and Pederson currents are derived from the solar flux and auroral patterns. The IE to GM coupling consists of passing the electric potential to the other component. This electric potential is used to calculate the E x B velocity at the inner boundary of the GM component. The IE to PS coupling consists of the same information, the electric potential; however here it is used to generate the electric field in the equatorial plane by mapping along Earth's magnetic field lines. This coupling does assume that the field lines are equipotential. There is no PS to IE coupling. In our second configuration, the GM to IM coupling is the most computationally taxing. This cost is due to the requirement of tracing out the full 3D magnetic field lines in the GM component so that the 3D grid of the GM component can be properly mapped onto the IM grid for applying corrections to the density and pressure. As the GM component is normally spread over many processors in a parallel execution of the code this adds additional overhead to the operation as many processors must coordinate between themselves. To help deal with this the 3D tracing performed by the GM component uses interpolations at the block boundaries of the grid. The IM to GM coupling is also taxing on the computer. The IM component needs the full volume of the 3D flux tube from GM with the density and pressure in the flux tubes so that they can be interpolated onto its own 2D spherical-shell grid [33]. Obtaining this information requires accurate integration along many thousands of field lines on the distributed 3D grid. This coupling provides an insight into the type of work the shared library layer of the SWMF does, in that it is this layer which handles the exchange of information and collection of data between the different processors running the GM component. Toth et al. (2005) provides an explanation of an algorithm which allows the IM to GM coupling to occur in a fraction of a second [33].

The major underlying assumption of the SWMF is that it is possible to bridge the gap between vastly different physics domains in both a reasonable amount of time and across vastly different scales. The other option to that of a framework is a monolithic code. While the uniformality of a monolithic code might be desirable the SWMF has compared favorably to these codes in several studies. The major validation studies of the SWMF are covered in Tóth et al. 2005, Yu et al. 2008, Wang et al. 2008, Pulkkinen et al. 2013, Glocer et al. 2016, and Sachdeva et al. 2019 [33, 35–39].

2.2 Block-Adaptive-Tree-Solar-Roe-Upwind-Scheme

The Block-Adaptive-Tree-Solar-Roe-Upwind-Scheme (BATS-R-US) is a multi-fluid, multi-species, global ideal magnetohydrodynamic code. The fundamental object within BATS-R-US is a fluid packet within a finite volume. For this fluid packet various values, called primitive variables, are calculated descriptive of the state of a plasma which the fluid is assigned to represent. The primitive variables are the density, x-, y-, and z-components of momentum, the x-,y-, and z-components of the magnetic field and the total plasma energy. BATS-R-US can perform these calculations for an arbitrary number of fluids. BATS-R-US can keep track of the primitive variables separately for each fluid, while allowing the fluids to interact within a block. Therefore, even if two fluids mix BATS-R-US maintains an ability to distinguish them. The ability to simulate multiple fluids allows each fluid to either represent different species (i.e. H^+, He^+, O^+ etc.) or different populations of the same species, for instance the solar wind and polar wind. BATS-R-US is a global code, meaning that it simulates the entire computational domain with ideal magnetohydrodynamic equations. These equations are solved within each block volume for each fluid present in that block. Because BATS-R-US uses a Riemann type solver every fluid must have a non-zero density and temperature throughout the domain. However, it is possible to assign values to fluids such that they are non-significant in regions of the computational space which are appropriate to which plasma they represent with out affecting the MHD calculation.

As stated above BATS-R-US solves the magnetohydrodynamic equations for each fluid within a block. BATS-R-US has the ability to dynamically refine its cells, increasing resolution in areas of interest and decreasing resolutions elsewhere. It does this through the use of Adaptive Mesh Refinement (AMR) [40]. The user specifies some initial grid resolution. By comparing either geometric qualities of a block or comparison of the local flow quantities to a threshold value, a decision to coarsen or refine the grid can be made. Refinement takes the form of splitting a block into octants. Each octant, or offspring, inherits its initial values for the primitive variables from the parent block, but is then allowed to evolve them separately from its siblings. The coarsening of the grid is the inverse operation, in which eight neighboring blocks combine to form a new larger block. A tree structure is used to keep track of the adaptive mesh. Every block in the mesh is treated as a leaf, the end point of a series of branches leading back to some initial uniform coverage of the grid. Each time a refinement is made the block being refined, represented by a leaf, becomes a branch; and the offspring blocks created by the refinement become leaves on this new branch. When coarsening occurs leaves are pruned from a branch, and the branch reverts to being a leaf on some lower level branch. This tree structure makes it simple to decompose the domain. In addition, by ensuring that each processor in a parallel computation has an equal number of blocks the AMR approach also simplifies load-balancing [34]. Figure 2.1 gives a graphical representation of the Block-Adaptive-Tree.

In BATS-R-US the typical choices of refinement rely on local measures of compressibilty, rotationality, and current density. The cell volume, V, is used to scale the pre-selected values, which allows them to be used to resolve both smooth regions of the flow as well as discontinuous ones.

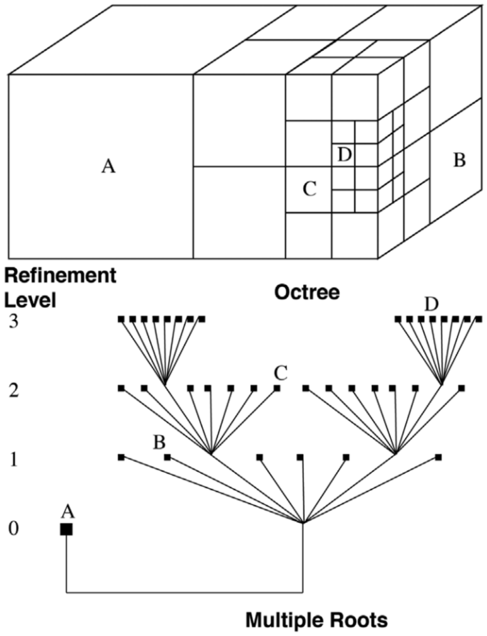

FIGURE 2.1: Adative Mesh Refinement and Tree data structre. This image is Figure A.2. reproduced from [34].

$$\epsilon_c = |\nabla \cdot \mathbf{u}|\sqrt{V} \tag{2.1}$$

$$\epsilon_r = |\nabla \times \mathbf{u}|\sqrt{V} \tag{2.2}$$

$$\epsilon_t = |\nabla \times \mathbf{B}|\sqrt{V} \tag{2.3}$$

BATS-R-US solves the ideal MHD equations in three dimensions. These ideal MHD equations are statements on the conservation of mass, momentum, energy, and Faraday's law. Only a single equation is required for the conservation of mass and energy while three equations are required to resolve the conservation of momentum and Faraday's law for an ideal, inviscid, perfectly conducting, non-relativistic fluid. The primitive variables formally stated are:

ρ	density
ρu_i	Momentum
B_i	Magnetic Field
E	Total Plasma Energy

TABLE 2.1: Primitive variables solved for by BATS-R-US. i represents the x,y, or z component.

where,

$$E = \rho e + \rho\frac{\mathbf{u} \cdot \mathbf{u}}{2} + \frac{\mathbf{B} \cdot \mathbf{B}}{2\mu_0} \tag{2.4}$$

where μ_0 is the permeability of vacuum, and e is the ideal-gas equation of state:

$$e = \frac{p}{(\gamma - 1)\rho} \tag{2.5}$$

where γ is the ratio of the specific heat. Equation 2.5 is used to relate pressure and energy. Ampère's law is used to relate magnetic field and current density.

Adapting the presentations in Powell et al. (1999) and Gombosi et al. (2021), the ideal MHD equations solved by BATS-R-US take the following form: [34, 41]

$$\frac{\partial \overline{\mathbf{U}}}{\partial t} + (\overline{\nabla} \cdot \overline{\overline{\mathbf{F}}})^T = \overline{\mathbf{S}} \tag{2.6}$$

where $\overline{\mathbf{U}}$ is the vector of conserved quantities defined by

$$\overline{\mathbf{U}} = (\rho, \rho u_x, \rho u_y, \rho u_z, B_x, B_y, B_z, E)^T \tag{2.7}$$

where u_i are the components of the bulk flow velocity vector, $\overline{\mathbf{u}}$. The flux tensor $\overline{\overline{\mathbf{F}}}$ can be written as:

$$\overline{\overline{\mathbf{F}}} = \begin{pmatrix} \rho\overline{\mathbf{u}} \\ \rho\overline{\mathbf{u}\mathbf{u}} + (p + \frac{\overline{\mathbf{B}}\cdot\overline{\mathbf{B}}}{2\mu_0})\overline{\overline{\mathbf{I}}} - \frac{\overline{\mathbf{B}\,\mathbf{B}}}{2\mu_0} \\ \overline{\mathbf{u}}\overline{\mathbf{B}} - \overline{\mathbf{B}}\overline{\mathbf{u}} \\ \overline{\mathbf{u}}(E + p + \frac{\overline{\mathbf{B}\,\mathbf{B}}}{2\mu_0}) - \frac{(\overline{\mathbf{u}}\cdot\overline{\mathbf{B}})\overline{\mathbf{B}}}{\mu_0} \end{pmatrix}^T \tag{2.8}$$

Finally, $\overline{\mathbf{S}}$ is a 'source' vector, containing the terms that cannot be expressed in divergence form:

$$\overline{\mathbf{S}} = -\overline{\nabla} \cdot \overline{\mathbf{B}} \begin{pmatrix} 0 \\ \overline{\mathbf{B}} \\ \overline{\mathbf{u}} \\ \overline{\mathbf{u}} \cdot \overline{\mathbf{B}} \end{pmatrix} \tag{2.9}$$

The source term, $\overline{\mathbf{S}}$, can be handled in two ways. The first method is a direct application of Maxwell's equation. The statement $\nabla \cdot \mathbf{B} = 0$, the absence of magnetic monopoles, leads cleanly to $\overline{\mathbf{S}} \equiv 0$. The simple solution however raises problems in solving the larger problem. Setting $\overline{\mathbf{S}}$ to zero results in a degenerate eigensystem for equation 2.6 [42]. BATS-R-US deals with this by formally keeping the $\overline{\nabla} \cdot \overline{\mathbf{B}}$ term in equation 2.9 and makes it passively convected. This method both resolves the degeneracy and creates an 8th wave which carries information about the discontinuity in the normal component of the magnetic field. Toth et al. 2000 studied the so called '8-wave scheme' and found it performed as well as other methods, which typically advanced the magnetic field separately [43].

Equation 2.6 represents a system of equations solving for the time rate of change of a conserved quantity in a finite volume, a block, by finding the flux of that quantity through the surface of the block. The equations are solved for each face separately, thus the equation integrated over the surface of a single cell takes the form:

$$\frac{d\mathbf{U}_i}{dt}V_i + \oint_{\partial(celli)} \mathbf{F} \cdot \hat{\mathbf{n}} dS = \mathbf{S}_i V_i \tag{2.10}$$

where V is the volume of the cell, $\hat{\mathbf{n}}$ is the normal vector pointing outward from the surface of integration. In this representation $\mathbf{U}_i$ and $\mathbf{S}_i$ are the cell-averaged conserved variables and source terms for the i^{th} cell.

There are several other complicating factors in the calculation, however this section is meant to introduce the model at a high level. For the interested reader Powell et al. (1997), De Zeeuw et al. (2000), and references therein gives a detailed discussion on how equation 2.10 is derived from first principals and how several other computational concerns where resolved [41, 44].

2.3 Ridley Ionosphere Model

The Ridley Ionosphere Model (RIM) solves for the height integrated electrodynamics of the ionosphere in an electrostatic frame. RIM was developed by A.J. Ridley at the University of Michigan during the development of BATS-R-US. As such the code was made with coupling to BATS-R-US in mind, though it was developed a little before the SWMF was created. During this period RIM was integrated with BATS-R-US and the codes ran as a monolithic fashion. There are several early papers which discuss the development of RIM, namely Ridley et al. 2002a, 2003, and 2004 [45–47]. The first study, Ridley et al. 2002a, focused on the influence of ionospheric outflow on the time-dependent magnetospheric configuration. The second study, Ridley et al. 2003, focused on how the thermospheric neutral winds effect the ionospheric electric field and magnetospheric convection. The final study, Ridley et al. 2004, examined the influence of the ionospheric conductance on the magnetospheric configuration.

Ionospheric conductance is strongly driven by extreme ultraviolet radiation. As sunlight ionizes the neutrals in the atmosphere, the atmosphere's ability to carry an electric charge changes. Moen and Breeke (1993) [48] first derived an empirical relationship between f10.7, solar zenith angle and ionospheric conductance. f10.7 is a measure of the amount of solar flux at a particular wave-length and serves as a proxy for the intensity of EUV radiation. The solar zenith angle is the angle between the sun, from the perspective of a viewer on the ground, to the highest point of the sky. As solar zenith angle increases the solar flux is spread over a wider area of sky, decreasing the production of ions at high latitudes. As such, the conductance of the ionosphere is strongest at low latitudes on the day side and becomes progressively weaker as you move both nightward and poleward. When RIM was initially developed, Ridley used a map of Hall and Pedersen conductances derived using the Assimilative Mapping of Ionospheric Electrodynamics (AMIE) method [49]. During that development only one month of data was used to construct the conductance map. However, in 2020, Mukhopadhyay et al., found a new set of Hall and Pedersen conductances which improved the skill score of dB/dt predictions using the SWMF during extreme events by using non-linear regression to span minute resolution AMIE data spanning the whole year of 2003 [50]. However, the simulations reported in Chapter 4 were conducted before Mukhopadhyay et al. 2020 published the Conductance Model for Extreme Events (CMEE), and as such we use the Ridley numbers. Later in Chapter 5 however we do switch to using the Mukhopadhyay 2020 conductance tensor for the configuration of RIM.

The Ridley et al. 2004 study discusses how RIM solves for the potential of the ionosphere. When RIM is integrated as part of the SWMF it is this conductance, which leads to electric potential, which leads to the $\mathbf{E} \times \mathbf{B}$ drift at the inner boundary or the convection electric field, which the other models require. As such we will follow its presentation of the calculation of the electric potential briefly.

Ionospheric conductivity changes as both a function of altitude and the ratios of the ions, electrons, and neutrals to each other. In the E-layer of the ionosphere, between 100 km to 150 km the ratio of ions to neutrals means that an ion will collide with neutrals several hundred times per gyro-radius. The high ratio of ions to neutrals means that the ions will cease their $\mathbf{E}\times\mathbf{B}$ drift and move only along the electric field. $\mathbf{E}$. Meanwhile, due to a smaller physical size the electrons are still few enough, relative to the neutrals, that they will go for many hundreds of gyroperiods before colliding with a neutral. Therefore, the electrons will continue to follow an $\mathbf{E}\times\mathbf{B}$ drift. The difference in the motion of the ions and electrons in this region of the ionosphere gives rise to the Pedersen and Hall currents respectively [4].

The Ridley Ionosphere Model functions according to the following algorithm. The field-aligned currents (FACs) are calculated in BATS-R-US. The FACs are then scaled along a dipole magnetic field from 3.5 $\mathrm{R_E}$ to 150 km above the Earth's surface. This mapping of the FACs is done in such a way as to conserve current continuity. The conductance values for various points in the ionosphere are found based on the methods described above. A poisson like equation is solved for the electric potential in the ionosphere using the scaled FACs and conductance values as inputs. After the electric potential has been found, it is then scaled back to the inner boundary of BATS-R-US, 2.5 $\mathrm{R_E}$. The potential is then used to calculate the electric field, and from it, the $\mathbf{E}\times\mathbf{B}$ velocity of the plasma. The $\mathbf{E}\times\mathbf{B}$ value is used as an inner boundary condition for BATS-R-US. RIM will also use the electric potential and derived electric field to set the electric field of the Dynamic Global Core Plasma Model (DGCPM) and Comprehensive Inner Magnetosphere

Ionosphere Model (CIMI), which will be discussed in latter sections [47].

The poisson like equation solved by RIM can be represented, according to Amm et al. (1996) [51] as:

$$\begin{aligned} j_R(R_I,\theta,\psi) = {} & \frac{1}{R_I^2}\frac{\delta^2\Phi}{\delta\theta^2}\frac{\Sigma_0\Sigma_P}{C} + \frac{1}{R_I^2}\frac{\delta^2\Phi}{\delta\psi^2}\left\{\frac{1}{\sin^2\theta}\left(\Sigma_P + \frac{\Sigma_H^2\sin^2\epsilon}{C}\right)\right\} + \\ & \frac{1}{R_I^2}\frac{\delta\Phi}{\delta\theta}\left\{\frac{\delta}{\delta\theta}\left(\frac{\Sigma_0\Sigma_P}{C}\right) + \cot\theta\frac{\Sigma_0\Sigma_P}{C} + \frac{1}{\sin\theta}\frac{\delta}{\delta\psi}\left(\frac{\Sigma_0\Sigma_H\cos\epsilon}{C}\right)\right\} + \\ & \frac{1}{R_I^2}\frac{\delta\Phi}{\delta\psi}\left\{\frac{\delta}{\delta\theta}\left(\frac{\Sigma_0\Sigma_H(-\cos\epsilon)}{C\sin\theta}\right) + \frac{1}{\sin^2\theta}\frac{\delta}{\delta\psi}\left(\Sigma_P + \frac{\Sigma_H^2\sin^2\epsilon}{C}\right) + \frac{\Sigma_0\Sigma_H(-\cos\epsilon)\cot\theta}{C\sin\theta}\right\} \end{aligned} \tag{2.11}$$

where,

$$C = \Sigma_0\cos^2\epsilon + \Sigma_P\sin^2\epsilon \tag{2.12}$$

ϵ is the angle between the radial direction and the magnetic field, θ is the colatitude, and Σ_0, Σ_H, and Σ_P are field-aligned, Hall, Pedersen height integrated conductances, respectfully. Equation 2.11 makes no assumptions about the spatial distribution of conductances, the magnetic field, or the electric potential. Within BATS-R-US, Σ_0 is given as a constant value of 1000 mhos [47].

The electric potential is solved independently in both hemispheres. A preconditioned gradient reduction resolution (GMRES) solver is used to solve for the electric potential [47]. This solver is analogous to the Roe-solver in BATS-R-US, in that it is the algorithm which does the bulk of the computation. GMRES is robust enough to handle the various field-aligned currents and ionospheric conductances found in the ionosphere [47].

RIM runs on a simple ionosphere grid, with a grid resolution of 2 degrees in latitude and 1 hour in MLT [52]. As stated above, the physics which RIM is interested in occurs between 100 km and 150 km. As such, it is a two dimensional grid relaying on other models coupled through the SWMF to remove the need for a third dimension. RIM can couple to a dedicated upper atmosphere code if the user wishes to simulate lower altitudes then what RIM is set to (150 km for this work). Coupling to an upper atmosphere code would be done to derive the Hall and Pedersen conductances from the chemistry of the upper atmosphere [33]. In this study, we use both the default Ridley conductance grid and the CMEE values produced by Mukhopadhyay et al. 2020. Ridley's numbers are used for the Chapter 4 while Mukhopadhyay's work is utilized in Chapter 5 For altitudes higher then 150 kilometers the physics more closely resembles MHD, and as such the upper boundary for RIM is taken by mapping BATS-R-US values along the magnetic field lines to the appropriate altitude.

RIM is not a time accurate code. For any given set of inputs, FAC, f10.7 etc. RIM checks after coupling to another model if the information coming in from that model has changed. In the event that it has changed, RIM will advance to the current time of the coupling component, update the values of coupled variables, and resolve its equations with this updated information. RIM will then remain in this state until the next time it couples.

2.4 Comprehensive Inner Magnetosphere-Ionosphere Model

The Comprehensive Inner Magnetosphere-Ionosphere Model (CIMI) was developed by M.C. Fok at the NASA Goddard Space Flight Center in 2014. CIMI was created by combining the Comprehensive Ring Current Model (CRCM) and Radiation Belt Environment (RBE) models to serve as a base, and adding additional capabilities on top. CRCM was developed in 2001 to solve the ring current particle distributions and to consider the closure of electric current between the magnetosphere and the ionosphere [53]. CRCM contains an embedded plasmasphere model, a modified DGCPM. This internal plasmasphere is driven by the electric field calculated from CRCM. By coupling with ionosphere codes CRCM could reproduce features of the plasmasphere such as drainage plumes and the propagation of undulations from the night side to dayside local times [54, 55]. RBE was similarly developed by M.C Fok in 2001 to calculate radiation belt particle fluxes and to predict their variations during active times [56]. The RBE model calculates the distribution functions of 10 keV to 4 MeV electrons and considers diffusive interactions with whistler mode chorus waves. The model has been successful in reproducing observed features of substorms including dispersionless injection and drift echoes. Both CRCM and RBE are well-established models. However each has short comings. RBE, in the early days, used empirical electric field models [57]. CRCM assumed the loss rate of electrons was a simple fraction of the strong diffusion rate [58]. By combining CRCM and RBE these models cover each other's weakness while maintaining their own merits. The self-consistent electric field model provides an improved distribution function for ring current electrons, which are the seed population for radiation belt electrons, with a precise treatment of wave-particle interactions. The convection model and wave diffusion for the ring current electrons result in a realistic electron precipitation pattern in the ionosphere, which in turn modifies the ionosphere conductance and convection pattern. Thus, the new CIMI model provides a self-consistent representation of the inner-magnetosphere, calculating the distribution functions of ring current ions and electrons, region 2 field-aligned currents, radiation belt electrons, electron precipitation into the ionosphere, plasmaspheric density, and the subauroral convection field.

CIMI solves three basic equations, the first of these describes the distribution function.

$$\frac{\partial f_s}{\partial t} + \langle\dot{\lambda}_i\rangle\frac{\partial f_s}{\partial \lambda_i} + \langle\dot{\phi}_i\rangle\frac{\partial f_s}{\partial \phi_i} = \frac{1}{G}\frac{\partial}{\partial \alpha_o}[G(D_{\alpha_o\alpha_o}\frac{\partial f_s}{\partial \alpha_o} + D_{\alpha_o E}\frac{\partial f_s}{\partial E})] + \frac{1}{G}\frac{\partial}{\partial E}[G(D_{EE}\frac{\partial f_s}{\partial E} + D_{E\alpha_o}\frac{\partial f_s}{\partial \alpha_o})] - v\sigma_{sH}\langle n_H\rangle f_s - (\frac{f_s}{0.5\tau_b})_{losscone} \tag{2.13}$$

where G,

$$G = T(\alpha_o \sin(2\alpha_o)(E + E_o)\sqrt{E(E + 2E_o)} \tag{2.14}$$

Equation 2.13 solves for the average distribution function, $f_s = f_s(t, \lambda_i, \phi_i, M, K)$, between the mirror points on a specified field line. The field lines are indexed by the subscript i, and kept track of by their footprints in the ionosphere. λ_i is the magnetic latitude of the base of a field line, while ϕ_i is the local time at the base of the field line. M is defined to be the relativistic magnetic moment, and $K = J/\sqrt{8}m_o M$ where J is the second adiabatic invariant. The inner boundary of the model is set at 12°, which corresponds to an L-shell of $L = 1.06$ when Earth's magnetic field is well approximated as a dipole. The outer boundary is set to 10 Earth radii ($\mathrm{R_E}$) or a magnetic latitude of 70.3°, which ever is closest. The outer boundary is determined either by an empirical plasma sheet model, or coupling with an MHD model. For this work, the outer boundary is set by coupling with BATS-R-US. E_o is the rest energy, α_o represents the equatorial pitch angle and $T(\alpha_o)$ is a function depending on α_o and the shape of the field line.

Particle drift is represented on the left hand side of 2.13 while the right hand side represents the diffusion and loss processes present in the plasmasphere.$\langle\dot{\lambda}_i\rangle$ and $\langle\dot{\phi}_i\rangle$ are the bounce averaged drift velocities across the field lines [59]. These drifts include the gradient-curvature drift, $E \times B$ drift velocity, and coroation electric fields. The inductive electric field, which results form a time-varying magnetic field, is accounted for implicitly as described by Fok et al. (2005) [54].

The first two terms on the right hand side of 2.13 account for the particle diffusion in energy and pitch angle due to interactions with plasma waves. The calculations for the phase space density are done in terms of (E, α_o) and the result mapped back to the (M, K) coordinate system. The last two terms on the right-hand side of equation 2.13 represent charge exchange loss for the ions and the losses due to precipitation in the loss cone. The boundary of the loss cone is a mirror location set at 100 km altitude. The charge-exchange cross section for a species s with neutral hydrogen is labeled by σ_{sH}. The term $\langle n_H\rangle$ is the density of hydrogen averaged over a bounce and τ_b is the particle bounce period. CIMI assumes that in the loss cone, particles have a lifetime of $.5\tau_b$ [60].

Equation 2.13 is an initial boundary problem. The ions have zero initial distribution or initial fluxes specified based on the empirical model of quiet time ring current by Sheldon and Hamilton 1993 [61]. The initial distribution for the electrons is given by the empirical model of AE8 [62, 63]. The pitch angle is assumed to be isotropic at the beginning of the simulation [60]. Particle flux at the inner boundary is set to zero, while the distribution at the outer boundary is determined by coupling with BATS-R-US as stated above. When solving the diffusion terms in Equation 2.13 CIMI assumes $\partial f/\partial E = 0$ at the lower energy limit, while it assumes f= 0 at the upper limit [60]. $\partial f/\partial \alpha_0 = 0$ is applied to both ends of the pitch angle grid [60].

$$\nabla \cdot (-\overleftrightarrow{\Sigma} \nabla \Phi) = J_{||} \sin(I) \tag{2.15}$$

CIMI uses the 2D thin-shell approximation in its conservation of the ionospheric currents. This simplification allows CIMI to make use of 2.15. $\overleftrightarrow{\Sigma}$ is the tensor representing ionospheric Hall and Pedersen conductance. Φ is the ionospheric potential, I is the magnetic dip angle, and $J_{||}$ is the is the Region 2 current, which is calculated from the pressure gradients of all ring current species [56]. Therefore, CIMI self-consistently solves the convection field, taking into account the electric coupling between the magnetosphere and the ionosphere. CIMI specifies the potential at the pole ward boundary at 70.3○ latitude by the Weimer

2K model and assumes that no current flows across the equator ward boundary. Equation 2.15 is used when CIMI is running either stand-alone or without a coupled ionosphere code [60]. For the purposes of this paper the ionosphere electrical conductance and resulting electric potential is handled by coupling to the Ridley Ionosphere Model discussed above. The discussion of how CIMI models the ionosphere is kept for the sake of completeness.

$$\frac{\partial N}{\partial t} + \langle \dot{\lambda}_i \rangle \frac{\partial N}{\partial \lambda_i} + \langle \dot{\phi}_i \rangle \frac{\partial N}{\partial \phi_i} = \frac{F_n + F_s}{B_i} \tag{2.16}$$

Equation 2.16 describes the embedded plasmasphere model of CIMI. F_n and F_s are the ionospheric fluxes in or out of the flux tube at the northern and southern ionospheres. B_i is the magnetic field at the ionospheric foot points of the flux tube. The net flux of plasmasphere material into our out of a flux tube depends on the balance between refilling, and diffusion. Refilling happens in flux tubes whose foot points are on the dayside of Earth, while diffusion occurs in flux tubes whose foot points are on the night side. As shown in the left-hand sides of equations 2.15 and 2.16, the plasmasphere particles drift in the same way as the energetic particles, the only difference being that the magnetic drift of cold plasma is ignored. CIMI imposes a saturation density at the model's inner boundary and a plasma trough density at the outer boundary. CIMI assumes that plasma density is constant along a field line. The simulated plasmasphere density is used to calculate the wave diffusion coefficients [60]. CIMI's plasmasphere is a modified Dynamic Global Core Plasma Model (DGCPM). We will discuss DGCPM, and the simulation of the plasmasphere, in more detail in the next section.

CIMI runs on an ionosphere grid with 30 minutes resolution in Magnetic Local Time (MLT) and a resolution of 76 in latitude, with the lower and upper boundaries on latitude described above. The time step in CIMI is typically 1 second though some functions, such as those that calculate wave diffusion, can decrease the time step to ensure dynamics are not skipped over. The initial condition for CIMI's embedded plasmasphere is to run the plasmasphere model for a day at initialization, giving it quite different initial condition then DGCPM, a matter which will be discussed in the Current Work Chapter.

In a new capability added to CIMI for this study, BATS passes density and pressure information to two populations in CIMI. Previously CIMI had only one population to represent plasma entering from the tail. We have added a second population representing the portion of the plasmasphere which has recirculated which contributes directly to ring current material. With this new capability, we can see exactly what portion of observables such as density, momentum, and pressure or D_{st} comes from the recirculating plasmasphere material.

2.5 Dynamic Global Core Plasma Model

The Dynamic Global Core Plasma Model (DGCPM) is a single-species two-dimensional plasmasphere model. The modeled value is the flux tube content in electrons per Weber. DGCPM models the most important processes of the plasmasphere, the filling, depleting, and transport due to electric fields.

If the magnetic field is $\vec{B}(\vec{r})$ and the electric field is $\vec{E}(\vec{r})$ in the equatorial magnetic plane, then the plasma continuity equation can be described by equation 2.17.

$$\frac{D_\perp N}{D_\perp t} = \frac{F_N + F_S}{B_i} \tag{2.17}$$

where $\frac{D_\perp}{D_\perp t}$ signifies a convective derivative and N is the flux tube content in electrons per Weber. F_N and F_S are the net fluxes of plasma in the northern and southern hemispheres, respectively, and B_i is the magnetic field strength at the ionospheric foot print of the field line, which the model assumes is the same at both foot points. This is true for a dipole magnetic field, however for a more realistic magnetic field, it may no longer by true. Depending on if the foot point is on the day side or the night side the flux tube will be either filling with plasma or losing plasma. On the day side the rate of gain is:

$$F_d = \frac{n_{sat} - n}{n_{sat}} F_{max} \tag{2.18}$$

where F_d is the rate at which flux is added, n_{sat} is the saturation density of the plasmasphere, n is the density, and F_{max} is the maximum rate of which flux can be added. This will lead to an exponential behaviour after we plug it into equation 2.21. The night side models exponential decay:

$$F_n = \frac{NB_i}{\tau} \tag{2.19}$$

where F_n is the flux on the night side, N is the density of the flux tube, and τ is the characteristic depletion time. Thus n_{sat}, F_{max}, and τ determine the behavior of the plasmasphere in the DGCPM model. In Ober et al. (1997) the values were, and still are: [64]

$$n_{sat} = 10^{A+B*L} cm^{-3} \tag{2.20}$$

where A = 3.904 and B = -.3145, an expression originated in the plasmasphere model of Carpenter and Anderson (1992) [64, 65]. The exponent describes the average equatorial electron density variation versus the McIlwain L value. The maximum flux in the Ober et al. (1997) paper is set to be $F_{max} = 2E10^{12} m^{-2} s^{-1}$. The decay time τ is set to 10 days. Equations 2.17 - 2.19 can be used to derive the following equations for the day time flux tube content,

$$N(t) = N_{sat} - (N_{sat} - N_0)e^{-\frac{t}{\tau_d}} \tag{2.21}$$

where,

$$\tau_d = \frac{N_{sat}B_I}{F_{max}} \tag{2.22}$$

and the following for night time decay,

$$N(t) = N_0 e^{-\frac{t}{\tau}} \tag{2.23}$$

where N_0 is the flux tube content at the start of the refilling or decay process, and t is the time since the start of the refilling or decay.

Plasma convection is handled by a second-order upwind scheme with a Superbee limiter [66]. While at the core, DGCPM is the same model as from Ober et al. 1997, it has undergone significant modification to be fully integrated in the SWMF [33, 64, 67]. For a more detailed discussion on how DGCPM functions, see Ober et al. 1997 [64].

Chapter 3

Configuration of the Models

3.1 Configuration of the SWMF

For the Chapter 4 the SWMF is configured to couple three models: the Block-Adaptive-Tree-Solarwind-Roe-Up-Wind-Scheme (BATS-R-US), the Dynamic Global Core Plasma Model (DGCPM) and the Ridley Ionosphere Model (RIM). BATS-R-US is a multi-fluid multi-species global magnetohydrodynamic (MHD) code [68]. In our case the simulation is configured with two fluids, both hydrogen. The first fluid is defined to be the known sources of the ring current, namely the solar wind and the high latitude ionospheric outflow [69, 70]. For the sake of simplicity we refer to the high latitude ionospheric outflow as the polar wind through out the rest of the report. The second BATS-R-US fluid represents the cold plasmasphere population and is coupled to DGCPM. For each fluid BATS-R-US solves the

DGCPM is a two dimensional plasmasphere code which solves for flux tube content on the ionosphere grid, projected into the equatorial plane [66]. DGCPM is configured within the Space Weather Modeling Framework to have one way coupling with BATS-R-US. Within 10 R_E of Earth BATS-R-US will nudge its solution for the mass density of the plasmasphere fluid towards that of DGCPM, such that the solutions converge rapidly [68, 71]. BATS-R-US is coupled to RIM in a two-way manner. BATS-R-US provides field aligned currents to RIM which in turn provides the $E \times B$ values at the inner boundary of BATS-R-US to set the velocity of all fluids there [72]. RIM and DGCPM are one-way coupled. DGCPM uses the solution of the electric potential generated by RIM to calculate the electric field in the equatorial plane [66]. For a graphical representation of this configuration refer to Figure 3.1.

Figure 3.1 summarizes the coupling of BATS-R-US, DGCPM and RIM through the framework of the SWMF. The red arrows in Figure 3.1 represent the coupling described above that was used in this study. The yellow arrow labeled 'Magnetic Field' pointing from BATS-R-US to DGCPM indicates a desired future coupling to be discussed later.

Several simplifying assumptions were made in the BATS-R-US simulation. The first assumption is that Earth's magnetic field can be represented as a dipole. The second assumption is that Earth's magnetic dipole is parallel to Earth's axis of rotation. The final assumption is that the axis of rotation is perpendicular to the ecliptic plane. DGCPM assumes a dipole with the same configuration, and thus by using a similar magnetic field configuration in BATS-R-US we minimize the effects of having non-coupled magnetic fields between the two models. The consequence of not having this coupling this will be discussed later.

The novel part of this configuration of the SWMF is that, on closed field lines within 10 R_E, the dynamics of the plasmasphere fluid in BATS-R-US are dictated by DGCPM. The DGCPM code has been shown to provide an accurate description of the plasmapause, as long as the ionospheric potential model is itself an accurate representation [73]. In this study we are using the SWMF to provide the ionospheric potential, via coupling to RIM, to drive DGCPM. This configuration has all of the advantages of the best preforming model to drive DGCPM as identified by Ridley et al. 2014 [73]. Therefore this configuration should provide the most accurate simulation of plasmaspheric dynamics to date.

Figure 3.2 shows a comparison of the plasmasphere in different configurations of BATS-R-US and DGCPM running as sub components of the SWMF. In Figure 3.2a we see the plasmasphere as produced by BATS-R-US running in a stand alone single fluid configuration. Figure 3.2b is BATS-R-US in a multi-fluid stand alone configuration with a dedicated plasmaspheric fluid. The difference between the configuration for 3.2a and 3.2b is that the inner boundary condition for the plasmaspheric fluid was increased from 28 amu/cc, a value typical of the polar wind, to 500 amu/cc. This inner boundary generates a much denser pseudo-plasmasphere. However, even with the configuration of 3.2b the plasmasphere and its plume is still very diffuse, lacking a sharply defined plasmapause. Figure 3.2c is a standalone DGCPM simulation, while Figure 3.2d is multi-fluid BATS-R-US coupled to DGCPM via the SWMF. As can be clearly seen in Figure 3.2a and Figure 3.2b a global MHD code, even with a dedicated plasmasphere fluid, is a poor representation of the dynamics that a cold dense plasma undergoes near Earth. The standalone DGCPM simulation gives a very detailed plasmasphere (though some features, such as the tendrils visible near midnight, may not be real), but standalone DGCPM lacks the ability to include the effects of the solar wind, plasma sheet and anything beyond 10 R_E from Earth. While this gives us a detailed view of the plasmasphere, it limits our understanding of the entire system. Thus by coupling DGCPM to BATS-R-US, we capture the best of both worlds. We are able to see and model the solar wind and the broader near-Earth space environment while maintaining a detailed view of the plasmasphere. Importantly, this enables us to study in a self-consistent manner how plasmaspheric material evolves once it leaves the inner magnetosphere, and whether it is captured by night side reconnection and advected back towards Earth.

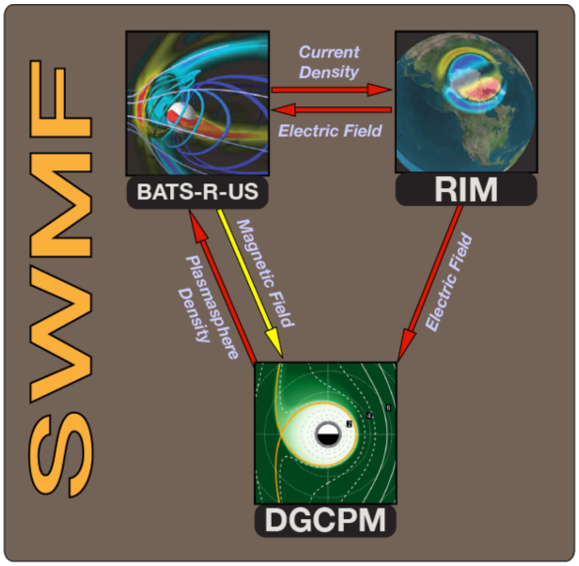

FIGURE 3.1: Configuration of the SWMF and coupling between sub modules. Red arrows depict coupling in the SWMF model which currently exists. The yellow arrow depicts coupling to be added to the future, to be discussed later.

3.2 Configuration of BATS-R-US

In the configuration for the following simulations BATS-R-US is configured with two fluids, both of which are hydrogen. The first fluid is the combined solar wind and polar wind, while the second is a dedicated plasmasphere fluid. BATS-R-US handles the bulk of the computational space while the other models, DGCPM and RIM, handle specific components of the inner magnetosphere and ionosphere. BATS-R-US runs on a Cartesian grid in the GSM coordinate system. A key feature

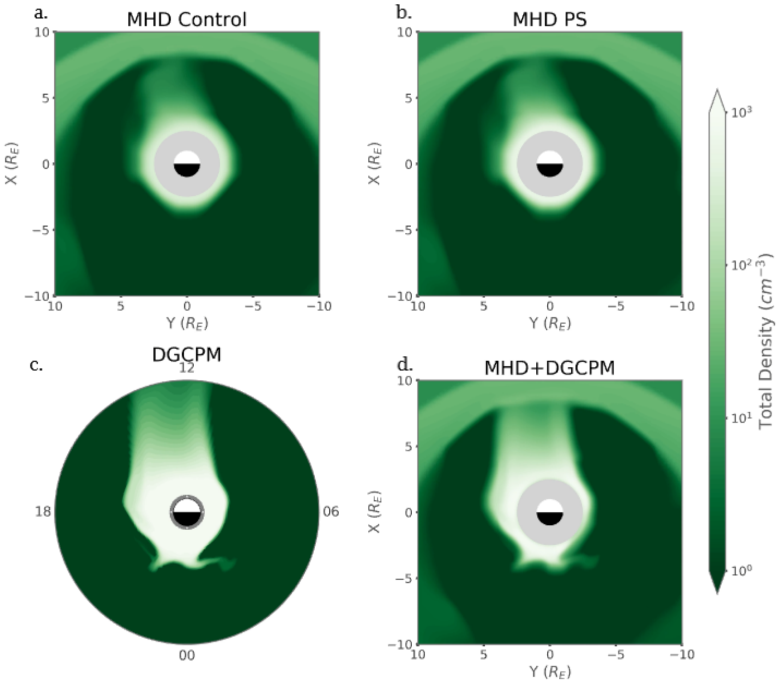

FIGURE 3.2: Coupling of BATS-R-US and DGCPM. (A) Z=0 slice of single fluid BATS-R-US in standalone mode. GSE coordinates.(B) Z=0 slice of two fluid BATS-R-US in standalone mode. GSE coordinates. (C) Standalone DGCPM out to 10 R_E. LT and Radius (D) Z=0 SWMF coupling dual fluid BATS-R-US and DGCPM. GSE coordinates.

of BATS-R-US is the flexible grid size of cells within the region of computation. In the configuration used in this study, the entire inner magnetosphere was resolved to a resolution of 1/8 Earth Radii (R_E). The maximum grid size was cubes of 8 R_E a side, while the minimum was cubes of 1/16 R_E a side. The grid is set with areas of high resolution near the magnetosheath and Earth starting at 1/16 R_E cells and stepping down from there. Farther down the tail, the grid is dominated by cells of 8 R_E. For a more detailed discussion of the grid see Welling and Liemohn 2014 [74].

Within BATS-R-US, the upstream boundary condition is determined by solar wind and interplanetary magnetic field (IMF) values read from a file. Upstream plasma values must be provided for every fluid in the MHD simulation. This restriction is discussed in the subsection about BATS-R-US within the Models Chapter. The inner boundary is determined by predefined values made to mimic the polar wind. In BATS-R-US, the inner boundary values for the combined solar and polar wind fluid were set to 28 amu/cc at 25000.0 K. For the plasmasphere fluid, values of .01 amu/cc and 25000 K were assigned. The low amu/cc count of the plasmasphere prevents the inner boundary condition from becoming a significant source of plasmasphere ions.

3.3 Configuration of DGCPM

The temperature of the plasma is fixed to be 1 eV for the purpose of coupling to BATS-R-US. This value is consistent with values given in the literature which range from .01 eV - 2 eV [75, 76]. This temperature along with the density of the plasma in DGCPM is used to calculate the pressure of the plasmasphere in

BATS-R-US. This pressure is always a small fraction ($\leq 10\%$) of the total pressure of non-plasmaspheric fluid in BATS-R-US and does not significantly affect the MHD calculation. Therefore, the calculation is fairly insensitive to the choice made for the temperature of the plasmaspheric plasma. DGCPM assumes a dipole field and does not receive non-dipole values from BATS-R-US. BATS-R-US self-consistently calculates the magnetic field, though it also assumes a dipole for Earth's magnetic field. The possible consequences of this discrepancy will be discussed in a later chapter.

The initial condition of DGCPM for these runs is one of a dense plasmasphere at or near the saturation density. This initial condition is chosen specifically to give us the best chance at seeing recirculation occur. It is important to keep this in mind when we discuss the results as this may bias us to see recirculation as more of a dominant source relative to the solar and polar winds. However, as the fullness of the plasmasphere does not affect the likelihood of a geomagnetic storm occurring these results represent the recirculation of the plasmasphere when it is at or near saturation.

3.4 Configuration of RIM

The currents from BATS-R-US are taken at a fixed altitude near the inner boundary. The current values are then mapped along dipole field lines to the ionosphere. The gradient of the potential yields the electric field which can be combined with BATS-R-US's magnetic field to yield the $E \times B$ value, which is returned to BATS-R-US. In BATS-R-US, the returned $E \times B$ values are used to set the tangential velocity of the plasma about the inner boundary. A major challenge for ionosphere models is getting the realistic conductance. Conductance is primarily derived from two sources: ionization due to extreme ultra-violet (EUV) radiation [48] and ionization due to precipitating ions and electrons [77–79]. Conductance caused by extreme ultra-violet radiation is included via an empirical formula, which is a function of solar zenith angle [72]. RIM uses an empirical model based on an Assimilate Mapping of Ionospheric Electrodynamics (AMIE) study to drive the conductance caused by particle precipitation [80]. The Assimilate Mapping of Ionospheric Electrodynamics study produced a simple relationship for the strength of field aligned currents and Hall or Pedersen conductance:

$$\Sigma = \Sigma_0 e^{-A|J_{||}|} \tag{3.1}$$

where Σ_0 and A are functions of latitude and longitude. Two sets of coefficients are used, one for upward, and one for downward field aligned currents. For a detailed discussion of how the model works see [45].

RIM is also coupled to DGCPM. In the one way coupling between DGCPM and RIM, DGCPM requests electric field data from RIM. RIM can calculate the electric potential down to the low latitudes and thus provide the electric field to the entire DGCPM domain.

Chapter 4

Published Simulations

4.1 Ideal Square Wave

The first simulation presented for this study is an Ideal Square Wave event. The solar wind has a constant density and velocity of 5 /cm^{-3} and 450 km/s. The B_z component of the interplanetary magnetic field (IMF) begins at +5 nT flipping to -10 nT after 8 hours, marking the start of the storm. There is a constant value of B_y = +2 nT which moves the reconnection line slightly out of the equatorial plane. The B_x component of the solar wind is zero throughout the simulation. Such ideal event conditions are chosen to demonstrate that the recirculation of plasmaspheric plasma is possible. The long period of quiet time preceding the start of the storm allows the simulation to build a dense and saturated plasmasphere. The sudden southward turning and constant negative B_z provides the maximum amount of time for plasmaspheric material to recirculate. Having an extended southward B_z period increases the chances that we see such an affect occur. In addition, the constant negative B_z drives reconnection on the dayside, which in turn drives the formation of the dayside plasma plume. Relatively typical solar wind velocity and density were chosen to demonstrate that our results are not a consequence of rare or unusual solar wind conditions.

Figure 4.1A-F shows the state of the plasmasphere in BATS-R-US at three key points in the simulation. Figure 4.1A-C shows 2D slices from the Y=0 plane, while Figure 4.1D-F shows 2D slices of the Z=0 plane. The black and white circle at the origin of each plot represents the Earth. The white half of the circle represents the dayside and the black half the night side of Earth. The light gray circle around the Earth represents the inner boundary of BATS-R-US. The color map of each plot is the density of the plasmaspheric fluid in BATS-R-US at that point in the domain. The yellow arrows represent the magnitude and direction of the velocity vector field for the plasmaspheric fluid. The velocity arrows in the upstream solar wind of each plot are 450 km/s. In subplots A-C in Figure 4.1, the black contours are closed magnetic field lines, meaning both foot points of the field line are in the ionosphere. The red contour represents the last closed magnetic field line, whereas the white contours represent open field lines. Each column contains slices from a single time in the simulation. The times chosen are 08 Hr 40 Min, 09 Hr 19 Min, and 09 Hr

52 Min, for the left, center, and right columns respectively. Recall that the storm began with a southward turning of B_z at 8 Hrs. Thus, the times shown in Figure 4.1 are from 40 Min, 1 Hr 19 Min, and 1 Hr 52 Min after the storm began respectively. These times show three key moments of plasmasphere recirculation. In Figure 4.1D, the dayside plume encounters the dayside reconnection line and begins venting plasmaspheric plasma along the dawn flank. This feature is highlighted by the red box in Figure 4.1D. We see in Figure 4.1A that the dayside lobes do not contain much plasmaspheric material. There is a strong divergence in the flow pattern on the night side in Figure 4.1B corresponding to the location of night side reconnection, marked by a red box. We also see that the lobes are beginning to fill, indicating that at this time, plasmaspheric material has not recirculated over the poles. In Figure 4.1E, we see a good deal of plasma has continued to leak out of the dayside plume and has begun to fill the plasma sheet with recirculated material. This process is aided by the flank biased plume which, when comparing to Figures 4.1C and 4.1F, is venting much more material along the flanks then though the dayside lobes. In Figure 4.1C, we see that the lobes have become saturated with plasmaspheric material, while in Figure 4.1F, we see that the amount of material vented along the flanks is greatly reduced. This reduction in material recirculating around the flank can be seen comparing the density within the red boxes marked on plots 4.1E and 4.1F.

Figure 4.1G-L shows the relative contribution of the plasmasphere fluid to the total fluid density in BATS-R-US. Figure 4.1G-I contains Y=0 slices while Figure 4.1J-L contains Z=0 slices. We see from the progression of Figure 4.1G to Figure 4.1I that the filling of the dayside lobes with recirculating plasmasphere material takes a significant amount of time. By the time plasmasphere fluid is a significant fraction of the total population in the lobes, we see that the recirculating plasmasphere is already a significant contributor to the population of the plasma sheet (Figure 4.5B). In agreement with conclusions drawn from Figure 4.1A-F we see that the around-the-flank recirculation is must faster then over the pole recirculation. By comparing the timing of the lobes becoming dominated by the recirculated plasmasphere to Figure 4.5 we see that the peak of the relative contribution of the plasmasphere fluid to the total fluence from the plasma sheet into the inner magnetosphere comes during a time when through-the-lobe recirculation is dominant.

Consider the progression shown in all three time slices. We see that early in the storm, material leaks out of the plasmasphere primarily through the dawn flank, not over the lobes. While some plasmasphere material does recirculate through the dusk flank, it is a small amount compared to the recirculation through the dawn flank. This disparity is primarily due to the location of the plasmaspheric bulge being near the dawn flank when the storm began. We see that recirculation along the flanks is relatively fast compared to recirculation over the lobes as the tail begins to fill with plasmaspheric fluid from the flanks before the lobes fill with plasmaspheric material. As the storm progresses, however, we see that plasmaspheric plasma recirculating along the flanks diminishes as as the dayside plume moves towards the center of the reconnection line away from the flank. At the same time, the lobes are now full and providing most of the recirculating plasma. Thus, the path that recirculating plasma takes is dependent on the location of the dayside plume and how much time has passed since the storm began. To see an animated movie of Figure 4.1A-F for the Ideal Square Wave simulation see the supplementary materials presented at the end of this paper.

The times, 08 Hr 40 Min, 09 Hr 19 Min, and 09 Hr 52 Min, are also marked on Figures 4.5-4.6 to aid in making comparisons between plot features. These markings will be labeled ’A.)’, ’B.)’, and ’C.)’, corresponding to the columns of Figure 4.1. In addition to these marked times, the simulation start at 08 Hr 00 Min is also marked, though it is unlabeled.

Figure 4.3A-F depicts the temperature of combined solar wind and polar wind fluid. In Figure 4.3G-L we see the temperature of the plasmasphere fluid. The left, center, and right columns are at the same time as those in Figure 4.1. The major take away from the plot is the degree to which the plasmasphere is heated during the process of recirculation. Over the entire course of leaving through the dayside plume and recirculating, plasmaspheric material is shown to heat several hundred to several thousand electron volts by the time it reenters the inner magnetosphere. This heating occurs due to several mechanisms. At the day side magnetopause pick up ion heating occurs. The plasmasphere material cools as it travels over the poles and heats again in the tail, mostly through conservation of the adiabatic invariants. Welling and Ridley 2010 [81] discusses this process. For a discussion of heating at the reconnection line Toledo-Redondo et al. 2016 [82] and references therein discuss this.

Figure 4.4 depicts the absolute difference between the temperature of the plasmasphere fluid and the combined solar and polar wind fluid in BATS-R-US. Figure 4.4A-C shows Y=0 slices while 4.4D-F shows Z=0 slices. Again the left, center, and right columns correspond to 8 hours 40 minutes, 9 hours and 19 minutes and 9 hours and 52 minutes after the simulation again. At all times we see a significant difference between the temperature of the plasmasphere and combined solar and polar wind. This large temperature difference occurs even in regions where the recirculating plasmaspheric plasma has been extremely heated. This difference in temperatures is crucial as it should be detectable by satellite missions such as THEMIS and CLUSTER. This feature indicates that a signature of recirculating plasma could be detected as a secondary population of plasma in the tail whose temperature is several keV below the majority of the detected plasma. The fact that this signature does not rely on tracer species, such as helium or oxygen, greatly

Variable	Day Side	Night Side
Radius	6.6 R_E	10 R_E
Latitude	± 30°	± 60°
Longitude	± 90°	± 90°

TABLE 4.1: Limits of the surface of measurement through which fluence is calculated.

expands the number of candidate events that can be studied in the future.

The next value which we will look at is fluence, being the integration of flux over a surface. On the dayside of the planet, the surface of integration was a hemispherical shell going from dawn to dusk and spanning ±60° latitude at 6.6 R_E, geosynchronous orbit. The boundaries of the integration surfaces are recorded in Table 4.1. Fluence is calculated through the surface of the shell as a discrete sum of the flux over the area, where $flux_r$ is the radial flux. r is the radius fixed to 6.6 R_E on the dayside. θ is the latitude and ϕ is the longitude. $d\theta$ and $d\phi$ are the discrete step in theta and phi with values of $\pi/90$ radians due to the resolution of data points on the spherical shell. The flux is calculated from the density and bulk flow velocities of the fluids taken from BATS-R-US. On the night side, the boundary through which we measure flux and calculate fluence is a spherical shell of 10 R_E going from dawn to dusk and ±30° latitude. This radial distance was chosen due to the coupling between BATS-R-US and DGCPM which occurs at and within 10 R_E. This limitation raises an issue which we will discuss later. The choice of

6.6 R_E on the dayside is somewhat arbitrary. The dayside surface was chosen to be at that distance because in both simulations the surface was never in the solar wind. Geosynchronous orbit is also were many satellites with plasma detecting instruments sit. Therefore, in the future, geosynchronous orbit is a likely place to look for signatures of plasmaspheric recirculation. Having such data now will allow us to compare directly between this current study and possible future work. On the night side, we are interested only in the fluence of the BATS-R-US fluids towards Earth. Therefore, the calculation of fluence on the night side censors flux which is pointing away from Earth. The case is reversed on the day side, where the flux pointing towards Earth is censored in the fluence calculation. The intersection of these 3D surfaces with the Y=0 and Z=0 planes is marked on Figure 4.1G-I as black dashed arc segments.

$$fluence(\frac{\#}{s}) = \Sigma flux_r r^2 \cos(\theta) d\theta d\phi \tag{4.1}$$

Figure 4.5A shows the fluence of the fluids in BATS-R-US as they pass the measurement boundaries 4.1. The x-axis of Figure 4.5 is simulation time. We do not show the first six hours after the simulation began, as the early part of the simulation is simply to build a steady state in the inner magnetosphere. The y-axis of Figure 4.5A shows the fluence of the fluids in BATS-R-US as they pass through the measurement surfaces 4.1. The vertical line marked 'Ω.)' corresponds to the start of the storm. The vertical lines marked 'A.)', 'B.)', 'C.)' correspond to the times: 08 Hr 40 Min, 09 Hr 19 Min, and 09 Hr 52 Min. These times correspond to the left, center, and right columns of Figures 4.1-4.4. In Figure 4.5A the bright green curve indicates the flow of plasmaspheric material through the dayside measurement surface, while the remaining three curves show the flow of material through the night side measurement surface. The dark green curve represents the fluence of plasmaspheric material on the night side, and thus, represents the recirculated plasmaspheric plasma. The dark blue curve shows the fluence of the combined solar and polar wind through the night side measurement surface. The dark red curve shows the total fluence of both BATS-R-US fluids through the night side measurement surface. Figure 4.5A shows that plasmaspheric material flows strongly out the dayside boundary, indicating a strong plume flow. This finding agrees well with observations made in the Z=0 slices of Figure 4.1. The value is comparable to ionospheric outflow once the storm begins. By comparing the magnitude of the fluence of plasmaspheric material leaving the plasmasphere on the dayside to the fluence of the plasmaspheric materials crossing the night side boundary, we see that we lose an order of magnitude of material during the process of recirculation. Thus, we can state that most of the material is lost to the solar wind, which agrees well with Moore et al. (2008) [31]. Maximum fluence of the recirculated plasmaspheric material through the night side boundary occurs around 9 Hr 37 Min. Looking back to Figure 4.1, we see that this is in between the majority of recirculation traveling through the flanks at 09 Hr 19 Min, or the lobes at 09 Hrs 52 Min. As might be expected, maximum recirculation occurs when the plasma has the most paths through which to travel. Note that from approximately 09 Hrs 45 Min to 10 Hr 30 Min, the dayside plasmaspheric fluence out the plume remains fairly constant. However, at the same time, the fluence of plasmaspheric material on the night side decreases. As we know, by comparison to Figure 4.1, that this time indicates a shift from mostly around the flank recirculation to mostly over-the-pole recirculation. Therefore, the fall off in plasmaspheric fluence on the night side indicates that recirculation through the flank is a more efficient path then over-the-pole recirculation. The spike in the solar and polar wind fluid crossing the night side boundary is explained by a build up of cold plasma on the night side due to flow patterns during quiet time. As the storm begins, the magnetosphere is disturbed injecting a large portion of this build up towards Earth as the magnetosphere collapses. After this initial spike, we see that the amount of combined solar and polar wind crossing the night side boundary is comparable to that of the plasmaspheric material which has recirculated. For a more detailed comparison of the fluid crossing the night side boundary, we look to the bottom frame of Figure 4.5B.

Figure 4.5B shows what percentage of the material crossing the night side boundary was provided by the recirculated plasmasphere material. The y-axis is the percentage of the total fluence which is provided by the recirculated plasmasphere. At 0% there is no plasmasphere recirculation, at 50% the recirculated plasmasphere contributes equally with the other fluid, which is the combined solar and polar winds. Once the dayside plume has vented a substantial amount of material, we see that the recaptured portion is still more then 10% of the total plasma content crossing the night side for three and a half hours. The maximum contribution of the recirculated material was 25%, with contributions over 20% lasting about an hour. Unsurprisingly, by comparison with Figure 4.1, we see that the maximum relative contribution occurs during the time when both flank and over-the-pole recirculated plasma was contributing to the total fluence on the night side. Refer to Figure 8 of Welling et al. 2018 [83] which shows the results of an experiment done where O^+ was injected into the inner magnetosphere in windows centered around dawn, midnight, and dusk. As the plot there demonstrates, the more dawnward material is injected into the ring current, the more likely it is to remain on a closed drift path and contribute to the ring current. This fact raises a point which we will discuss later.

A consequence of Figure 8 in Welling et al. (2011) [83] is that in addition to considering the absolute contribution of the fluids in BATS-R-US to the plasma sheet, we must also consider where those contributions were made in space. Figure

4.6 shows what percentage of the total fluence crossing the night side measurement surface was provided by the recirculating plasmaspheric plasma, broken down by magnetic local time 4.1. The y-axis is simulation time, with the earlier parts of the simulations being at the top of the plot. The x-axis is magnetic local time going from dusk through midnight to dawn. The color map is scaled so that 0% recirculated plasmaspheric plasma corresponds to the darkest blue. At 100%, which would represent only recirculated plasmaspheric material crossing the night side boundary, the color map is the darkest green. The white color indicates 50% where recirculated plasmaspheric fluid and the combined solar and polar wind fluid are contributing equally. What we see here is that, relative to the combined solar wind and polar wind fluid, most of the contribution of the recirculated plasmaspheric material is centered in a window spanning midnight to 2 a.m. local time. The recirculated plasmaspheric plasma goes from being mostly provided by the dawn side flank, to being provided by the over-the-pole recirculation. At the same time, we see the majority contribution of the plasmaspheric plasma flow shift duskward. The duskward shift of the plasmasphere material crossing the night side boundary also corresponds with the dayside plume continuing to sweep from dawn to dusk. The recirculated plasmaspheric plasma has a local maximum contribution of 70% the total fluence across the boundary in a window spanning midnight to 2 a.m. local time.

4.2 Time-Epoch Averaged Corotating Interaction Region Event

The second event studied for this paper is an Idealized Corotating Interaction Region (CIR) Event. The event was constructed by taking a time averaged epoch analysis of 11 storms during solar cycle 23 [84]. For a more detailed discussion of exactly how the anaylysis was preformed see Katus et al. 2015. Figure 4.7 shows a detailed plot of the IMF conditions used for this simulation. All four panes of Figure 4.8 share an x-axis with the major ticks being periods of 24 hours. In Figure 4.7, the top panel shows the B_y and B_z components of the IMF. The y-axis here is the displacement from quiet time averages of the IMF measured in nanotesla (nT). The storm occurs in two phases. The first phase of the storm starts after 6 hours and begins as a sharp southward turning in the B_z component of the IMF of about 7.5 nT. After remaining steady for about four hours, there is a second southward turning in the B_z component of roughly another 7.5 nT where it remains for approximately four hours before beginning to recover. The idealized CIR storm has a long recovery period of 65 hours [84]. As this study is only interested in the main phase of the storm, the first 30 hours of the ideal CIR storm was simulated. The density of the solar wind, Figure 4.7B , increases from an average of 12.5 $/\text{cm}^{-3}$ up to 22. 5 $/\text{cm}^{-3}$ before recovering to 12.5 $/\text{cm}^{-3}$ at the end of the storm. Figure

4.7C shows the velocity of the solar wind measured in km/s along the y-axis. The velocity of the solar wind began slower then that of the other simulation at 350 km/s, however, the velocity increased throughout the simulation ending at 525 km/s.

Figure 4.8 reports the state of the plasmasphere in BATS-R-US for the Idealized CIR storm at 11 hours. This time corresponds to the period of maximum relative contribution of the recirculated plasmasphere to the total fluence through the night side measurement boundary (Figure 4.9B). Figure 4.8A shows a 2D slice from the Y=0 plane, while Figure 4.8C shows a 2D slice of the equatorial plane. The color map of Figures 11A and 11C is the density of the plasmaspheric fluid in BATS-R-US. The yellow arrows represent the magnitude and direction of the velocity vector field for the plasmaspheric fluid. The velocity arrows in the upstream solar wind of each plot are 450 km/s. In Figure 4.8A, the black contours are closed magnetic field lines (i.e. both foot points in the ionosphere), and the red contour represents the last closed magnetic field line, whereas the white contours represent open field lines. Similar to the plot shown for the Ideal Square Wave event 4.1, we see that the majority of the plasmaspheric material is flowing over the poles after the initial phase of the storm. There is virtually no flow of plasmaspheric plasma around the flank by this time. This lack of flow is in part due to the location of the dayside plume. Unlike in the Ideal Square Wave event, there were initially two plumes. The smaller of the plumes was present from early in the simulation venting plasmaspheric material along the dusk flank. The main plume formed as a result of the changing IMF conditions, and first impacted the dayside reconnection line around 7:00 Simulation Time. The central plume remained much broader and denser then the dusk side plume contributing the majority of the fluence on the dayside. The third dawn side plume formed as features from the night side plasmasphere co-rotating around Earth became stretched out on the dawn flank as a consequence of dayside reconnection. Again, we see that plasmaspheric materials flows along the flanks well before there is significant flow over the poles into the lobes. However, unlike in the Ideal Square Wave Event, we see that the peak contribution from the plasmasphere comes from a time dominated by over-the-pole flow. Interestingly, despite the dusk side plume venting material into the tail from early in the storm, there is a slight dawnward bias in the MLT where the plasmaspheric material flows down the tail towards Earth. This dawnward bias is clearly seen in Figure 4.8D. To see an animated movie of Figure 4.8A and 4.8C for the entire storm, see the supplemental materials. Figure 4.8B and 4.8D shows the relative contribution of the plasmasphere density to the total fluid density in the Y=0 and Z=0 planes. Similar to what we see in Figure 4.1G-L, by the time we reach peak relative contribution of the recirculating plasmasphere to the total density we see that the lobes are dominated by plasmasphere material. In addition, we also see that over-the-pole recirculation dominates over around-the-flank recirculation at this stage of the storm.

Figure 4.9 shows the fluence of the fluids in BATS-R-US as they pass the measurement boundaries 4.1. The dashed bright green curve of Figure 4.9 is the fluence of the dayside plume, the dark red curve is the total fluence across the night side boundary, the dark green curve is the fluence of the recirculating plasmasphere on the night side, while the dark blue curve is the fluence of the combined solar and polar wind on the night side. The fluence of the dayside plume occurred in two major phases. The first phase coincided with the onset of the storm beginning around 6:00 UT. The second phase began around 14:00 UT, which coincides with the occurrence of several sub-storms in the tail. As can be seen in the animated movie included in the supplementary material the relaxing of the magnetic fields after the sub-storms causes a large injection of material into the inner magnetosphere from the tail. As can also be seen by comparing Figure 4.9 to the animated movie of the Idealized CIR storm, as the storm progress the reconnection line on the night side moves in towards the planet. The movement of the reconnection line causes recirculating plasmasphere material to enter the tail, rather then being injected back into the inner magnetosphere. The shifting nightside reconnection line explains the lack of an increase in the recirculating plasmasphere on the night side following the period of increased fluence out the dayside seen from 14:00 UT to 20:00 UT.

Figure 4.9 shows the percentage of the total fluence crossing the night side boundary which is provided by the recirculating plasmaspheric plasma. The y-axis for Figure 4.9 is the percent relative contribution of the plasmasphere fluid. At 0% there is no recirculating plasmaspheric plasma. At 50%, the recirculating plasmaspheric plasma and combined solar and polar winds contribute equally to the fluence across the night side boundary. We note that the recirculated plasmaspheric material began to become a noticeable fraction of the whole much faster than in the Ideal Square Wave event. The relatively early increase in the importance of the recirculated plasmaspheric contribution is explained by the plasmaspheric material leaking out of the plasmasphere through the dusk side plume and into the tail through the flanks. The relative contribution is much higher than in the previous event with a maximum contribution of up to 43%. For a period of four hours, starting from 09:00 UT, over 20% over the total material contributing to the plasma sheet is recirculated plasmaspheric material.

Figure 4.10 shows what percentage of the total fluence crossing the night side measurement surface was provided by the recirculating plasmaspheric plasma, broken down by magnetic local time for the Idealized CIR event4.1. The y-axis is simulation time, with the earlier parts of the simulations being at the top of the plot. The x-axis is magnetic local time going from dusk through midnight to dawn. The color map is scaled so that 0% recirculated plasmaspheric plasma corresponds to the darkest blue. At 100%, which would represent only recirculated plasmaspheric material crossing the night side boundary, the color map is the darkest green. The white color indicates 50% where recirculated plasmaspheric fluid and the combined solar and polar wind fluid are contributing equally. Unlike for Figure 4.6 a filter is applied to the calculated relative contribution. This filter takes the form of a minimum required fluence. If the total fluence in a given cell is below 4E7 particles per second then the value is censored and set to 0% for the purposes of the color bar scale. When the total fluence is low the recirculating plasmasphere can become a significant portion of the total fluence in a cell, even dominating it. This lack of fluence causes random spikes of high contribution of the recirculating plasmasphere to appear at all over the plot. Therefore, the minimum fluence requirement is imposed to not give a false sense of importance to the recirculating plasmasphere. Despite the censorship, we see several similarities to Figure 4.6. The most important similarity is that the majority of the plasmasphere recirculation comes in a window centered around midnight. This fact is true even in the earlier part of the storm where the recirculation was primarily happening through the dusk flank. Though unlike in Figure 4.6 we see a duskward, rather then dawnward bias.

Figure 4.11 shows the pressure of the fluids in BATS-R-US at the point when recirculating plasmasphere material was at it highest peak. The left column depicts the pressure of the plasmasphere fluid, while the right column depicts the combined solar and polar wind. The top row of Figure 4.11 contains a Y=0 slice, while the bottom row contains a Z=0 slice. Figure 4.11 and 4.11 shows that in the equatorial plane the combined solar and polar wind fluid has a much higher pressure then the plasmasphere fluid. The most significant source of pressure for the plasmasphere, outside the plasmasphere itself, is a beam of plasma in the night side equatorial tail centered around midnight. This region of relatively high pressure corresponds, by comparison to Figure 4.8, to a fast, but not dense, flow of recirculating plasma in the tail.

Figure 4.12 shows how the temperature of the fluids in BATS-R-US evolve as a function of location within the environment. The image was generated from a single time corresponding to the storm maximum in the Idealized CIR event simulation. The right column shows 2D slices of the Z=0 plane, while the left hand column shows 2D slices from the Y=0 plane. The top row of Figure 4.12 shows the absolute temperature difference between the combined solar and polar wind fluid, and the plasmaspheric fluid measured in electron volts (eV). The central row depicts the temperature of the combined solar and polar wind fluid, while the bottom row depicts the temperature of the plasmaspheric fluid, both reported in electron volts (eV). In strong agreement with Figures 4.3 and 4.4 we see that the plasmasphere fluid is heated to several keV in regions outside the plasmasphere. We see that the temperature difference between the combined solar and polar wind and the plasmasphere is on the scale of several keV in regions such as the tail. This finding reinforces the results of Figure 4.4, demonstrating that the recirculated plasmasphere could be detached independent of the solar or polar winds, with out the need of a tracer species.

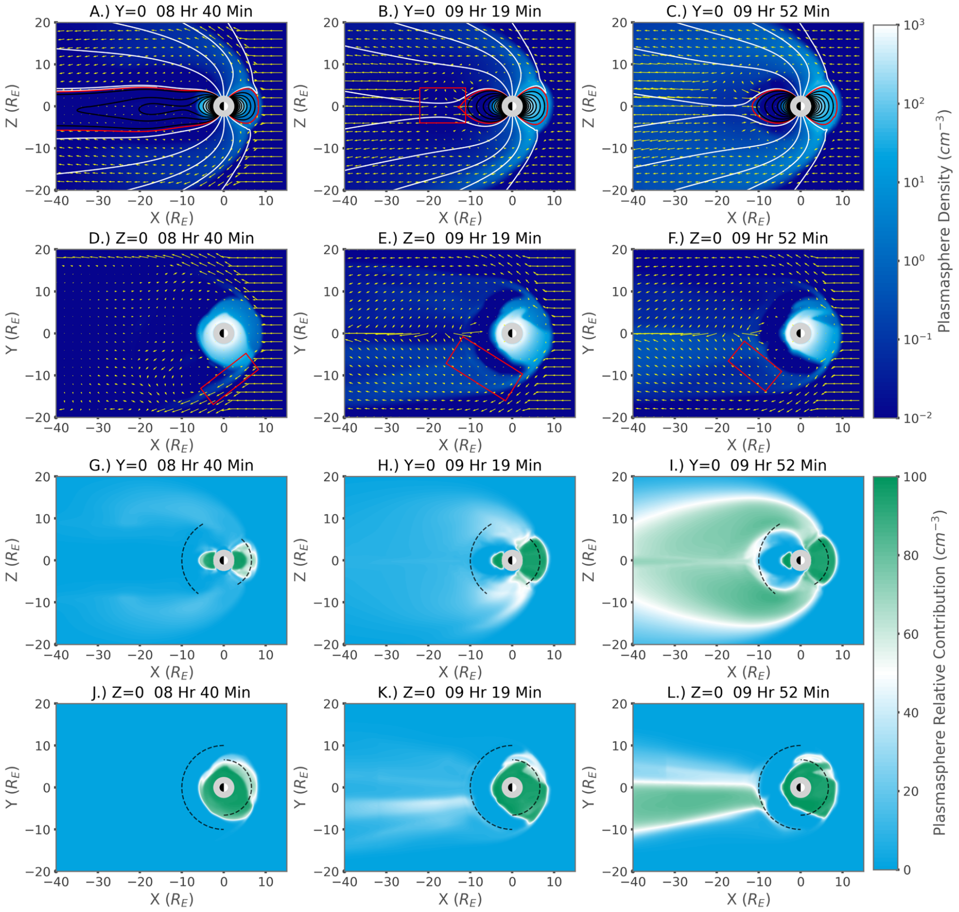

FIGURE 4.1: From the BATS-R-US simulation of the Ideal Square Wave Event. Column (A): 8 Hr and 40 Min into the simulation. Column (B): 9 Hr 19 Min into the simulation. Column (C): 9 Hr 52 Min into the simulation. (A)-(F) State of the Plasmasphere at during the Ideal Square Wave Event. The color map corresponds to the density of the plasmasphere fluid in BATS-R-US, while the yellow vector field represents the velocity of the same fluid. (A)-(C) Y=0 slices additionally showing the magnetic field configuration. White curves are open magnetic field lines, red is the last closed field line, while black curves represent the closed magnetic field. (D)-(F) Z=0 slices. (G)-(L) Relative contribution of the plasmasphere fluid to the total fluid density. A contribution of 0% (blue) means that there is no plasmasphere fluid contribution to the total density. A contribution of 50% (white) means that the combined solar and polar wind fluid contributes to the total density equally with the plasmasphere fluid. A contribution of 100% (green) means that there is no contribution to the total density from the combined solar and polar wind. The black dashed circular arcs mark the where the surface of measurement crosses through the Y=0 and Z=0 planes 4.1. (G)-(I) Y=0 slices, (J)-(L) Z=0 slices.

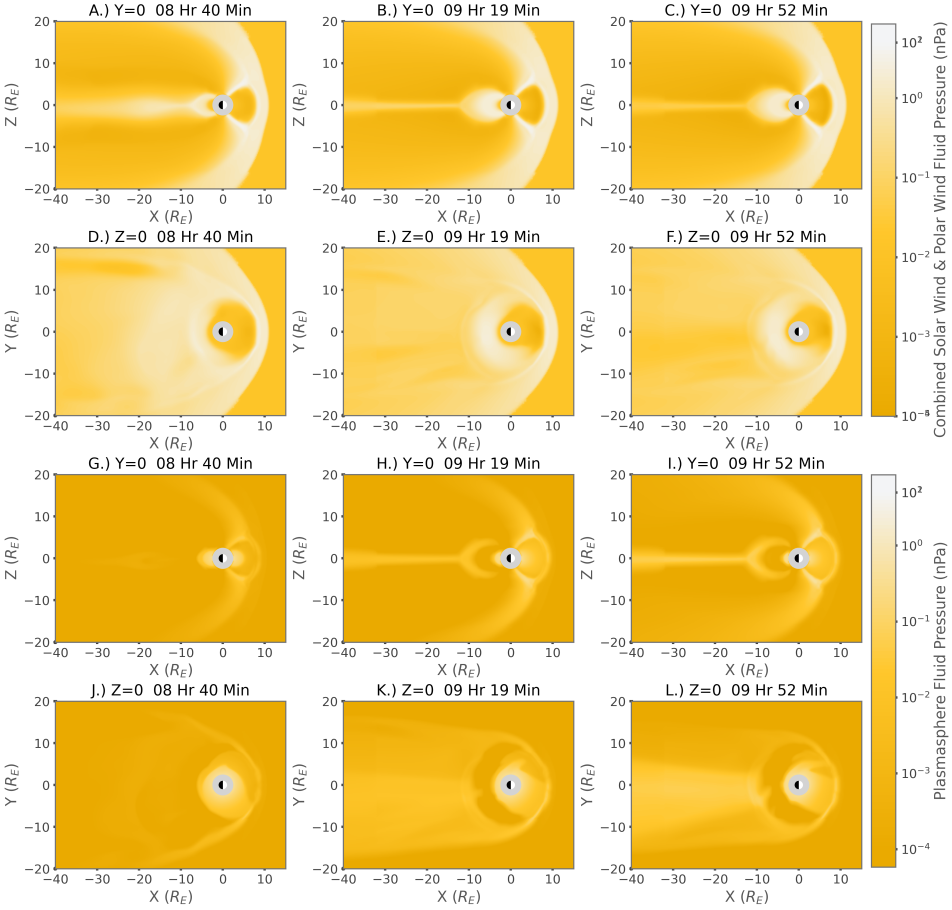

FIGURE 4.2: Pressure of Fluids in BATS-R-US for the Ideal Square Wave event. Column (A): 8 Hr and 40 Min into the simulation. Column (B): 9 Hr 19 Min into the simulation. Column (C): 9 Hr 52 Min into the simulation. (A) - (F) Pressure of the combined solar wind and ploar wind fluid. (A) - (C) Y=0 slices, (D) - (F) Z=0 slices. (G) - (L) Pressure of the plasmasphere fluid. (G) - (I) Y=0 slices, (J) - (L) Z=0 slices.

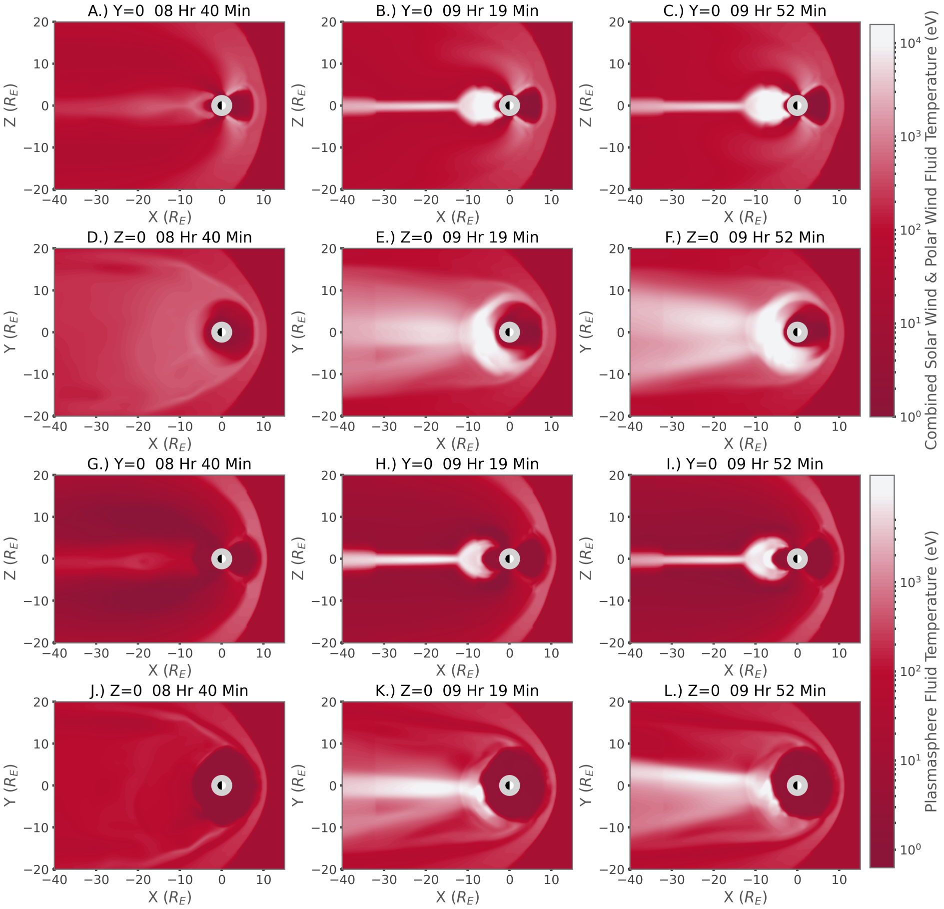

FIGURE 4.3: Temperature of Fluids in BATS-R-US for the Ideal Square Wave event. Column (A): 8 Hr and 40 Min into the simulation. Column (B): 9 Hr 19 Min into the simulation. Column (C): 9 Hr 52 Min into the simulation. (A) - (F) Temperature of the combined solar wind and ploar wind fluid. (A) - (C) Y=0 slices, (D) - (F) Z=0 slices. (G) - (L) Temperature of the plasmasphere fluid. (G) - (I) Y=0 slices, (J) - (L) Z=0 slices.

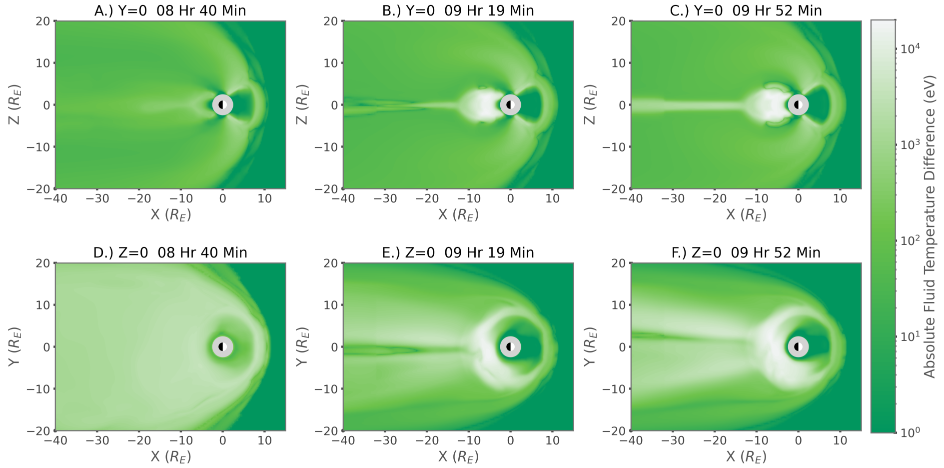

FIGURE 4.4: Absolute temperature difference of the plasmasphere fluid and combined solar and polar wind fluid in the BATS-R-US simulation for the Ideal Square Wave event. Column (A): 8 Hr and 40 Min into the simulation. Column (B): 9 Hr 19 Min into the simulation. Column (C): 9 Hr 52 Min into the simulation. (A) - (C) Y=0 slices, (D) - (F) Z=0 slices.

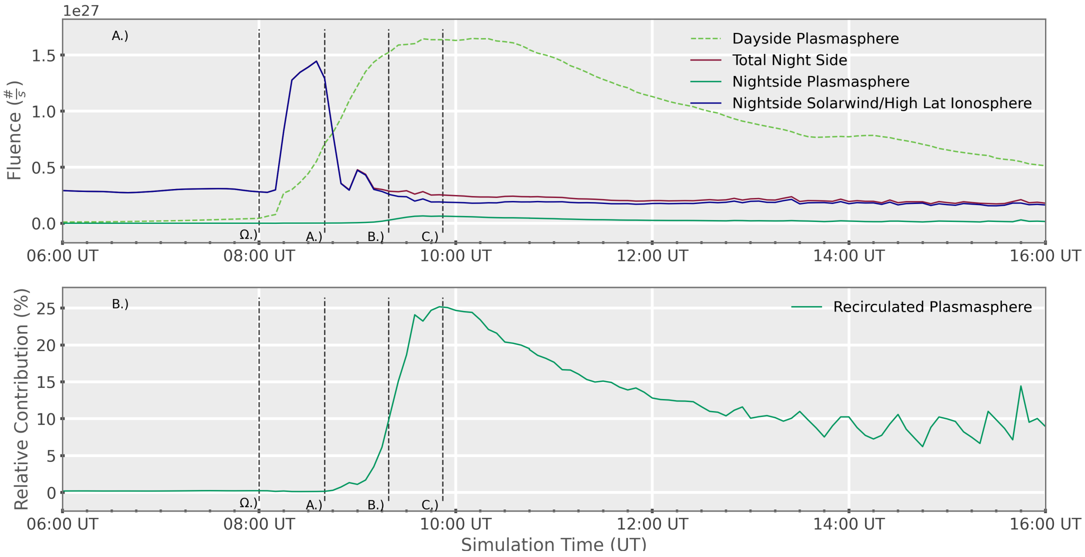

Figure 4.5: The vertical line marked 'Ω.)' corresponds to the beginning of the storm. The vertical lines marked 'A.)', 'B.)', 'C.)' correspond to the times shown in the left, center, and right columns of Figures 4.1 - 4.4 respectively. (A) Fluence of the BATS-R-US fluids as they cross the measurement boundaries on the day and night side 4.1. 'Dayside Plasmasphere' corresponds to the fluence of the plasmasphere material through the dayside plume. 'Total Night Side' refers to the total fluence of all fluids passing through the night side measurement boundary. 'Nightside Solarwind/High Lat Ionosphere' refers to the fluence of the combined solar and polar wind across the night side boundary. 'Nightside Plasmasphere' refers to the fluence of the recirculating plasmasphere through the night side measurement boundary. (B) Relative contribution of the recirculating plasmasphere to the total fluence crossing the night side measurement boundary in the Ideal Square Wave event 4.1. At 0% there is no recirculating plasmasphere, at 50% the recirculating plasmasphere is contributing equally to the combined solar and polar wind.

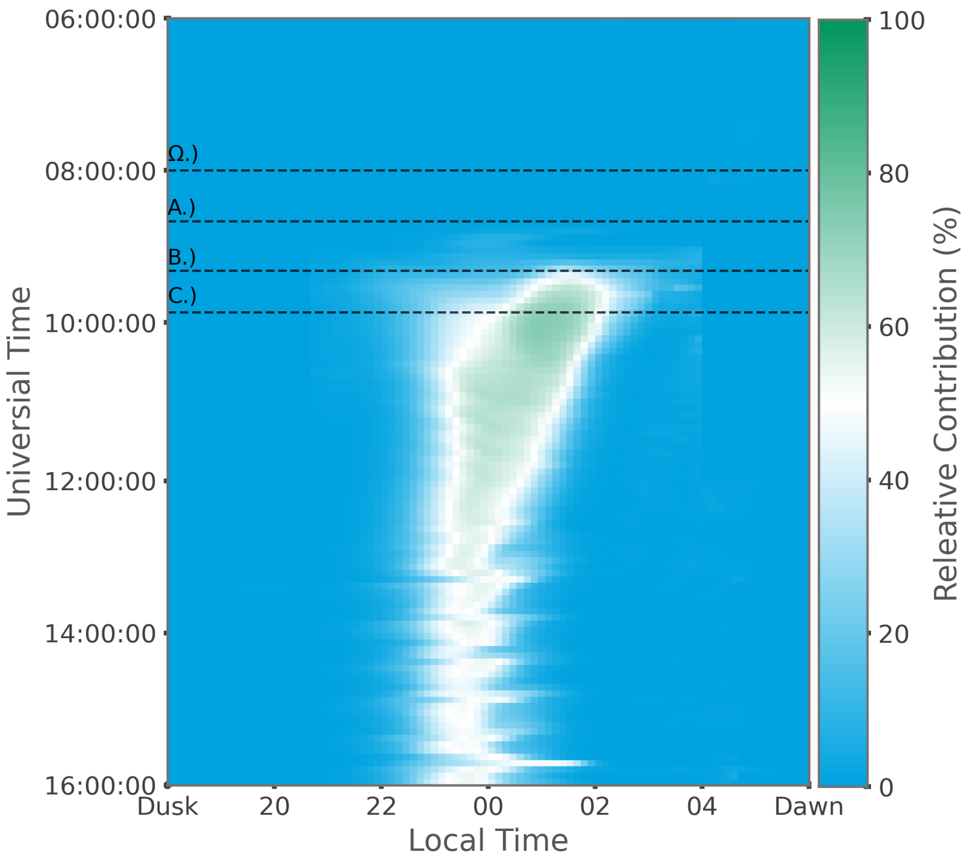

FIGURE 4.6: Relative contribution of the recirculating plasmasphere as a function of local time and simulation time. At 0% there is no recirculating plasmaspheric material. At 50% (white) the recirculating plasmaspheric material is contributing equally to the combined contributions of solar and polar winds. At 100% there is no contribution from the solar and polar winds. The horizontal line marked 'Ω.)' corresponds to the beginning of the storm. The horizontal lines marked 'A.)', 'B.)', 'C.)' correspond to the times shown in the left, center, and right columns of Figures 4.1 - 4.4 respectively.

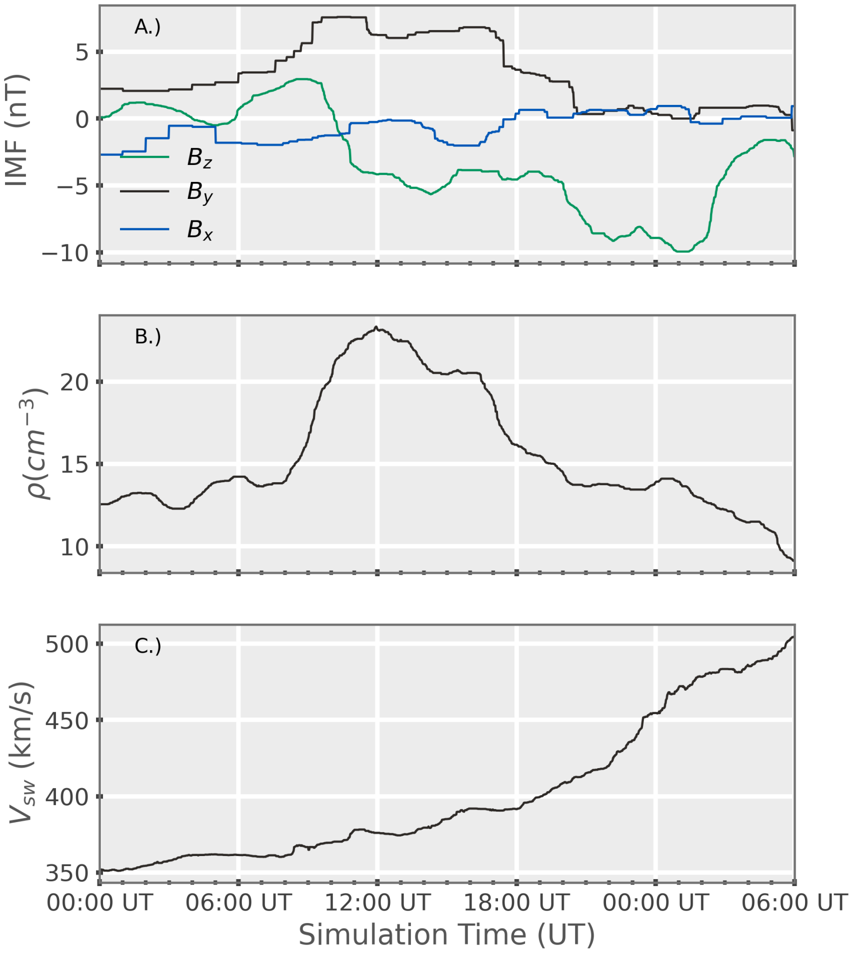

FIGURE 4.7: (A) Magnitude of disturbance from quiet time average of the B_z and B_y components of the IMF. (B) Density of the solar wind as a function of simulation time. (C) Velocity of solar wind as a function of simulation time.

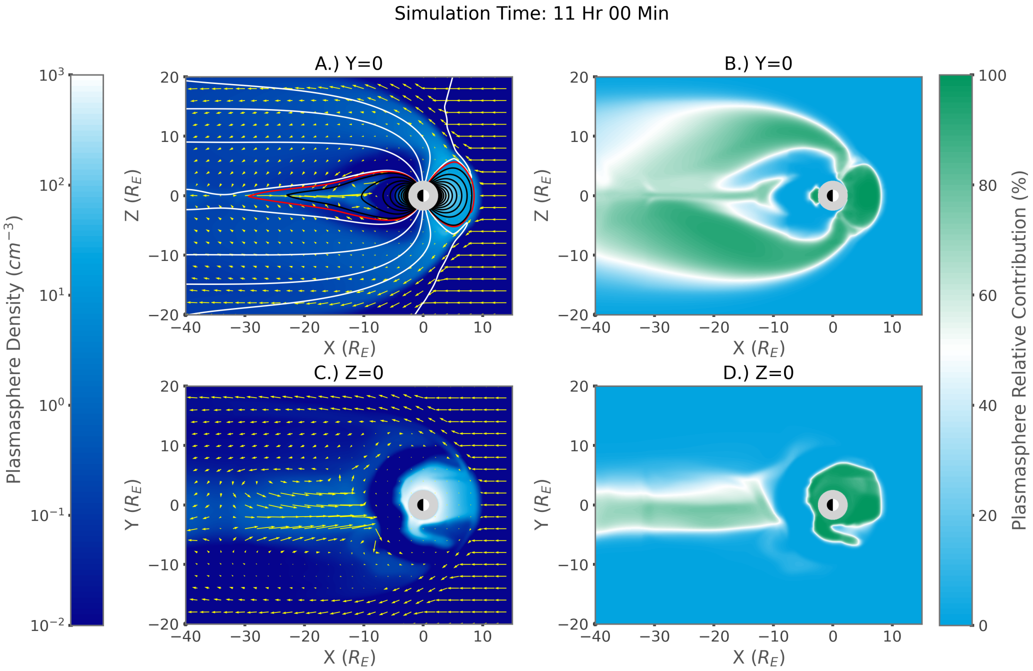

FIGURE 4.8: (A) Y=0 slice showing the density of the plasmasphere fluid, plasmasphere fluid velocity vector field, and magnetic fields. White magnetic field lines are open, black are closed, and red is the last closed magnetic field line. (B) Y=0 slice showing the relative contribution to the total density of the plasmasphere fluid. (C) Z=0 slice showing the density of the plasmaspheric fluid, plasmaspheric fluid velocity vector field. Yellow arrows in both plots are the velocity of the plasmasphere fluid. (D) Z=0 slice showing the relative contribution to the total density of the plasmasphere fluid. All plots are from 11 hours into the Idealized CIR event simulation. This time approximately corresponds to the maximum relative contribution of the plasmasphere material to the total fluence on the night side measurement boundary.

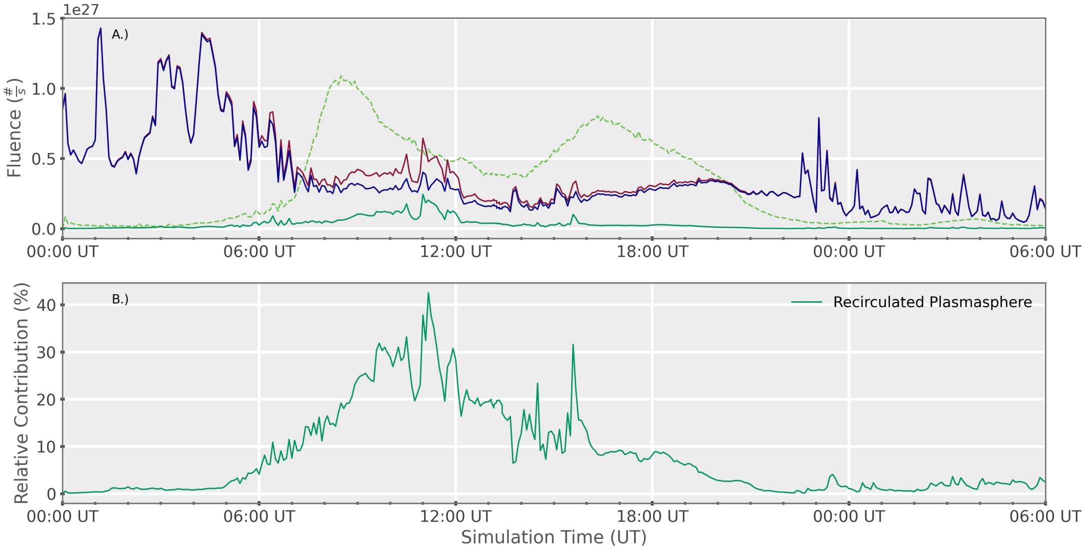

FIGURE 4.9: (A) Fluence of the BATS-R-US fluids as they cross the measurement boundaries on the day and night side 4.1. 'Dayside Plasmasphere' corresponds to the fluence of the plasmasphere material through the dayside plume. 'Total Night Side' refers to the total fluence of all fluids passing through the night side measurement boundary. 'Nightside Solarwind/High Lat Ionosphere' refers to the fluence of the combined solar and polar wind across the night side boundary. 'Nightside Plasmasphere' refers to the fluence of the recirculating plasmasphere through the night side measurement boundary. (B) Relative contribution of the recirculating plasmasphere to the total fluence crossing the night side measurement boundary in the Idealized CIR event 4.1. At 0% there is no recirculating plasmasphere, at 50% the recirculating plasmasphere is contributing equally to the combined solar and polar wind.

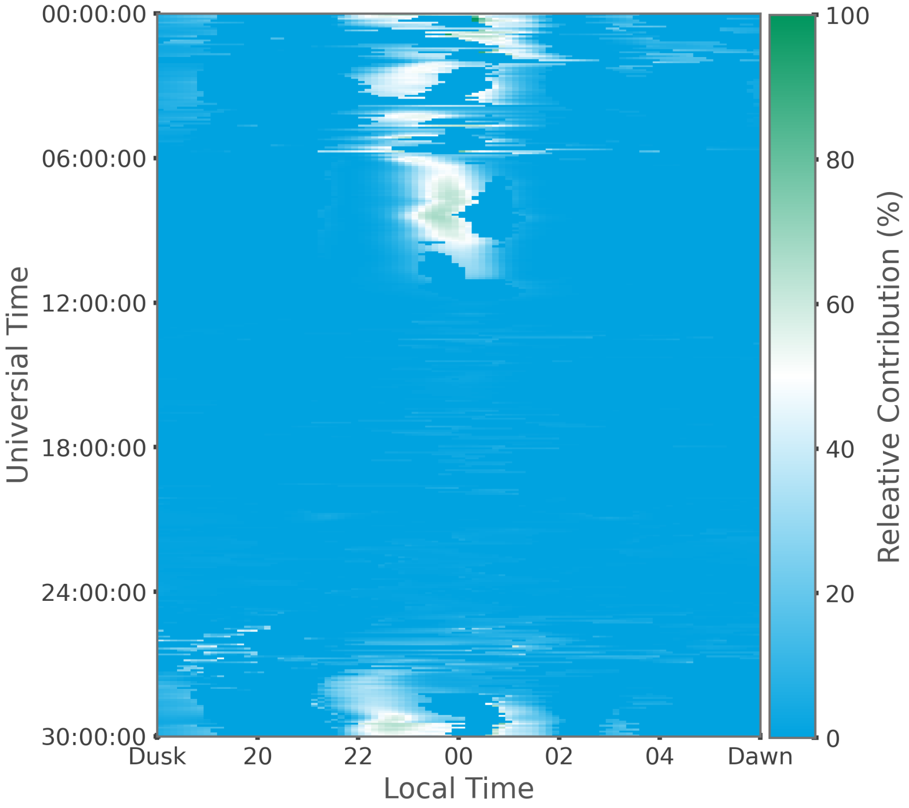

Figure 4.10: Relative contribution of the recirculating plasmasphere as a function of local time and simulation time in the Idealized CIR simulation. At 0% there is no recirculating plasmaspheric material. At 50% (white) the recirculating plasmaspheric material is contributing equally to the combined contributions of solar and polar winds. At 100% there is no contribution from the solar and polar winds.

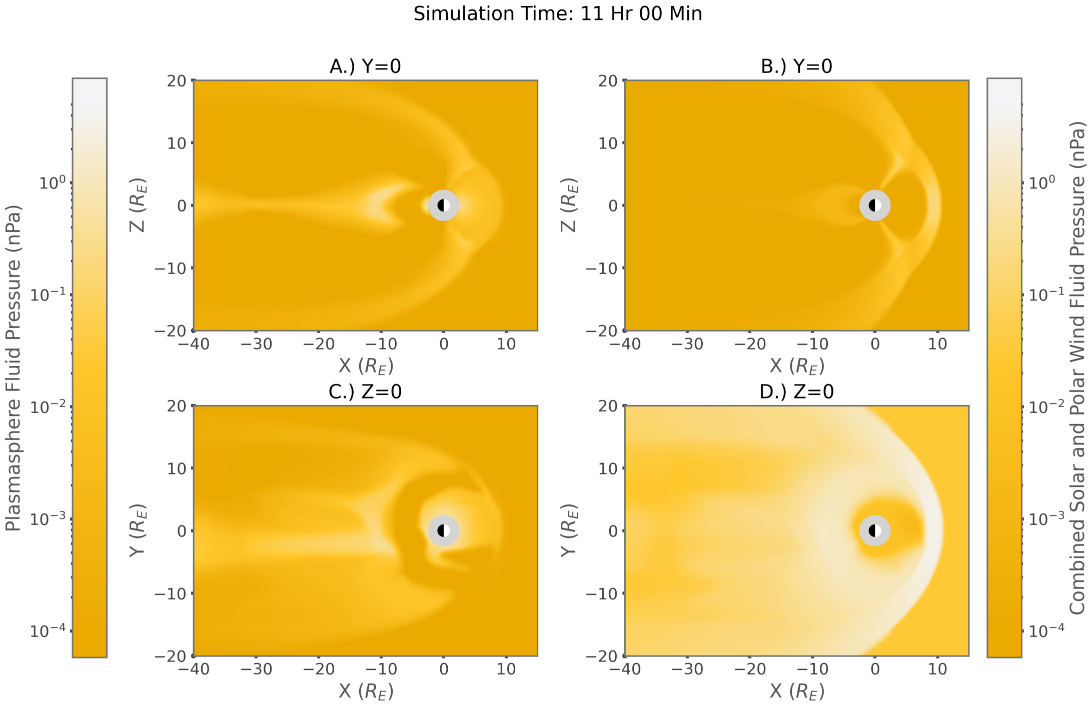

FIGURE 4.11: Taken from BATS-R-US at 11 hours into the Idealized CIR simulation. (A) and (C) Y=0 and Z=0 slices pressure of plasmasphere fluid respectively. (B) and (D) Y=0 and Z=0 slices pressure of combined solar and polar wind fluid respectively.

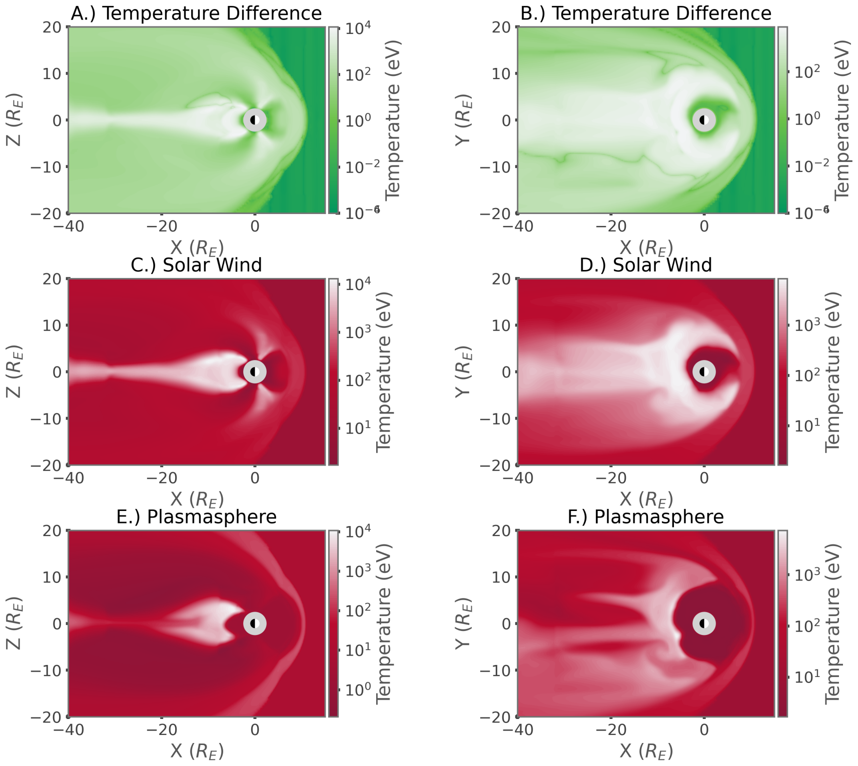

FIGURE 4.12: (Left Column) Y=0 Slices, (Right Column) Z=0 slices. (A) - (B) Absolute Temperature Difference between the two BATS-R-US fluids. (C) - (D) Temperature of the combined solar wind and polar wind fluid. (E) - (F) Temperature of the plasmasphere fluid.

Chapter 5

Developing CIMI for use in Plasmasphere Recirculation Research

In addition to the analysis seen in the previous chapter my dissertation focuses on replacing the Dynamic Global Core Plasma Model (DGCPM) from the configuration in 3.1 with the Comprehensive Inner Magnetosphere-Ionosphere Model (CIMI), as seen in Figure 5.1. There are several strong motivating reasons for this change including: self-consistently determining the contribution of the recirculating plasmasphere to the ring current energy, self-consistent calculation of the magnetic field in regards to the evolution of the plasmasphere and ring current, and self-consistent effects of region 2 field-aligned currents on the evolution of the ionosphere conductance. A major theme of the Chapter 4 is the advantage that the self-consistent treatment of the recirculating plasmasphere has on the amount of

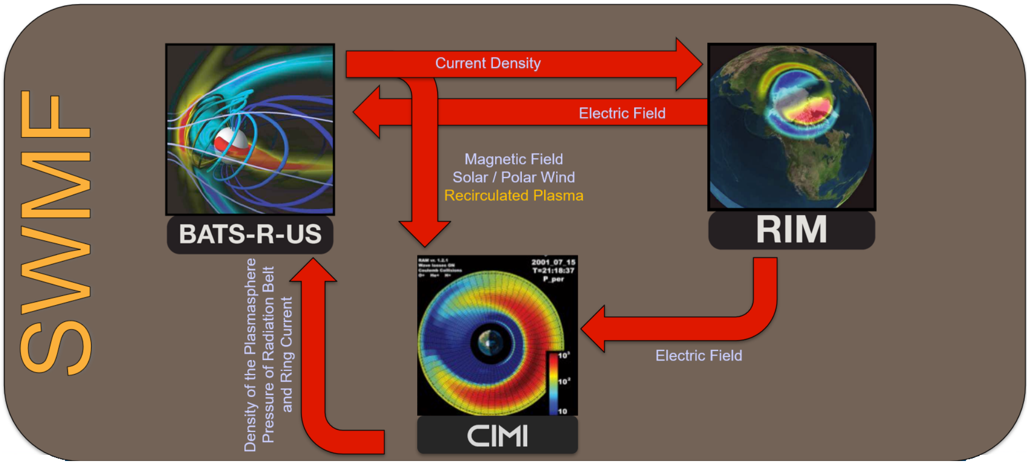

FIGURE 5.1: Configuration and couplings of the SWMF with BATS-R-US (GM), RIM (IE), CIMI (IM).

recirculating plasma relative to earlier studies. By replacing DGCPM with CIMI we extend the self-consistency of the simulation to new physical domains.

Figure 5.1 describes the coupling of the SWMF sub modules when CIMI is used in place of DGCPM. Notable is the additional coupling between CIMI and BATS-R-US which not only passes the density of the plasmasphere, but also the density and pressure of plasma found in the ring current and radiation belts. This new coupling, compared to the DGCPM set up, has the advantage of driving field-aligned currents in the BATS-R-US model. These currents provide a sharper gradient than what is produced in BATS-R-US, for reasons we will discuss later, which in turn provide a better conductance calculation in RIM, and thus a better electric potential, and variables derived from this. This improvement in the output of RIM is then fed back into CIMI through the electric field which helps to drive the strict ExB drift of the plasmasphere as well as the convection of particles in the ring current and radiation belts. Therefore, although not shown in Figure 5.1, CIMI and RIM are coupled in a two-way manner via an implicit coupling through BATS-R-US in the form of the field aligned currents.

Through out this chapter we will be comparing the configuration of the SWMF presented in the previous chapter (summarized in Figure 3.1) to a new configuration of the SWMF to be discussed throughout this chapter (summarized in Figure 5.1). To distinguish between these two configurations, and the configurations of the physics models contained therein, I will refer to aspects of the previous configuration as the 'DGCPM configuration' or 'SWMF-DGCPM' or the 'BATS-R-US-DGCPM' et cetera. I will refer to the aspects of the current configuration as being of the 'CIMI configuration' or 'SWMF-CIMI' or the 'BATS-R-US-CIMI'.

The task of replacing DGCPM with CIMI has not been trivial. The largest obstacle in the way of completing the study began in the previous chapter is the development of new features in CIMI. Currently CIMI's outer boundary takes information from BATS-R-US about the energy and density of plasma at those L-shells and feeding this information into its calculation for the phase space densities of its various populations. The populations in CIMI are based on the species of the plasma represented with no obvious mechanism to have a 'multi-population' ability, analogous to the multi-fluid capability of BATS-R-US. Because the MHD simulation is comprised solely of hydrogen this would mean that both the solar and polar wind fluid and the plasmasphere fluid, after recirculation, would be fed into the same population within CIMI. Consequently, in the coupling from BATS-R-US to CIMI we lose the ability to distinguish the plasmasphere from the solar wind and polar wind which is critical in the analysis preformed in the previous chapter. In addition, because CIMI lacks the ability to distinguish the solar and polar wind form the recirculated plasmasphere, if we wanted to see the affect on the total energy of the ring current that recirculating plasmapshere material exerts we would need to run the simulation multiple times. We would need to compare two runs, one with, and one without the recirculating plasmasphere to see how much of the ring current energy is provided by the recirculating material. This requirement would hinder the self-consistency at the heart of this research. The literature on the numerical differences which can be expected between a given simulation with the same settings is lacking. Thus our conclusion would be left at the qualitative stage unless we undertook a much larger effort to quantify the minor differences you might expect to evolve from a simulation run many times ourselves. Thus, it is desirable to have a configuration of the SWMF and CIMI in which the recirculating plasmasphere is treated as a separate population than that of the other hydrogen species. Such a configuration would enable us to distinguish within one simulation how much of the total ring current energy is provided by the recirculated plasmapshere versus the other contributors.

The addition of this new population of recirculated plasmasphere within CIMI represents the lion share of my work, and is still ongoing. While it is relatively simple to add a new population in a naive way, it is difficult to implement the new capability in a way that is both efficient in terms of code execution and that does not disrupt the veracity of the established model. The remainder of this chapter will deal with all the changes that need to be made to the SWMF and physics domains to add a new population to CIMI, have it coupled in the desired way with BATS-R-US, and how to verify stages of code development and troubleshoot issues.

The first step in creating a new fluid is to configure the equation files for the physics domains to be implemented. New equation files are required for CIMI, as a new population is being added. In addition, a new equation file is needed for BATS-R-US as well as, with a new fluid in CIMI, the BATS-R-US file must be configured to properly couple to that new fluid.

The files for the original attempts and the current versions can be found on github at https://github.com/spacecataz/swmf_runfiles.git on the branch named CIMIdev in the folder labeled 'psphere_coupled'. In addition to these equation files, modifications were made to one subroutine, IM_get_for_gm, in the wrapper for CIMI. All files modified from their original SWMF versions are contained on the github repository with detailed instructions on how to integrate them into a fresh install of the SWMF.

The BATS-R-US equation file will define the name, number, and index of variables and the number, name, and species of fluids, how the variables relate to each other (i.e. which variables are density, momentum etc.), and which variables can be positive, negative, or both. Initially we did not use a prefix to denote the solar wind and polar wind fluid in the new equation while we used the prefix 'HpPs' for the plasmasphere. The the solar wind and polar wind density would be 'rho' and the plasmasphere density would be 'hppsrho'.

The CIMI equation file proves a similar function as that of BATS's equation file. It defines the number, name, file extension, index, charge exchange cross section, mass, and the density and temperature ratio for each species to be included. Note: here species basically means populations as it is a new inovation within this work that two populations share a species but are separate from each other. Similar to BATS-R-US, variable names, how the variables relate to each other (i.e. grouping into density, parallel pressure etc.), and which variables are to be coupled to the GM component are set in this file. The CIMI equation file also has controls for aspects of the ionosphere and Earth's radius or dipole moment. As we couple to RIM for the ionosphere component and keep the standard Earth radius and dipole moment, we won't go into detail about them. In a divergence from BATS-R-US we specify the total population variables in addition to those for each species. As a result the normal hydrogen population gets the prefix 'Hp', unlike BATS-R-US, and the recirculating plasmasphere gets the prefix 'HpPs', similar to BATS-R-US, while the total population variables did not have a prefix. This divergence in the naming schemes will lead to problems which we will come back to.

As we do not wish to include recirculating plasmasphere in every configuration of CIMI and BATS-R-US of the SWMF (i.e. single fluid MHD in BATS-R-US) a flag is added to the equation file for CIMI and to the file IM_wrapper.f90 which will only search for and couple the 'HpPs' population if it is set to true. The flag is added to, and then marked false in, other CIMI equation files. As coupling is a unidirectional process multiple subroutines are used for each combination of models to be coupled, i.e. IM_get_for_gm to pass information from CIMI to BATS-R-US and IM_put_from_gm to do the reverse.

Once these changes were implemented a simulation with the standard Space Weather Prediction Center (SWPC) grid was set up and run. The simulation was to only run for a few couplings between the IM and GM component to test if the coupling was behaving properly and the output files were reasonable. The output files were unreasonable containing NaNs (Not a Number) as well as other nonsensical data output. This stage is where troubling shooting begins. There are several ways in which nonsense data can make it to the output: bad values in BATS-R-US being passed through the SWMF control module and into CIMI then properly propagating through CIMI, bad assignment of data from one variable to the other during coupling (either in the SWMF control module or the CIMI wrapper), CIMI corrupting or otherwise mishandling the data after coupling, and bad writing of data to output file. Print statements are added throughout the code (SWMF, BATS, and CIMI) at key points to determine where the failure occurred.

As we will need to refer to the same variables between multiple models I will adopt the system of capitalizing some of the letters of CIMI's variables while leaving BATS-R-US's variables in all lower case. After studying the output of the print statements we find that there are actually two errors compounding, creating the same problem. The fundamental issue the similarity of the variable names between the two hydrogen fluids in BATS-R-US and CIMI. 'Hp' and 'HpPs' both begin with the same letters, and SWMF's subroutines are designed to take the first fluid name, strip it off and then match the remaining string to a variable. For example, 'HpRho', the density of the solar wind and polar wind, becomes 'Rho' and matches to the case 'rho' in the IM wrapper. When going from IM to GM this behaviour is correct. However, in the two cases this behaviour fails. When going from GM to IM, the BATS-R-US variable 'rho' is the density of the combined solar wind and polar wind, this matches to 'Rho' in CIMI, which is the total density, the sum of HpPsRho and HpRho, which is the density of the recirculated plasmasphere and everything else respectively. The second case being the variable 'HpPsRho'. When going from GM to IM 'hppsRho' becomes 'psrho', as the first fluid name 'hp' is striped from 'hppsrho' while the 'hp' population is being coupled. This mistake causes CIMI to fail to match the variable to 'HpPsRho'. At the same time in the output files 'psrho' and other plasmasphere ('hpps') variables are being marked as being an unknown variable of the combined solar wind and polar wind ('hp') fluid, rather then marked as a plasmasphere fluid.

My first attempt to resolve this issue was simply to teach CIMI how to handle variables like 'pshro', 'psp', and others. This attempt was short lived, as this necessitated adding these variables to the tools used to manage the simulations output as well. The second solution is to simply rename the 'HpPs' variable to something that won't be confused with 'Hp'. Thus, throughout the rest of the report the plasmasphere will be referred to as 'PsHp'. This solution did require making additions to the library of variables names contained within the SWMF, though it was a relativly simple process.

After the various naming issues were resolved I hard coded certain values into the wrapper of the IM component. This test would reveal if the newly added recirculating plasmasphere population within CIMI was being treated properly. By hard coding values I could preform the calculation by hand as to what values of density and temperature I could expect to find in the simulation's output. As the SWMF converts all values to SI units during coupling I overwrote the values of the density and pressure for the Hp and HpPs populations during the GM to IM coupling in the IM wrapper. The selected values where 2.5e-20 kg/m^3 for the density and 1.2e-8 Pa for the pressure. These values should result in a number density of 15 cm^{-3} and temperature of 5 keV in both the Hp and HpPs populations. The conversions were calculated through the relationships,

$$n_s = \rho_s/(m_p * amu) \tag{5.1}$$

where n is the number density, ρ is the mass density, m_p is the proton mass and amu is the atomic mass unit of the species of the population. Though we do calculate the electron pressure in CIMI, electrons are not treated as a separate species. The electron density is assumed to be equal to that of the other populations so that quasi-neutrality is maintained. As all are populations in CIMI are hydrogen amu is 1 in all cases. The conversion from pressure to temperature was done by,

$$T_s = P_s/n_s * c \tag{5.2}$$

where T_s and P_s are the temperature and pressure of a given population respectively. c is a conversion factor between joules and electron volts equal to 6.2415e18.

The output files of both BATS-R-US and CIMI were found to have the predicted values.

Now that we have confirmed the new population is coupling correctly between the GM and IM components we moved on to a longer test simulation. Using the same grid as the SWPC configuration we ran the simulation for 40 minutes to see how it evolved. The result of this can be seen in Figure 5.2. Figure 5.2 shows the density in BATS-R-US and CIMI in the equatorial plane. The Top Left panel shows the density of the plasmasphere in CIMI, the Top Right shows the density of the plasmasphere in BATS. As can be seen these agree well, though CIMI is slightly more dense then BATS-R-US. The Center Right and Bottom Right panels show the density of the solar wind and polar wind population or fluid in CIMI and BATS-R-US respectively. These also agree well, within the region of coupling. The Center Left panel shows the recirculated plasmasphere population in CIMI. Though the IMF condition of the test is all northward some recirculated plasma appears in CIMI. This appearance is due to the dynamic outer boundary of CIMI which will move back and forth following the magnetic field. As can be seen in the Top Left panel the plasmasphere is dense and the plasmapause extends out to 9.5 Re, near the outer boundary. In BATS-R-US as its magnetic field moves slightly further out then CIMI's, the magnetic field lines drag the plasmasphere material in their flux tubes with them. When the models couple again, the plasmasphere material is now treated as an outer boundary condition for CIMI and is thus added to the recirculated plasmasphere population. While it is to early in the storm to begin recirculation in the manner described in the literature, it does demonstrate that the coupling between CIMI and BATS-R-US is behaving as intended.

Despite the successes demonstrated by Figure 5.2 there are also manifest issues present. A minor issue which looks far worse then it is, is the artefacts in the CIMI plots taking the form of large triangles along the dayside outer boundary. These artifacts are caused by the plotting algorithm of spacepy, an open source tool set which handles SWMF simulations outputs, and does not reflect structures present in the numbers of the simulation. CIMI is a portion of the SWMF not often used in this manner, and as such the maintainers of spacepy have yet to iron out all the kinks. Unfortunately, I lack the ability to resolve the issue myself so 2D plots of CIMI will have to suffer this inconvenience. The other issues present in Figure 5.2 is the odd shape of the plasmasphere and solar wind in CIMI and BATS-R-US, and the saturated plasmasphere of CIMI's default initial condition. By 'odd shape' I am referring to the wings coming off the plasmasphere in the CIMI component extending along the positive and negative y-axis and slightly along the negative x-axis. The wings originate in CIMI and propagate to BATS-R-US. The CIMI origin is clear in a time sequence of Z=0 slices of the CIMI and BATS-R-US plamsasphere density values. CIMI's initial condition for the plasmasphere, while it is physically

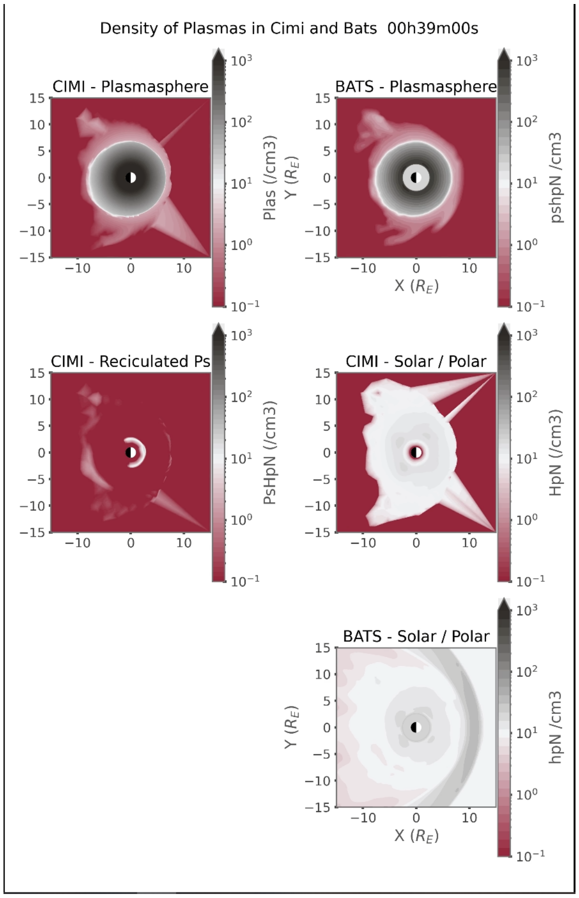

FIGURE 5.2: (Top Left) Plasmasphere from CIMI's embedded plasmasphere code. (Top Right) Plasmasphere fluid in BATS-R-US. (Center Left) Recirculated plasmasphere population in CIMI (Center Right) Combined Solar and Polar Wind population in CIMI (Bottom Right) Combined Solar and Polar Wind fluid in BATS-R-US.

possible, is a rare circumstance that does not often occur. As such it is difficult to make a direct comparison between the results of the CIMI simulation and that of the early DGCPM simulations as DGCPM has a more typical initial plasmasphere. It is desirable to compare the DGCPM and CIMI runs as this serves to verify that the CIMI code has been properly integrated. CIMI has been used within the SWMF before, but we have modified it with the addition of a new population and altered how it couples, thus we must ensure CIMI is still behaving properly. While both CIMI and DGCPM deal with different physical domains they overlap at the plasmasphere. CIMI, in addition to the plasmasphere, models the radiation belts and ring current. CIMI's plasmasphere code is a modified version of DGCPM. Thus, during periods of quite time, and nominal solar wind conditions, we would not expect the quiescent ring current or radiation belts to substantially change the configuration of the inner magnetosphere or plasmasphere. The plasmasphere, radiation belt, and ring current are often co-spatial with one another, separated by the energies of the plasma which make up their populations.

The wings present in the CIMI plasmasphere complicate the comparison to the earlier DGCPM runs in other ways. These wings feed the night side tail population through recirculation around the flank, similar to the early recirculation seen in the DGCPM based CIR run (Figure 4.8). In addition to around the flank movement of plasmasphere material into the night side tail, the plasmasphere being so full out to the CIMI boundary caused a significant amount of plasma to be pulled off the night side plasmasphere and into the tail. This early leakage of material is explained by several mechanisms. Numerical diffusion across the boundary between blocks of different grid resolution, and relaxation of the magnetic field lines after the time accurate portion of the simulation began. As the magnetic field lines relaxed from the initial condition some plasmasphere material was stripped from the night side plasmasphere into the tail. Numerical diffusion off the dayside pole, and on the wings of the inner magnetosphere in the equatorial plane, caused a large amount of material to leak out of the plasmasphere quickly.

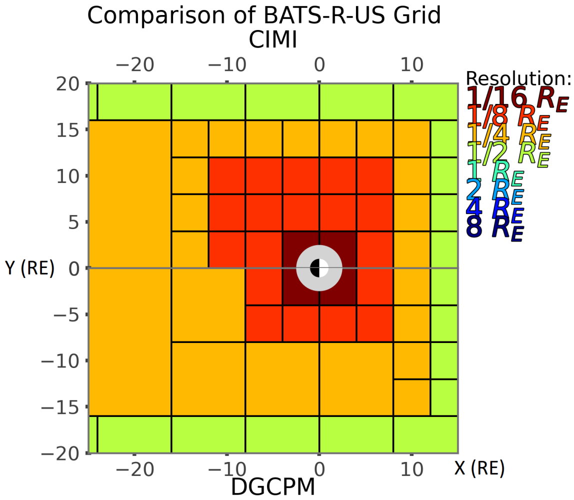

FIGURE 5.3: Comparison of the Grid between CIMI and BATS-R-US in the Z=0 plane. The positive y portion of the plot shows the grid of BATS-R-US when in the configuration of the SWMF with CIMI as the IM component. The negative y portion of the plot shows the grid of BATS-R-US when in the SWMF with DGCPM as the central component. (GSM coordinates)

To combat the numerical diffusion problem we increased the resolution of

BATS-R-US to be slightly higher then it was in the case of the SWMF-DGCPM simulations present in chapter 4. The new resolution was increased from the 1.9 million cells of the SWPC configuration to 9.2 million cells. This is a higher cell count then in the configuration of the BATS-R-US-DGCPM presented in chapter 4, which sat at 7.9 million cells. Figure 5.4 compares the resolution of the new grid for BATS-R-US to the grid used in the previous chapter in the Y=0 plane. The positive z-portion of the plot shows the block tree in the Y=0 plane for BATS-R-US-CIMI, while the negative z portion shows the block tree when BATS-R-US-DGCPM. As can be seen, we slightly extend the 1/16th cell area on the night side of Earth so that the large initial plasmasphere would be entirely contained within it. The additional cells in this configuration compared to the DGCPM configuration are almost entirely present on the night side extending from ± 10-12 R_E in both the Z and Y directions of the GSM coordinate system.

Figure 5.5 shows the equatorial plane of BATS-R-US-CIMI after 1 minute of time accurate simulation. The top half of Figure 5.5 shows the density and velocity vector field of the plasmasphere fluid, while the bottom half shows the grid of BATS-R-US. We see that plasma has a tendency to flow along the boundary of cells, rather than at arbitrary angles to the boundary. We see circulation occur between blocks of different resolution on the night side. Several structures of the velocity vector field show clear delineations between different blocks of cells, or

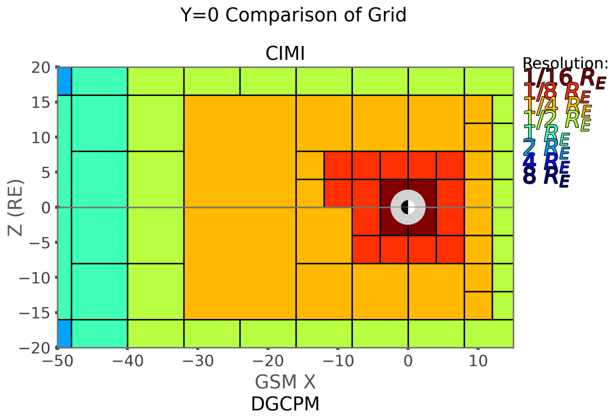

FIGURE 5.4: Comparison of the Grid between CIMI and BATS-R-US in the Y=0 plane. The positive z portion of the plot shows the grid of BATS-R-US when in the configuration of the SWMF with CIMI as the IM component. The negative z portion of the plot shows the grid of BATS-R-US when in the SWMF with DGCPM as the central component. (GSM coordinates)

grid resolutions. These flows are the visual manifestation of numerical diffusion across cell boundaries. Figure 5.6 has a shockingly clear case of this in the boundary between the 1/8th and 1/4 grid cells in the northern and southern hemispheres. Figure 5.6 shows the same thing as Figure 5.5, but in the Y=0 plane. We see a large amount of dayside plasmasphere material go out the dayside lobes from the very beginning.

Figure 5.7 shows the retaliative contribution to the total flux that the plasmasphere fluid is providing at various Earth Radii in BATS-R-US. This plot mirrors those of 4.5B and 4.9B. The red curve measures the fluence going from dawn to

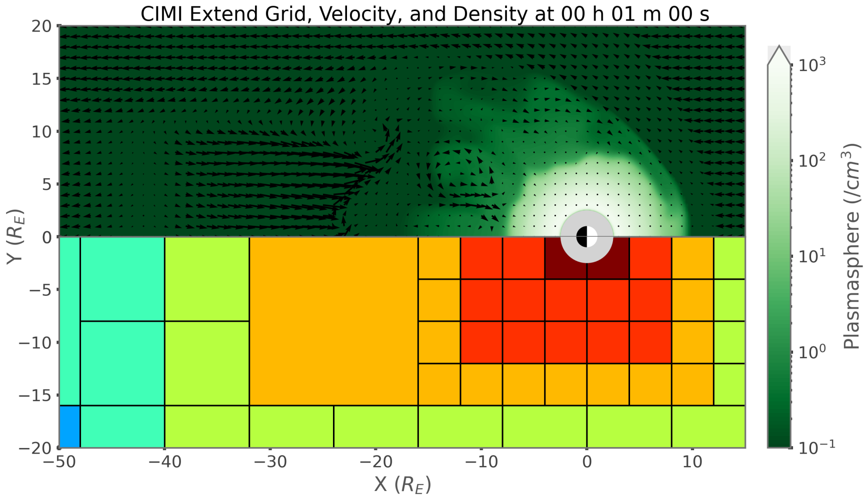

FIGURE 5.5: (Top) Y=0 slice of the state of the plasmasphere in BATS-R-US at 1 minute. Color map is of the density of the plasmasphere fluid. Black arrows show the velocity vector field of the plasmasphere. (Bottom) Grid of BATS-R-US with 9.2 million cells.

dusk and ± 60° latitude on the night side of the planet with a constant radius of 10 R_E. This is identical to the measurement surface on the night side in the previous chapter. The blue, green, yellow, and black curves measure the flux through the same spread of MLT and latitude, but at 15, 17,19, and 21 R_E respectively. The simulation shown ran on the same grid as described in Figures 5.3 - 5.6. The simulation ran for 10 hours using the same solar wind conditions as the Ideal Square Wave Event from 4. As can be seen the CIMI plasmasphere provided an immense amount of plasma to the tail even early in the simulation. As the CIMI plasmasphere during quite time is driven to saturation, this caused the plasmasphere to act

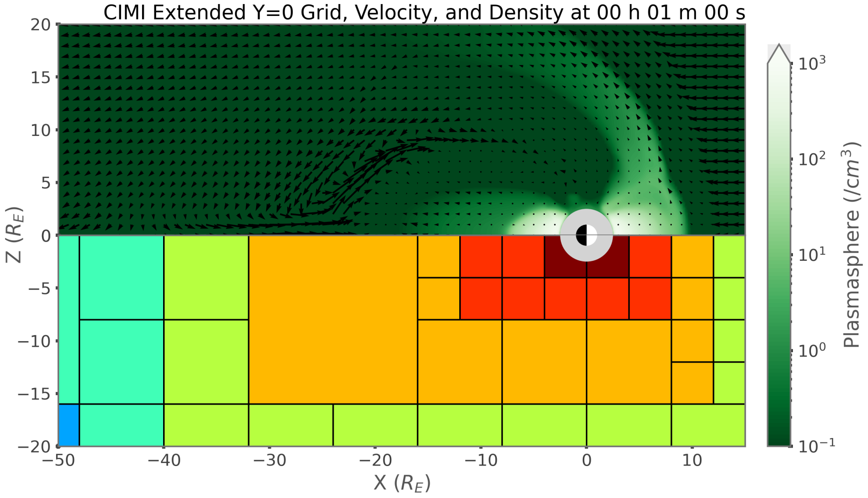

FIGURE 5.6: (Top) Y=0 slice of the state of the plasmasphere in BATS-R-US at 1 minute. Color map is of the density of the plasmasphere fluid. Black arrows show the velocity vector field of the plasmasphere. (Bottom) Grid of BATS-R-US with 9.2 million cells.

as an unrealistic source of plasma in the tail. Because of this we have to abbadon the run, and attempt to restrain the plasmasphere further. While the simulation failed to provide results similar to those in chapter 4 it does demonstrate that we are still suffering from a large amount of diffusion along the boundary of the plasmasphere in CIMI.

We again in creased the grid, from 9.2 million to 18 million cells and preformed the simulation for 1.5 hours. Figures 5.8 5.9 replicate Figures 5.6 5.7 for the Z=0 and Y=0 planes respectively. The region of 1/16 R_E cells has remained the same. In the Z=0 plane the region of 1/8 R_E cells has been pushed to ± 15 (up from

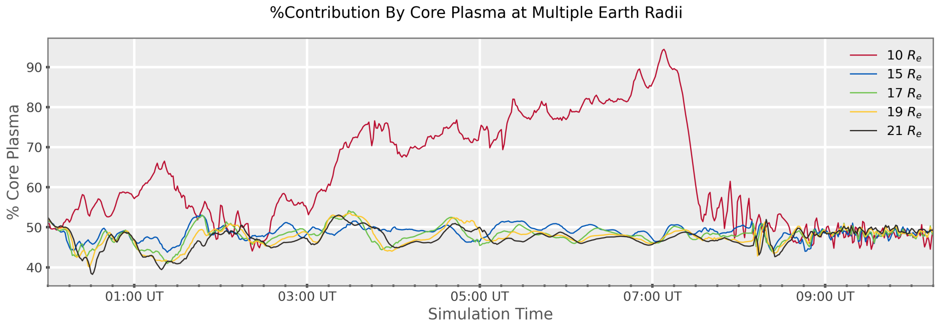

FIGURE 5.7: Relative contribution of the recirculated plasmasphere to the total fluence at various Earth Radii in the tail.

-12 to 10 R_E) along X and ± 16 along Y (up from ± 12 R_E), while in the Y=0 plane the region of 1/8 R_E has been pushed out to ± 12 R_E (up from ± 8 R_E). By compassion between the 9.2 million cell and 19 million cell plots we see that there is a definite decrease in the around of plasmasphere material which leaks out of the plasmasphere early in the simulation. The wings around the plasmasphere in the Z=0 case are substantially smaller while the circulation on the night side between the blocks of different resolutions has vanished. In the Y=0 plane, we see that the day side magnteosheath isn't filled with plasma as it was in the previous simulation. This improvement indicates we are no the right track with correcting the behaviour of the plasmasphere during quite time conditions.

Figure 5.10 shows the state of the BATS-R-US fluids at 1.5 hours into the simulation. As can be clearly seen, the issue of omni-present plasmasphere material

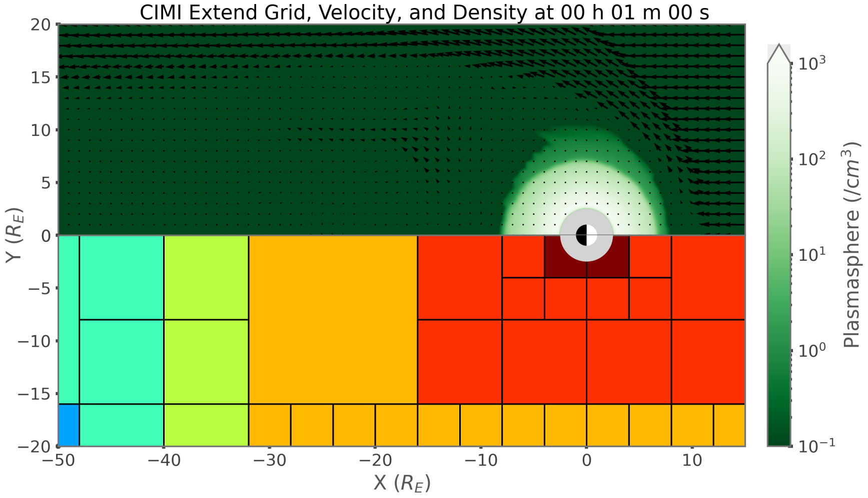

FIGURE 5.8: (Top) Z=0 slice of the state of the plasmasphere in BATS-R-US at 1 minute. Color map is of the density of the plasmasphere fluid. Black arrows show the velocity vector field of the plasmasphere. (Bottom) Grid of BATS-R-US with 18 million cells.

continues. The left columns of Figure 5.10 show the plasmasphere fluid of BATS-R-US while the right column shows the combined solar wind and polar wind fluid. the black arrow vector fields indicates the velocity field of the appropriate fluid, while the color maps correspond to the density of the represented fluid. The top row of Figure 5.10 shows the Z=0 plane while the bottom row shows the Y=0 plane.

Figure 5.10 demonstrates that while increasing the resolution helps the issue of plasmasphere leakage, it is not the soul solution. This fact additionally indicates that numerical diffusion is not the issue which we need to tackle. In addition to the grid, the initial condition of CIMI's plasmasphere is responsible by placing a dense

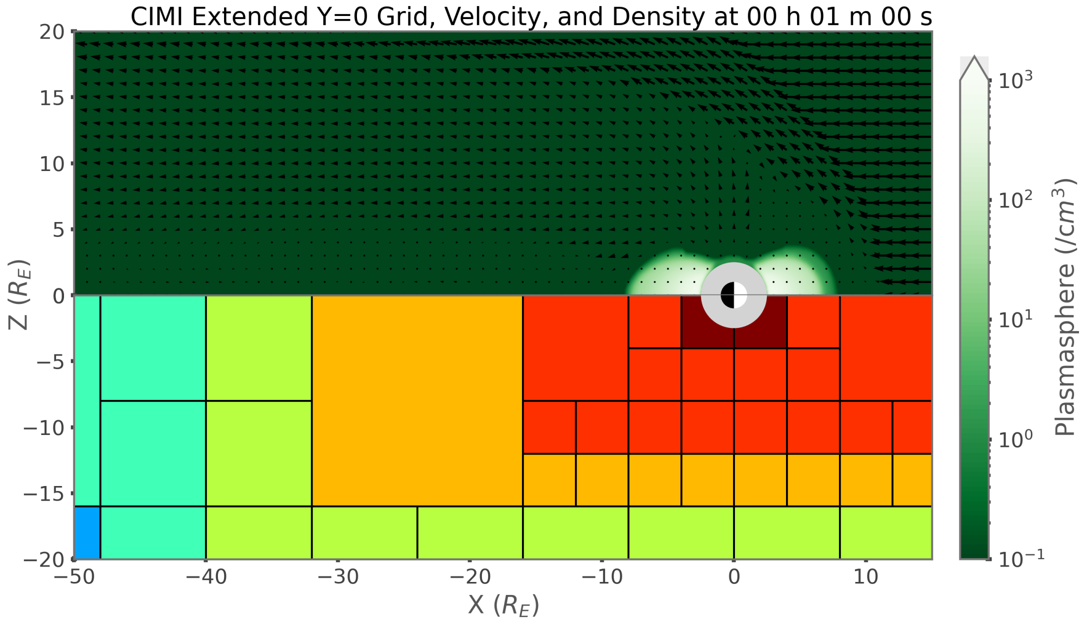

FIGURE 5.9: (Top) Y=0 slice of the state of the plasmasphere in BATS-R-US at 1 minute. Color map is of the density of the plasmasphere fluid. Black arrows show the velocity vector field of the plasmasphere. (Bottom) Grid of BATS-R-US with 18 million cells.

plasmasphere out to high L-shells. To make the comparison between DGCPM and CIMI easier, and to resolve the issue of CIMI's initial condition, I altered CIMI to use the same initial density profile of DGCPM as its initial condition for the plasmasphere. Unmodified CIMI's initial plasmasphere is generated by running the plasmasphere component for one day, filling the plasmasphere according to equation 2.16. CIMI and DGPCM of course run on separate grids, as such we must interpolate the density profile from DGCPM's grid to that of CIMI. Using such

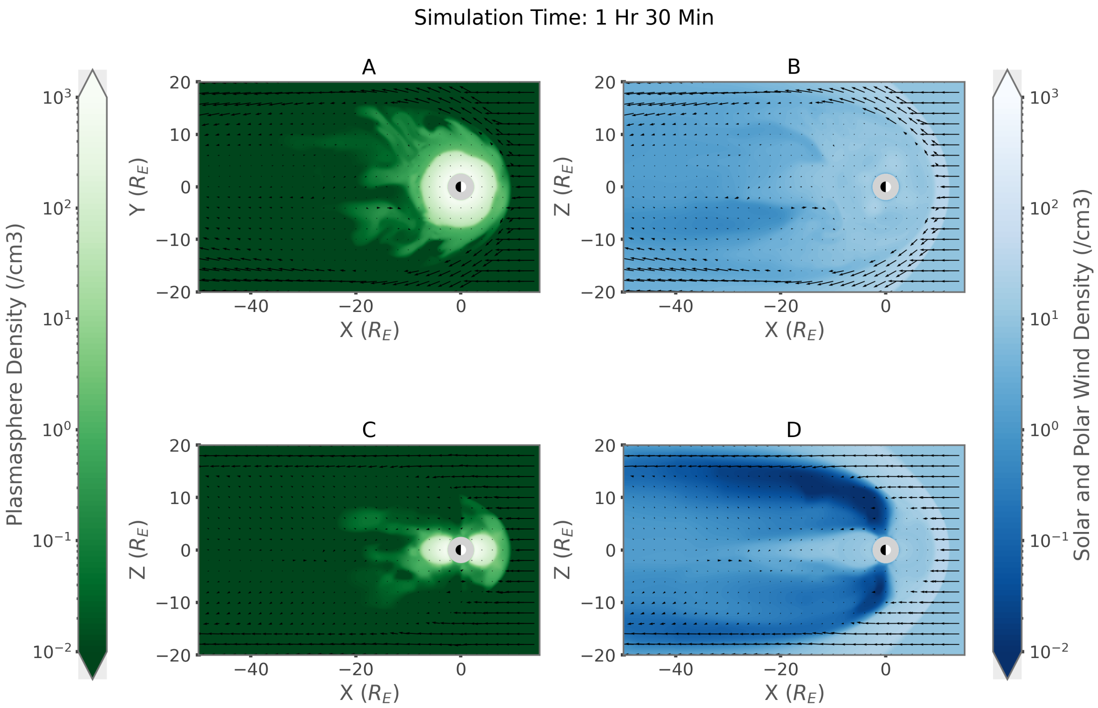

FIGURE 5.10: (A) Z=0 slice of BATS-R-US showing the density and velocity vector field of the of the plasmasphere. (B) Z=0 slice of BATS-R-US showing the density and velocity vector field of the of the combined solar wind and polar wind fluid. (C) Y=0 slice of BATS-R-US showing the density and velocity vector field of the of the plasmasphere. (D) Y=0 slice of BATS-R-US showing the density and velocity vector field of the of the combined solar wind and polar wind fluid.

functions found in the open source python library numpy the density profile seen in Figure 5.11 was produced. Figure 5.11 shows the initial of DGCPM plotted on its own grid in the left dial plot, while the right dial plot shows the same density profile interpolated to CIMI's grid. CIMI's grid extends beyond that of DGCPM as such at those L-shells the interpolation breaks down somewhat as can bee seen. The initial interpolation was modified by hard coding the plasmasphere beyond 10 R_E to be match the background required by the numerical simulation .001 cm^{-3}. Note that the density labels of Figure 5.11 are in the SI units of $/m^{-3}$. In cm^{-3} the goes from .1 to 1000 cm^{-3}.

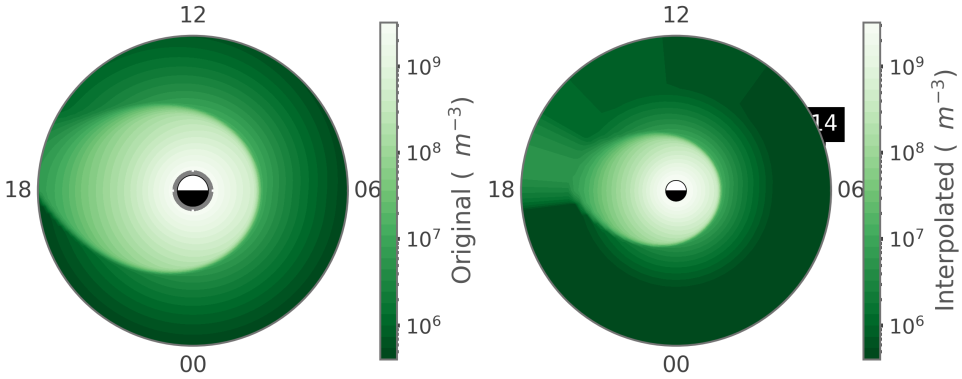

FIGURE 5.11: Comparison of DGCPM's initial condition on its own grid against the same density profile on CIMI's grid. (Left) Initial Condition of DGCPM on its own grid, extending out to 10 R_E. (Right) Initial Condition of DGCPM interpolated onto CIMI's grid. CIMI's grid initially extends past 10 R_E.

Figures 5.12 and 5.13 again mirrors Figures 5.5, 5.6, 5.8, and 5.9. The grid resolution was again increased, this time to 24 million cells. Along the x-axis the

1/8 R_E region was shifted to -20 R_E to 12 R_E. The dayside extension of the 1/8 R_E region was brought closer to Earth in comparison to the 18 million cell run as the area between 12-15 R_E along the X-axis was contained entirely within the solar wind, and a such does not require higher resolution. This shift allows us to use the cells deployed more efficiently. Along the Y and Z-axes the 1/8 R_E was pushed out to ± 16 R_E. In both Figure 5.12 and 5.13 we see that the plasmasphere fluid will fill out the same silhouette as in the 18 million cell run, the plasmapause is a couple R_E closer to Earth.

After 30 minutes however we see that again the plasmasphere has entered into the tail region in the equatorial plane. Figure 5.14 shows the state of the fluids of BATS-R-US similar to Figure 5.10. The problem persists and worsens as the run continues. Compared to the original attempt in Figure 5.2 the situation has improved greatly, and we are closer to being able to make a direct comparison to the DGCPM runs presented in Chapter 4. We have seen how the initial density profile and the resolution of the simulation have improved the our ability to produce a more typical plasmasphere in CIMI. At this point it is clear that the primary issue causing the overabundance of plasmasphere material in the inner magnetosphere is the aggressive refilling applied to the plasmasphere on closed field lines by the CIMI code. This realization represents the extent of my research completed before the writing of this dissertation.

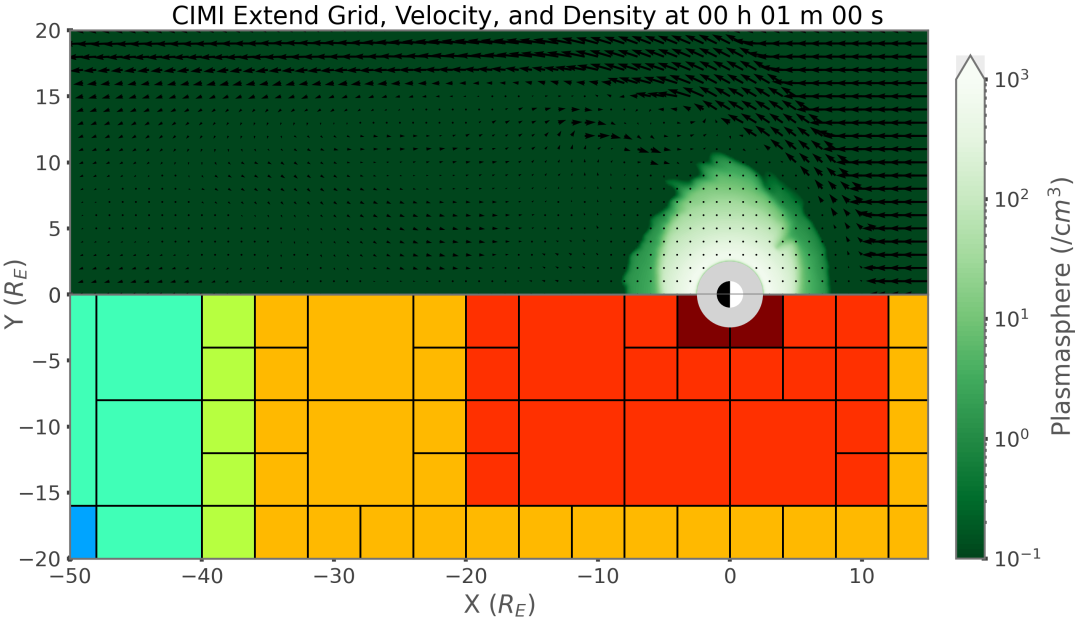

FIGURE 5.12: (Top) Z=0 slice of the state of the plasmasphere in BATS-R-US at 1 minute. Color map is of the density of the plasmasphere fluid. Black arrows show the velocity vector field of the plasmasphere. (Bottom) Grid of BATS-R-US with 24 million cells.

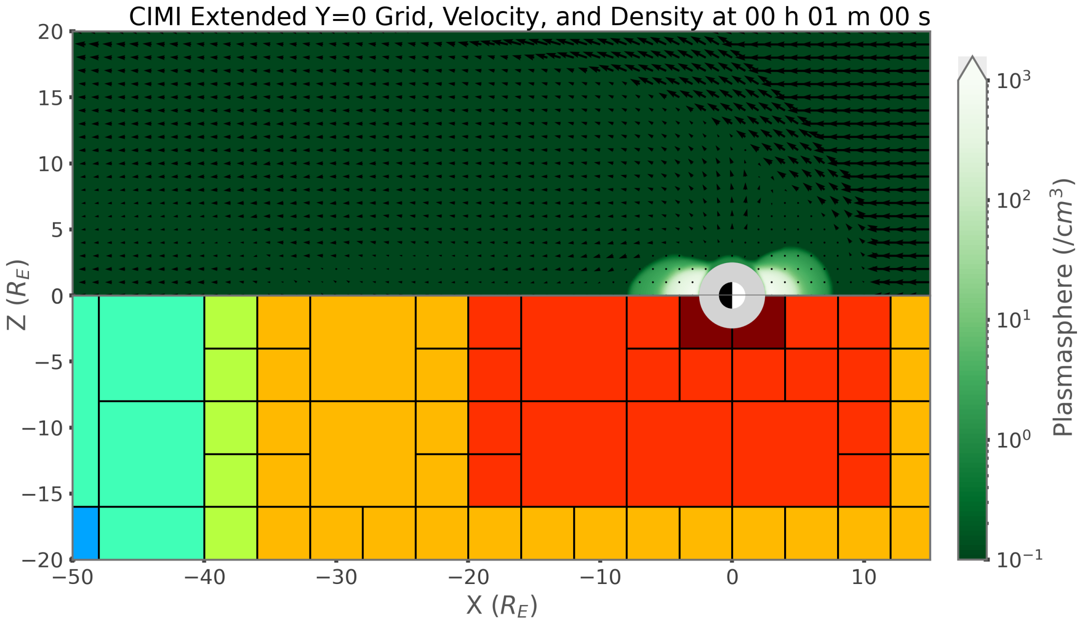

FIGURE 5.13: (Top) Y=0 slice of the state of the plasmasphere in BATS-R-US at 1 minute. Color map is of the density of the plasmasphere fluid. Black arrows show the velocity vector field of the plasmasphere. (Bottom) Grid of BATS-R-US with 24 million cells.

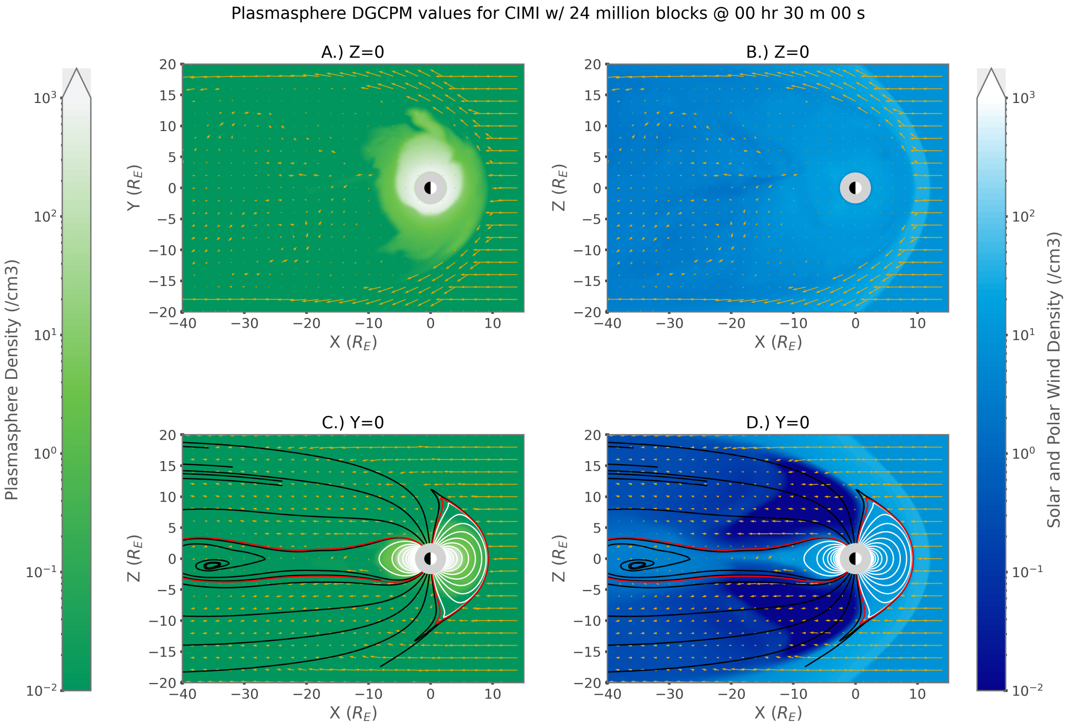

FIGURE 5.14: (A) Z=0 slice of BATS-R-US showing the density and velocity vector field of the of the plasmasphere. (B) Z=0 slice of BATS-R-US showing the density and velocity vector field of the of the combined solar wind and polar wind fluid. (C) Y=0 slice of BATS-R-US showing the density and velocity vector field of the of the plasmasphere. (D) Y=0 slice of BATS-R-US showing the density and velocity vector field of the of the combined solar wind and polar wind fluid.

Chapter 6

Conclusion and Closing Remarks

Through out this work I have presented my findings on the recirculation of the plasmasphere during magnetic storms. I conducted simulations with the SWMF configured to self-consistently model the plasmasphere within the inner magnetosphere via a novel configuration of the SWMF. I found in two simulations that the recirculating plasmasphere material can contribute anywhere from 8% to 70% of the total material crossing into the inner-magnetosphere during magnetic storms, with typical values being between 10% and 40%. I found that the initial condition of the plasmasphere had a significant impact on the amount and timing of plasmasphere recirculation seen on the night side measurement boundaries. I found that the path of recirculation changes through out the course of a storm, beginning as recirculation around the flanks and transitioning to recirculation over the poles latter in the storm. I demonstrated that in both simulations the plasmasphere is heated significantly from its initial 1 eV to several hundred or several thousand electron volts. I showed that even after the plasmasphere has been heated during recirculation it is still substantially colder (several keV) then the solar wind and polar wind fluid in the same simulation. This finding indicates a possible signature that can be found in real world data to confirm the presence of recirculated plasmasphere material in the plasma sheet. I published these findings in a peer reviewed journal and have presented them at several scientific conferences. Figures 4.6, 4.10, 4.4, and 4.12 demonstrate the major findings of the published work. These figures are the relative contribution for the recirculating plasmasphere fluid in the Ideal Square Wave Event and Idealized Corotating Interaction Region Event respectively, and the temperature difference of combined solar and polar wind fluid and the plasmasphere fluid in the Ideal Square Wave Event and Idealized Corotating Interaction Region Event respectively.

Following these simulations I worked to develop the CIMI model to treat the recirculating plasmasphere as a separate population within its framework. This new ability would enable the modeler run a single simulation and see the portion of the ring current energy provided by the recirculating plasmasphere. I verified the proper functioning of new code within CIMI, BATS-R-US, and the SWMF. I rigorously tested configurations of BATS-R-US and CIMI to produce results similar to the previously completed simulations. Reproduction of previous results would verify that the findings of Chapter 4 are not model dependent and also confirm that the changes made to BATS-R-US and CIMI behaved as intended. I demonstrated that when CIMI is a part of the SWMF grid resolution in BATS-R-US has a significant impact on the behaviour of the simulation. I created a new start up producer for CIMI which causes its initial condition for the plasmasphere to be a typical plasmasphere density profile, rather then the saturated plasmasphere produced by its default behaviour. Finally, I found that the primary issue driving the strong plasmasphere presence in CIMI is an aggressive refilling of the plasmasphere on closed field lines. The importance of the grid in BATS-R-US, the initial condition of CIMI, and the refilling behaviour of CIMI is demonstrated in Figures 5.5, 5.8, and 5.12 in the Z=0 plane, and Figure 5.6, 5.9, and 5.13 in the Y=0 plane.

Bibliography

1. Russell, C. T., Luhmann, J. G. & Strangeway, R. J. *Space physics: An introduction* (Cambridge University Press, 2016).
2. Klein, L. W. & Burlaga, L. F. Interplanetary magnetic clouds At 1 AU. *Journal of Geophysical Research: Space Physics* **87,** 613–624. eprint: `https://agupubs.onlinelibrary.wiley.com/doi/pdf/10.1029/JA087iA02p00613`. `https://agupubs.onlinelibrary.wiley.com/doi/abs/10.1029/JA087iA02p00613` (1982).
3. Gonzalez, W. *et al.* What is a geomagnetic storm? *Journal of Geophysical Research: Space Physics* **99,** 5771–5792 (1994).
4. Baumjohann, W. & Treumann, R. A. *Basic space plasma physics* (World Scientific, 2012).
5. Chappell, C. R., Huddleston, M. M., Moore, T. E., Giles, B. L. & Delcourt, D. C. Observations of the warm plasma cloak and an explanation of its formation in the magnetosphere. *Journal of Geophysical Research: Space Physics* **113,** n/a–

n/a. ISSN: 01480227. http://doi.wiley.com/10.1029/2007JA012945 (A9 Sept. 2008).

6. Wilder, F. D. *et al.* Magnetospheric Multiscale Observations of Waves and Parallel Electric Fields in Reconnecting Current Sheets in the Turbulent Magnetosheath. *Journal of Geophysical Research: Space Physics* **127.** e2022JA030511 2022JA030511, e2022JA030511. eprint: https://agupubs.onlinelibrary.wiley.com/doi/pdf/10.1029/2022JA030511. https://agupubs.onlinelibrary.wiley.com/doi/abs/10.1029/2022JA030511 (2022).

7. Kavanagh Jr., L. D., Freeman Jr., J. W. & Chen, A. J. Plasma flow in the magnetosphere. *Journal of Geophysical Research (1896-1977)* **73,** 5511–5519. eprint: https://agupubs.onlinelibrary.wiley.com/doi/pdf/10.1029/JA073i017p05511. https://agupubs.onlinelibrary.wiley.com/doi/abs/10.1029/JA073i017p05511 (1968).

8. Singh, N. & Horwitz, J. L. Plasmasphere refilling: Recent observations and modeling. *Journal of Geophysical Research: Space Physics* **97,** 1049–1079. ISSN: 2156-2202. https://agupubs.onlinelibrary.wiley.com/doi/full/10.1029/91JA02602%5C%4010.1002/%5C%28ISSN%5C%292169-9402.PLASREF1%20https://agupubs.onlinelibrary.wiley.com/doi/abs/10.1029/91JA02602%5C%4010.1002/%5C%28ISSN%5C%292169-9402.PLASREF1%

20https://agupubs.onlinelibrary.wiley.com/doi/10.1029/91JA02602@10.1002/(ISSN)2169-9402.PLASREF1 (A2 Feb. 1992).

9. Gallagher, D. L. & Comfort, R. H. Unsolved problems in plasmasphere refilling. *Journal of Geophysical Research: Space Physics* **121,** 1447–1451. eprint: https://agupubs.onlinelibrary.wiley.com/doi/pdf/10.1002/2015JA022279. https://agupubs.onlinelibrary.wiley.com/doi/abs/10.1002/2015JA022279 (2016).
10. Singh, N., Schunk, R. W. & Thiemann, H. Temporal features of the refilling of a plasmaspheric flux tube. *Journal of Geophysical Research: Space Physics* **91,** 13433–13454. eprint: https://agupubs.onlinelibrary.wiley.com/doi/pdf/10.1029/JA091iA12p13433. https://agupubs.onlinelibrary.wiley.com/doi/abs/10.1029/JA091iA12p13433 (1986).
11. Escoubet, C. P., Fehringer, M. & Goldstein, M. Introduction to the Cluster Mission. *Annales Geophysicae* **19,** 1197–1200 (10/12 2001).
12. Darrouzet, F., De Keyser, J., Décréau, P. M. E., El Lemdani-Mazouz, F. & Vallières, X. Statistical analysis of plasmaspheric plumes with Cluster/WHISPER observations. *Annales Geophysicae* **26,** 2403–2417. https://angeo.copernicus.org/articles/26/2403/2008/ (2008).

13. Décréau, P. M. E. *et al.* WHISPER, A RESONANCE SOUNDER AND WAVE ANALYSER: PERFORMANCES AND PERSPECTIVES FOR THE CLUSTER MISSION. *Space Science Reviews 1997 79:1* **79,** 157–193. ISSN: 1572-9672. `https://link.springer.com/article/10.1023/A:1004931326404` (1997).

14. McEntire, R. W. & Mitchell, D. G. in *Solar System Plasma Physics* 69–80 (American Geophysical Union (AGU), 1989). ISBN: 9781118664315. eprint: `https://agupubs.onlinelibrary.wiley.com/doi/pdf/10.1029/GM054p0069`. `https://agupubs.onlinelibrary.wiley.com/doi/abs/10.1029/GM054p0069`.

15. Burch, J. L. Image mission overview. *Space Science Reviews* **91,** 1–14. ISSN: 00386308 (2000).

16. Schmidt, A. Erdmagnetismus. *Enzyklopadie der Mathematischen Wissenschaft* **VI** (1917).

17. Chapman, S. I. The solar and lunar diurnal variations of terrestrial magnetism. *Philosophical Transactions of the Royal Society of London. Series A, Containing Papers of a Mathematical or Physical Character* **218,** 1–118 (1919).

18. Chapman, S. & Ferraro, V. C. A new theory of magnetic storms. *Nature* **126,** 129–130 (1930).

19. Chapman, S. & Ferraro, V. Terrestrial magnetism and atmospheric electricity. *J. Geophys. Res* **36,** 171–186 (1931).

20. Parker, E. Interaction of the solar wind with the geomagnetic field. *The Physics of Fluids* **1,** 171–187 (1958).

21. Dessler, A. J. & Parker, E. N. Hydromagnetic theory of geomagnetic storms. *Journal of Geophysical Research (1896-1977)* **64,** 2239–2252. eprint: `https://agupubs.onlinelibrary.wiley.com/doi/pdf/10.1029/JZ064i012p02239`. `https://agupubs.onlinelibrary.wiley.com/doi/abs/10.1029/JZ064i012p02239` (1959).

22. Sckopke, N. A general relation between the energy of trapped particles and the disturbance field near the Earth. *Journal of Geophysical Research (1896-1977)* **71,** 3125–3130. eprint: `https://agupubs.onlinelibrary.wiley.com/doi/pdf/10.1029/JZ071i013p03125`. `https://agupubs.onlinelibrary.wiley.com/doi/abs/10.1029/JZ071i013p03125` (1966).

23. Carovillano, R. L. & Siscoe, G. L. Energy and momentum theorems in magnetospheric processes. *Reviews of Geophysics* **11,** 289–353 (1973).

24. Freeman, J. W., Hills, H. K., Hill, T. W., Reiff, P. H. & Hardy, D. A. Heavy ion circulation in the Earth's magnetosphere. *Geophysical Research Letters* **4,** 195–197. eprint: `https://agupubs.onlinelibrary.wiley.com/doi/pdf/10.1029/GL004i005p00195`. `https://agupubs.onlinelibrary.wiley.com/doi/abs/10.1029/GL004i005p00195` (1977).

25. Borovsky, J. E., Thomsen, M. F. & McComas, D. J. The superdense plasma sheet: Plasmaspheric origin, solar wind origin, or ionospheric origin? *Journal of Geophysical Research: Space Physics* **102,** 22089–22097. eprint: `https://agupubs.onlinelibrary.wiley.com/doi/pdf/10.1029/96JA02469`. `https://agupubs.onlinelibrary.wiley.com/doi/abs/10.1029/96JA02469` (1997).
26. Daglis, L. A. *et al.* The Terrestrial Ring Current: Origin, Formation, and Decay. *Reviews of Geophysics* **37,** 407–438. ISSN: 87551209 (Nov. 1999).
27. Su, Y.-J. *et al.* Plasmaspheric material on high-latitude open field lines. *Journal of Geophysical Research: Space Physics* **106,** 6085–6095. eprint: `https://agupubs.onlinelibrary.wiley.com/doi/pdf/10.1029/2000JA003008`. `https://agupubs.onlinelibrary.wiley.com/doi/abs/10.1029/2000JA003008` (2001).
28. Elphic, R. C., Thomsen, M. F. & Borovsky, J. E. The fate of the outer plasmasphere. *Geophysical Research Letters* **24,** 365–368. eprint: `https://agupubs.onlinelibrary.wiley.com/doi/pdf/10.1029/97GL00141`. `https://agupubs.onlinelibrary.wiley.com/doi/abs/10.1029/97GL00141` (1997).
29. Weimer, D. R. A flexible, IMF dependent model of high-latitude electric potentials having "Space Weather" applications. *Geophysical Research Letters* **23,** 2549–2552. eprint: `https://agupubs.onlinelibrary.wiley.com/doi/pdf/`

10.1029/96GL02255. https://agupubs.onlinelibrary.wiley.com/doi/abs/10.1029/96GL02255 (1996).

30. Tsyganenko, N. A magnetospheric magnetic field model with a warped tail current sheet. *Planetary and Space Science* **37,** 5–20. ISSN: 0032-0633. https://www.sciencedirect.com/science/article/pii/0032063389900664 (1989).
31. Moore, T. E., Fok, M.-C., Delcourt, D. C., Slinker, S. P. & Fedder, J. A. Plasma plume circulation and impact in an MHD substorm. *Journal of Geophysical Research: Space Physics* **113.** eprint: https://agupubs.onlinelibrary.wiley.com/doi/pdf/10.1029/2008JA013050. https://agupubs.onlinelibrary.wiley.com/doi/abs/10.1029/2008JA013050 (2008).
32. The Lyon–Fedder–Mobarry (LFM) global MHD magnetospheric simulation code.
33. Tóth, G. *et al.* Space weather modeling framework: A new tool for the space science community. *Journal of Geophysical Research: Space Physics* **110.** ISSN: 21699402 (2005).
34. Gombosi, T. I. *et al.* What sustained multi-disciplinary research can achieve: The space weather modeling framework. *Journal of Space Weather and Space Climate* **11,** 42. ISSN: 2115-7251. https://www.swsc-journal.org/articles/

swsc/full_html/2021/01/swsc210015/swsc210015.html%20https://www.swsc-journal.org/articles/swsc/abs/2021/01/swsc210015/swsc210015.html (2021).

35. Yu, Y. & Ridley, A. J. Validation of the space weather modeling framework using ground-based magnetometers. *Space Weather* **6.** eprint: https://agupubs.onlinelibrary.wiley.com/doi/pdf/10.1029/2007SW000345. https://agupubs.onlinelibrary.wiley.com/doi/abs/10.1029/2007SW000345 (2008).

36. Wang, H., Ridley, A. J. & Lühr, H. Validation of the Space Weather Modeling Framework using observations from CHAMP and DMSP. *Space Weather* **6.** ISSN: 1542-7390. https://onlinelibrary.wiley.com/doi/full/10.1029/2007SW000355%20https://onlinelibrary.wiley.com/doi/abs/10.1029/2007SW000355%20https://agupubs.onlinelibrary.wiley.com/doi/10.1029/2007SW000355 (Mar. 2008).

37. Pulkkinen, A. *et al.* Community-wide validation of geospace model ground magnetic field perturbation predictions to support model transition to operations. *Space Weather* **11,** 369–385. ISSN: 15427390 (6 June 2013).

38. Glocer, A. *et al.* Community-wide validation of geospace model local K-index predictions to support model transition to operations. *Space Weather* **14,** 469–480. eprint: https://agupubs.onlinelibrary.wiley.com/doi/pdf/10.

1002/2016SW001387. https://agupubs.onlinelibrary.wiley.com/doi/abs/10.1002/2016SW001387 (2016).

39. Sachdeva, N. *et al.* Validation of the Alfvén wave solar atmosphere model (AWSoM) with observations from the low corona to 1 Au. *The Astrophysical Journal* **887,** 83 (2019).

40. Stout, Q. F. *et al. Adaptive Blocks: A High Performance Data Structure* in *Proceedings of the 1997 ACM/IEEE Conference on Supercomputing* (Association for Computing Machinery, San Jose, CA, 1997), 1–10. ISBN: 0897919858. https://doi.org/10.1145/509593.509650.

41. Grotht, C. P., De Zeeuw, D. L., Powell, K. G., Gombosi, T. I. & Stout, Q. F. A parallel solution-adaptive scheme for ideal magnetohydrodynamics. *14th Computational Fluid Dynamics Conference* **309,** 1–16 (1999).

42. Roe, P. L. & Balsara, D. S. Notes on the Eigensystem of Magnetohydrodynamics. *SIAM Journal on Applied Mathematics* **56,** 57–67. eprint: https://doi.org/10.1137/S003613999427084X. https://doi.org/10.1137/S003613999427084X (1996).

43. Tóth, G. The ·B=0 Constraint in Shock-Capturing Magnetohydrodynamics Codes. *Journal of Computational Physics* **161,** 605–652. ISSN: 0021-9991. https:

//www.sciencedirect.com/science/article/pii/S0021999100965197 (2000).

44. De Zeeuw, D., Gombosi, T., Groth, C., Powell, K. & Stout, Q. An adaptive MHD method for global space weather simulations. *IEEE Transactions on Plasma Science* **28,** 1956–1965 (2000).

45. Ridley, A. J. *et al.* University of Michigan MHD results of the Geospace Global Circulation Model metrics challenge. *Journal of Geophysical Research: Space Physics* **107,** SMP 12-1-SMP 12–19. eprint: https://agupubs.onlinelibrary.wiley.com/doi/pdf/10.1029/2001JA000253. https://agupubs.onlinelibrary.wiley.com/doi/abs/10.1029/2001JA000253 (2002).

46. Ridley, A. J., Richmond, A. D., Gombosi, T. I., De Zeeuw, D. L. & Clauer, C. R. Ionospheric control of the magnetospheric configuration: Thermospheric neutral winds. *Journal of Geophysical Research: Space Physics* **108.** eprint: https://agupubs.onlinelibrary.wiley.com/doi/pdf/10.1029/2002JA009464. https://agupubs.onlinelibrary.wiley.com/doi/abs/10.1029/2002JA009464 (2003).

47. Ridley, A. J., Gombosi, T. I. & Dezeeuw, D. L. Ionospheric control of the magnetosphere: conductance. **22,** 567–584 (2004).

48. Moen, J. & Brekke, A. The solar flux influence on quiet time conductances in the auroral ionosphere. *Geophysical Research Letters* **20,** 971–974. eprint: `https://agupubs.onlinelibrary.wiley.com/doi/pdf/10.1029/92GL02109`. `https://agupubs.onlinelibrary.wiley.com/doi/abs/10.1029/92GL02109` (1993).

49. Rich, F. J. & Hairston, M. Large-scale convection patterns observed by DMSP. *Journal of Geophysical Research: Space Physics* **99,** 3827–3844. eprint: `https://agupubs.onlinelibrary.wiley.com/doi/pdf/10.1029/93JA03296`. `https://agupubs.onlinelibrary.wiley.com/doi/abs/10.1029/93JA03296` (1994).

50. Mukhopadhyay, A. *et al.* Conductance Model for Extreme Events: Impact of Auroral Conductance on Space Weather Forecasts. *Space Weather* **18.** e2020SW002551 10.1029/2020SW002551, e2020SW002551. eprint: `https://agupubs.onlinelibrary.wiley.com/doi/pdf/10.1029/2020SW002551`. `https://agupubs.onlinelibrary.wiley.com/doi/abs/10.1029/2020SW002551` (2020).

51. Amm. Comment on "A three-dimensional, iterative mapping procedure for the implementation of an ionosphere-magnetosphere anisotropic Ohm's law boundary condition in global magnetohydrodynamic simulations". *Annales Geophysicae* **14,** 773–775. `http://pascal-francis.inist.fr/vibad/index.php?action=getRecordDetail&idt=3141790` (1996).

52. Ridley, A. J., Crowley, G. & Freitas, C. An empirical model of the ionospheric electric potential. *Geophysical Research Letters* **27,** 3675–3678. eprint: `https://agupubs.onlinelibrary.wiley.com/doi/pdf/10.1029/1999GL011161`. `https://agupubs.onlinelibrary.wiley.com/doi/abs/10.1029/1999GL011161` (2000).

53. Fok, M.-C., Wolf, R. A., Spiro, R. W. & Moore, T. E. Comprehensive computational model of Earth's ring current. *Journal of Geophysical Research: Space Physics* **106,** 8417–8424. eprint: `https://agupubs.onlinelibrary.wiley.com/doi/pdf/10.1029/2000JA000235`. `https://agupubs.onlinelibrary.wiley.com/doi/abs/10.1029/2000JA000235` (2001).

54. Fok, M.-C., Ebihara, Y., Moore, T. E., Ober, D. M. & Keller, K. A. in *Inner Magnetosphere Interactions: New Perspectives from Imaging* 207–220 (American Geophysical Union (AGU), 2005). ISBN: 9781118666128. eprint: `https://agupubs.onlinelibrary.wiley.com/doi/pdf/10.1029/159GM16`. `https://agupubs.onlinelibrary.wiley.com/doi/abs/10.1029/159GM16`.

55. Buzulukova, N., Fok, M.-C., Moore, T. E. & Ober, D. M. Generation of plasmaspheric undulations. *Geophysical Research Letters* **35.** eprint: `https://agupubs.onlinelibrary.wiley.com/doi/pdf/10.1029/2008GL034164`. `https://agupubs.onlinelibrary.wiley.com/doi/abs/10.1029/2008GL034164` (2008).

56. Fok, M.-C., Moore, T. E. & Spjeldvik, W. N. Rapid enhancement of radiation belt electron fluxes due to substorm dipolarization of the geomagnetic field. *Journal of Geophysical Research: Space Physics* **106,** 3873–3881. eprint: https://agupubs.onlinelibrary.wiley.com/doi/pdf/10.1029/2000JA000150. https://agupubs.onlinelibrary.wiley.com/doi/abs/10.1029/2000JA000150 (2001).

57. Zheng, Y., Fok, M.-C. & Khazanov, G. V. A radiation belt-ring current forecasting model. *Space Weather* **1.** eprint: https://agupubs.onlinelibrary.wiley.com/doi/pdf/10.1029/2003SW000007. https://agupubs.onlinelibrary.wiley.com/doi/abs/10.1029/2003SW000007 (2003).

58. Buzulukova, N. *et al.* Ring current dynamics in moderate and strong storms: Comparative analysis of TWINS and IMAGE/HENA data with the Comprehensive Ring Current Model. *Journal of Geophysical Research: Space Physics* **115.** eprint: https://agupubs.onlinelibrary.wiley.com/doi/pdf/10.1029/2010JA015292. https://agupubs.onlinelibrary.wiley.com/doi/abs/10.1029/2010JA015292 (2010).

59. Fok, M.-C. & Moore, T. E. Ring current modeling in a realistic magnetic field configuration. *Geophysical Research Letters* **24,** 1775–1778. eprint: https://agupubs.onlinelibrary.wiley.com/doi/pdf/10.1029/97GL01255. https:

//agupubs.onlinelibrary.wiley.com/doi/abs/10.1029/97GL01255 (1997).

60. Fok, M.-C. *et al.* The Comprehensive Inner Magnetosphere-Ionosphere Model. *Journal of Geophysical Research: Space Physics* **119,** 7522–7540. eprint: https://agupubs.onlinelibrary.wiley.com/doi/pdf/10.1002/2014JA020239. https://agupubs.onlinelibrary.wiley.com/doi/abs/10.1002/2014JA020239 (2014).
61. Sheldon, R. B. & Hamilton, D. C. Ion transport and loss in the Earth's quiet ring current: 1. Data and standard model. *Journal of Geophysical Research: Space Physics* **98,** 13491–13508. eprint: https://agupubs.onlinelibrary.wiley.com/doi/pdf/10.1029/92JA02869. https://agupubs.onlinelibrary.wiley.com/doi/abs/10.1029/92JA02869 (1993).
62. Vette, J. I. in *The AE-8 Trapped Electron Model Environment* (National Space Science Data Center, NASA Goddard Space Flight Center, 1991).
63. Fung, S. F. in *Radiation Belts: Models and Standards* 79–91 (American Geophysical Union (AGU), 1996). ISBN: 9781118664261. eprint: https://agupubs.onlinelibrary.wiley.com/doi/pdf/10.1029/GM097p0079. https://agupubs.onlinelibrary.wiley.com/doi/abs/10.1029/GM097p0079.

64. Ober, D. M. & Daniel M. Ober, J.L. Horwitz, D. G. Formation of density troughs embedded in the outer plasmasphere by subaruroral ion drift events. *JOURNAL OF GEOPHYSICAL RESEARCH* **102,** 14595–14602. ISSN: 01480227 (1997).

65. Carpenter, D. L. & Anderson, R. R. An ISEE/whistler model of equatorial electron density in the magnetosphere. *Journal of Geophysical Research: Space Physics* **97,** 1097–1108. eprint: `https://agupubs.onlinelibrary.wiley.com/doi/pdf/10.1029/91JA01548`. `https://agupubs.onlinelibrary.wiley.com/doi/abs/10.1029/91JA01548` (1992).

66. Ridley, A. J., Dodger, A. M. & Liemohn, M. W. Exploring the efficacy of different electric field models in driving a model of the plasmasphere. *Journal of Geophysical Research: Space Physics* **119,** 4621–4638. eprint: `https://agupubs.onlinelibrary.wiley.com/doi/pdf/10.1002/2014JA019836`. `https://agupubs.onlinelibrary.wiley.com/doi/abs/10.1002/2014JA019836` (2014).

67. Tóth, G. *et al.* Adaptive numerical algorithms in space weather modeling. *Journal of Computational Physics* **231.** Special Issue: Computational Plasma Physics, 870–903. ISSN: 0021-9991. `https://www.sciencedirect.com/science/article/pii/S002199911100088X` (2012).

68. Glocer, A. *et al.* A Case Study on the Origin of Near-Earth Plasma. *Journal of Geophysical Research: Space Physics* **125.** ISSN: 21699402 (11 Nov. 2020).

69. Welling, D. T. & Ridley, A. J. Validation of SWMF magnetic field and plasma. *Space Weather* **8.** eprint: `https://agupubs.onlinelibrary.wiley.com/doi/pdf/10.1029/2009SW000494`. `https://agupubs.onlinelibrary.wiley.com/doi/abs/10.1029/2009SW000494` (2010).

70. Welling, D. T. & Liemohn, M. W. The ionospheric source of magnetospheric plasma is not a black box input for global models. *Journal of Geophysical Research: Space Physics* **121,** 5559–5565. eprint: `https://agupubs.onlinelibrary.wiley.com/doi/pdf/10.1002/2016JA022646`. `https://agupubs.onlinelibrary.wiley.com/doi/abs/10.1002/2016JA022646` (2016).

71. Ridley, A. J., Gombosi, T. I. & DeZeeuw, D. L. Ionospheric control of the magnetosphere: conductance. *Annales Geophysicae* **22,** 567–584. `https://angeo.copernicus.org/articles/22/567/2004/` (2004).

72. Welling, D. in *Geomagnetically Induced Currents from the Sun to the Power Grid* 43–65 (American Geophysical Union (AGU), 2019). ISBN: 9781119434412. eprint: `https://agupubs.onlinelibrary.wiley.com/doi/pdf/10.1002/9781119434412.ch3`. `https://agupubs.onlinelibrary.wiley.com/doi/abs/10.1002/9781119434412.ch3`.

73. Ridley, A. J., Dodger, A. M. & Liemohn, M. W. Exploring the efficacy of different electric field models in driving a model of the plasmasphere. *Journal of Geophysical Research: Space Physics* **119,** 4621–4638. ISSN: 21699402 (2014).

74. Welling, D. T. & Liemohn, M. W. Outflow in global magnetohydrodynamics as a function of a passive inner boundary source. *Journal of Geophysical Research: Space Physics* **119,** 2691–2705. ISSN: 21699402 (2014).

75. Singh, A. K., Singh, R. P. & Siingh, D. State studies of Earths plasmasphere: A review. *Planetary and Space Science* **59,** 810–834. ISSN: 00320633. http://dx.doi.org/10.1016/j.pss.2011.03.013 (2011).

76. Darrouzet, F. & De Keyser, J. The dynamics of the plasmasphere: Recent results. *Journal of Atmospheric and Solar-Terrestrial Physics* **99,** 53–60. ISSN: 13646826. http://dx.doi.org/10.1016/j.jastp.2012.07.004 (July 2012).

77. Frahm, R. A. *et al.* The diffuse aurora: A significant source of ionization in the middle atmosphere. *Journal of Geophysical Research: Atmospheres* **102,** 28203–28214. eprint: https://agupubs.onlinelibrary.wiley.com/doi/pdf/10.1029/97JD02430. https://agupubs.onlinelibrary.wiley.com/doi/abs/10.1029/97JD02430 (1997).

78. Newell, P. T., Sotirelis, T., Liou, K., Meng, C.-I. & Rich, F. J. A nearly universal solar wind-magnetosphere coupling function inferred from 10 magnetospheric state variables. *Journal of Geophysical Research: Space Physics* **112.** eprint: `https://agupubs.onlinelibrary.wiley.com/doi/pdf/10.1029/2006JA012015`. `https://agupubs.onlinelibrary.wiley.com/doi/abs/10.1029/2006JA012015` (2007).

79. Newell, P. T., Sotirelis, T. & Wing, S. Diffuse, monoenergetic, and broadband aurora: The global precipitation budget. *Journal of Geophysical Research: Space Physics* **114.** eprint: `https://agupubs.onlinelibrary.wiley.com/doi/pdf/10.1029/2009JA014326`. `https://agupubs.onlinelibrary.wiley.com/doi/abs/10.1029/2009JA014326` (2009).

80. Richmond, A. D. & Kamide, Y. Mapping electrodynamic features of the high-latitude ionosphere from localized observations: Technique. *Journal of Geophysical Research: Space Physics* **93,** 5741–5759. eprint: `https://agupubs.onlinelibrary.wiley.com/doi/pdf/10.1029/JA093iA06p05741`. `https://agupubs.onlinelibrary.wiley.com/doi/abs/10.1029/JA093iA06p05741` (1988).

81. Welling, D. T. & Ridley, A. J. Exploring sources of magnetospheric plasma using multispecies MHD. *Journal of Geophysical Research: Space Physics* **115.** eprint: `https://agupubs.onlinelibrary.wiley.com/doi/pdf/10.1029/`

2009JA014596. https://agupubs.onlinelibrary.wiley.com/doi/abs/10.1029/2009JA014596 (2010).

82. Toledo-Redondo, S. *et al.* Cold ion heating at the dayside magnetopause during magnetic reconnection. *Geophysical Research Letters* **43,** 58–66. eprint: https://agupubs.onlinelibrary.wiley.com/doi/pdf/10.1002/2015GL067187. https://agupubs.onlinelibrary.wiley.com/doi/abs/10.1002/2015GL067187 (2016).

83. Welling, D. T., Jordanova, V. K., Zaharia, S. G., Glocer, A. & Toth, G. The effects of dynamic ionospheric outflow on the ring current. *Journal of Geophysical Research: Space Physics* **116,** 1–15. ISSN: 21699402 (2011).

84. Katus, R. M. *et al.* Statistical analysis of the geomagnetic response to different solar wind drivers and the dependence on storm intensity. *Journal of Geophysical Research: Space Physics* **120,** 310–327. ISSN: 21699380. http://doi.wiley.com/10.1002/2014JA020712%20https://onlinelibrary.wiley.com/doi/full/10.1002/2014JA020712%20https://onlinelibrary.wiley.com/doi/abs/10.1002/2014JA020712%20https://agupubs.onlinelibrary.wiley.com/doi/10.1002/2014JA020712 (1 Jan. 2015).